University of Illinois at Urbana-Champaign

ACRC

Air Conditioning and Refrigeration Center A National Science Foundation/University Cooperative Research Center

Including Material Cost and Strength Constraints in Heat Exchanger Design

I. E. Davidson and C. W. Bullard

ACRC TR-250 October 2006

For additional information:

Air Conditioning and Refrigeration Center
University of Illinois
Department of Mechanical Science & Engineering
1206 West Green Street
Urbana, IL 61801

(217) 333-3115

Prepared as part of ACRC Project #186
Including Material Cost and Strength Constraints in Heat Exchanger Design
C. W. Bullard, Principal Investigators

The Air Conditioning and Refrigeration Center was founded in 1988 with a grant from the estate of Richard W. Kritzer, the founder of Peerless of America Inc. A State of Illinois Technology Challenge Grant helped build the laboratory facilities. The ACRC receives continuing support from the Richard W. Kritzer Endowment and the National Science Foundation. The following organizations have also become sponsors of the Center.

Arçelik A. S.
Behr GmbH and Co.
Carrier Corporation
Cerro Flow Products, Inc.
Daikin Industries, Ltd.
Danfoss A/S
Delphi Thermal and Interior
Embraco S. A.
Emerson Climate Technologies, Inc.
General Motors Corporation
Hill PHOENIX
Honeywell, Inc.
Hydro Aluminum Precision Tubing
Ingersoll-Rand/Climate Control
Lennox International, Inc.
LG Electronics, Inc.
Manitowoc Ice, Inc.
Matsushita Electric Industrial Co., Ltd.
Modine Manufacturing Co.
Novelis Global Technology Centre
Parker Hannifin Corporation
Peerless of America, Inc.
Samsung Electronics Co., Ltd.
Sanden Corporation
Sanyo Electric Co., Ltd.
Tecumseh Products Company
Trane
Visteon Automotive Systems
Wieland-Werke, AG

For additional information:

Air Conditioning & Refrigeration Center
Mechanical & Industrial Engineering Dept.
University of Illinois
1206 West Green Street
Urbana, IL 61801

217 333 3115

ABSTRACT

This project extends analysis of heat exchanger design tradeoffs in response to two emerging trends: 1) demands for increasing thermal performance while reducing material costs are beginning to raise structural issues; and 2) new manufacturing technologies are enabling designs that lie outside the envelope of existing empirical databases and performance correlations. Optimization methods are used to explore both conventional and unconventional designs in this broader parameter space, dealing explicitly with material- and manufacturing-related constraints. New semi-empirical correlations for heat transfer and friction factor are developed and used for analyzing flat- and round-tube plain fin heat exchangers. The role of structural constraints is illustrated by focusing on condenser optimization using a residential air conditioning model, but the analysis yields insights that applicable to other components and applications. Ways of avoiding some of these constraints are discussed in some detail

Table of Contents

List of Figures

Page

List of Tables

Page

List of Symbols

All symbols use units listed unless otherwise specified

Symbols

A	area [m^2]
A_{face}	Core face area [m^2]
D	tube outer diameter [mm]
D_c	Collar Diameter = $D + 2F_t$ [mm]
D_h	Hydraulic diameter = $4A_{channel}/P$ [mm]
EF	enhancement factor [-]
f	Darcy friction factor [-]
F	Fin parameter [mm]
Gz	Graetz Number = $1/x^*$ [-]
h	Heat transfer coefficient [W/m^2K]
k	Thermal conductivity [W/mK]
L	Louver parameter [mm or °] or total condenser depth
m	condenser mass [kg]
N	number of rows [-]
N_{slits}	Number of slits between tubes [-]
Nu	Nusselt number = hD_h/k [-]
Nu_D	Nusselt number based on tube outer diameter = hD/k [-]
P	Wetted perimeter [m]
Pr	Prandlt number [-]
Q	System capacity [kW]
Re_D	Reynolds number = VD/ν [-]
Re_{Dh}	Reynolds number = VD_h/ν
S_l	Condenser longitudinal tube pitch [mm]
S_t	Condenser transverse tube pitch [mm]
T	Temperature [C]
T_{evap}	Evaporating temperature [C]
$T_{outdoor}$	Outdoor temperature [C]
V	Condenser air velocity [m/s]
$\dot{W}$	Power [kW]
W_{evap}	Evaporator fan power [kW]
x	Channel depth, core depth [m]
x^*	Heat transfer depth [-]
X/D	distance from rear tube surface to tube outer diameter ratio [-]
$x+$	Friction factor depth [-]
α	Aspect ratio [-]
ΔP	Pressure drop [Pa]
η_{comp}	Compressor efficiency isentropic [-]
η_{fan}	Condenser fan and motor isentropic efficiency [-]
η_{fin}	fin efficiency [-]
ν	Kinematic viscosity

Subscripts

2D	Zero aspect ratio
3D	3 dimension, any aspect ratio
a	Airside
air	Air
app	Approach
c	Collar
channel	channel (between fins)
comp	Compressor
cond	Condenser
Dh	Based on channel hydraulic diameter
enh	Enhanced
face	From front of condenser
FD	Fully developed
fins/fin	Fins or fin
h	Hydraulic
h	Height
i	Section number
Ichi	From Ichimiya et al. (1988)
in	Condenser inlet
loc	Local
max	Minimum freeflow area
p	Pitch
plate	Flat plate
r	Refrigerant side
rect	Rectangular cross section channel
s	Spacing
sat	Saturation
surface	Surface
system/sys	System
t	Thickness
tubes	Tubes
x	Based on depth
Z	Form Zukauskas (1972)

Chapter 1. Introduction

Recent changes in the relative prices of copper and aluminum, combined with the emergence of new manufacturing techniques involving both brazing and mechanical fin/tube contact, has stimulated interest in revisiting some of the fundamental tradeoffs associated with heat exchanger design. At the same time increased pressures for increasing equipment efficiency are leading product engineers to increase the thermal-hydraulic performance of heat exchangers. Both of these trends are expanding the traditional design space into areas where the tradeoffs among heat transfer, pressure drop, structural strength and material and manufacturing costs differ in fundamental ways from the experience of the past.

Efforts to decrease refrigerant-side heat transfer resistance and air-side pressure drop have already prompted a shift to 7 mm tubes and to brazed aluminum heat exchangers. In both cases the new designs are increasing the cost distributing refrigerant uniformly, or in some cases matching the nonuniformity of the air flow distribution. With round tubes there is the cost of joining many more circuits to the heat exchanger core, and with flat tubes the high cost of brazing many tubes to headers has led to brazing the entire heat exchanger instead of relying on mechanical means for fin/tube contact. Thermal-hydraulic considerations alone lead to preference for minimizing diameters, maximizing the number of parallel circuits and making flat tubes wider than current technology permits.

Finally, increasing demand for reversible heat pumps has stimulated research on ways of circuiting heat exchangers in such a manner as minimize the risks associated with repeatedly splitting or re-distributing 2-phase flows. While the hydrodynamic implications are not severe in condensers where the goal is to equally distribute the vapor (relatively easy because of high void fraction), it is a very serious issue in evaporators where it is necessary to distribute the droplets which account for a very small volume-fraction of the flow. In heat pumps, both heat exchangers must function as an evaporator for part of the time. Kulkarni and Bullard (2003) quantified these effects in an earlier ACRC project, and investigated ways of minimizing the losses by focusing on single-circuit designs having no intermediate headers or Y-junctions. Ongoing work by Elbel and Hrnjak (2006) is exploring flash gas bypass and ejectors as a way of avoiding altogether the need to distribute 2-phase flow.

Chapters 2 and 3 of this report present the results of optimization analyses that search for optimal heat exchanger configurations, subject to a few constraints on package size (face area), refrigerant circuiting (reversible for heat pumping) and fin and tube diameters and wall thicknesses. One set of analyses was conducted for round- and flat-tube heat exchangers having louvered or offset strip fins. The results show show clearly that the optimal designs lie outside the historic parameter space that has been characterized by empirically-derived heat transfer and pressure drop correlations. Since the optimal configurations are constrained mainly by a lack of test data instead of material or manufacturing limits, it is not possible to identify the optimal designs, or to examine related structural constraints and material cost tradeoffs without extensive testing of new heat exchanger configurations.

However it was possible to identify optimal heat exchanger configurations lying outside the historic parameter space for the case of plain fins, by constructing new heat transfer and pressure drop correlations using physical insights obtained from small scale laboratory experiments for use in optimizing air conditioner condenser designs.

Chapters 2 and 3 cover flat and round tube heat exchangers, respectively. New semi-empirical correlations for plain fin heat exchangers are developed. The resulting optimal heat exchanger configurations are compared to

those identified using the highly-constrained purely empirical correlations available for enhanced fins. The analyses focus on the condenser in a residential air conditioning system. The tradeoff between minimum system power consumption and condenser mass is discussed, followed by a discussion of system power sensitivity to some design constraints. Finally, economic tradeoffs are discussed. The conclusions are summarized at the end of the chapter.

For both types of heat exchangers, an effort was made to avoid over-constraining the search for optimal designs. For example some strength-related factors (e.g. burst pressure, core rigidity) may severely limit the optimization of brazed aluminum heat exchangers, but would pose no problem for heat exchangers that rely on other methods of fin/tube contact, such as mechanical expansion or thermal adhesives. Therefore Chapter 4 explores the nature of these kinds of constraints and their relation to various manufacturing methods. It concludes by pointing to new possibilities for configuring heat exchangers to best exploit the unique properties of copper and aluminum, by developing methods of fabrication that circumvent the constraints that currently impose limits on evaporator and condenser designs.

Three appendices follow the two main chapters. The first, Appendix A, explains the correlations used in the condenser optimizations in detail. Correlation accuracy and limitations are discussed, as well and the optimal configurations found. Appendix B describes the sensitivity analyses and provides detail on the multi-layer optimizations. More condenser economics are also discussed. Appendix C describes important physical phenomena at work in round tube plain fin heat exchangers. Single-row and multi-row, and small and large fin pitch situations are discussed.

The flat tube plain fin correlations make use of combined entry region airflow in 3D rectangular channel as functions of channel depth, Reynolds number, hydraulic diameter, and channel aspect ratio. The correlations were designed to approach known physical limits as the channel aspect ratio and channel depth approach zero, and as the flow becomes fully developed. The curve fits were constructed by bridging continuously between these well known analytical and numerical results for 2D and 3D channels. The RMS value of the curve fits were 1.5 and 2.7% for heat transfer coefficient and friction factor, respectively. The optimal configuration was compared with that obtained using empirical louvered fin flat tube correlations. For any condenser mass, the plain fins show better performance throughout the parameter space covered by the empirical correlations. The physically-based correlations describe efficient design options beyond those limits.

The round tube plain fin correlations were designed to be accurate for heat exchangers that have relatively large fin pitch. The approach taken for the semi-empirical correlations superimposes a fin array and tube bank, and then adds empirically-based terms to account explicitly for the streamwise and spanwise vortices. Comparisons with available data show good agreement (within 10% for most configurations) for heat exchangers having large fin pitch (over 4 mm), where these effects are dominant. At small fin pitch (under 3 mm) the model neglects the formation of the stagnant wake, thereby grossly over estimating heat transfer. When this model and the empirical models were then applied to the optimization of the air conditioning condenser, the empirical correlations limit the optimization on several search variables and the semi-analytical correlation limited by its lower bound on fin pitch.

Chapter 2. Microchannel Heat Exchangers

2.1 Microchannel Heat Exchanger Introduction

This paper develops air-side heat transfer and Darcy friction factor correlations that bridge – with a continuous function – the full range of rectangular channel hydraulic diameters, aspect ratios, flow lengths and laminar Reynolds numbers. It is suitable for use with optimization algorithms that cannot tolerate discontinuities.

Microchannel heat exchangers are used widely for automotive a/c condensers and other applications where compactness is important. Their flat multiport tubes contribute to low air-side pressure drop and substantially increase refrigerant-side area, compared to the round tubes used in other applications. Recently, demands for increased efficiency in stationary a/c applications have led to increased outdoor air flow requirements to provide a larger heat sink. For this and other reasons, flat tube heat exchangers are now being considered for a wider range of applications where weight and flow depth are not as highly constrained as in mobile applications, and where air-side pressure drop is a more important consideration.

Unfortunately the empirical correlations developed for heat transfer and pressure drop on the air side of microchannel heat exchangers (Chang and Wang, 1997) are limited to the louvered fins, small fin pitch, short flow lengths and high face velocities typical of automotive applications. Such heat transfer and pressure drop correlations are generally accurate within ± 15%. On the other hand, flat-tube heat exchangers optimized for stationary heat pump applications may need plain fins to minimize condensate bridging and frost fouling, and to facilitate drainage of condensate and melt water. Since existing correlations are empirical, they cannot be extrapolated.

In order to be truly robust, a correlation must provide accurate predictions for any configuration. This was attempted by Muzychka and Yovanovich (2004). They developed a correlation for heat transfer in non-circular ducts of various shapes and sizes. The accuracy reported for this correlation is: "±15% for most non-circular ducts and channels." Stephan (1959) addressed heat transfer in developing flow of a 2D duct, while Shah and London (1978) developed a correlation for friction factor. These correlations were based on numerical and analytical solutions and apply to any depth. To include the effect of channel aspect ratio, modifications by Shah and London (1978) produced empirical correlations for Nusselt number and friction factor in fully developed rectangular channels. The combined correlations were reported to be accurate within ±0.05% and 0.1% respectively. This chapter presents and uses numerical results by Wibulswas (1966) and Curr et al. (1972).

2.2 3-D Channel Flow Correlation Development

2.2.1 Methodology

Existing correlations for rectangular channels are expressed in terms of two nondimensional geometric parameters, aspect ratio and flow depth. Two dimensional channel heat transfer and friction factor correlations are expressed as a function of non-dimensional flow length or heat exchanger depth (x^* for heat transfer and x^+ for friction factor, differing only due to the dependence of heat transfer on the Prandlt number) for simultaneously developing flow. For rectangular channels the aspect ratio $0 \leq \alpha \leq 1$ is the ratio of channel width to height.

The 3D correlations introduced here were constrained to approach three physically known limits: leading edge flow, fully developed flow, and a developing 2D duct (aspect ratio of zero) flow. Table 2.1 shows the scope of the 3D channel airflow heat transfer correlation with Nusselt numbers tabulated by Wibulswas (1966) and Stephan (1959) for varying aspect ratio and x^* with the three imposed physical limits. The same physical limits apply for friction factor.

Table 2.1 Wibulswas' (1966) numerical results, limiting cases and gaps

	α							
1/x*	1	0.5	1/3	0.25	1/6	small	0 (Stephan)	$h_{Stephan}/h_{plate}$
	Fully developed							
10	3.75	4.2	4.67	5.11	5.72		7.839	3.54
20	4.39	4.79	5.17	5.56	6.13		8.143	2.6
30	4.88	5.23	5.6	5.93	6.47		8.443	2.2
40	5.27	5.61	5.96	6.27	6.78		8.734	1.972
50	5.63	5.95	6.28	6.61	7.07		9.017	1.821
60	5.95	6.27	6.6	6.9	7.35		9.292	1.713
80	6.57	6.88	7.17	7.47	7.9		9.823	1.568
100	7.1	7.42	7.7	7.98	8.38		10.33	1.475
120	7.61	7.91	8.18	8.48	8.85		10.81	1.409
140	8.06	8.37	8.66	8.93	9.28		11.28	1.361
160	8.5	8.8	9.1	9.36	9.72		11.72	1.323
180	8.91	9.2	9.5	9.77	10.12		12.15	1.294
200	9.3	9.6	9.91	10.18	10.51		12.57	1.269
220	9.7	10	10.3	10.58	10.9		12.98	1.249
2115	32.2	Flat Plate				32.2	34.24	1.063
6667	57.2					57.2	59.83	1.046

The upper limit of Graetz number (1/x* = 6667) was chosen arbitrarily to serve as the lower limit on depth for the curve fit developed here. At the maximum fully developed laminar Reynolds number (2000) this corresponds to a hydraulic diameter to length ratio of 4.6, an extreme case lying outside the range of practical heat exchanger designs, at which the heat transfer coefficient was assumed to approach the flat plate limit. A similar table showing the same physical bounds was constructed for friction factor, and is shown below as Table 2.2.

Both the Nusselt Number and Darcy friction factor correlations were designed using the functional forms of the 2D duct correlations as the base cases. The nondimensional flow depths for heat transfer and friction factor, x* and x+, are defined below in Equations 2.1 and 2.2. The 2D semi-analytical solutions for heat transfer and Darcy friction factor appear below as Equations 2.3 and 2.4, respectively. The length scale used in the Reynolds number is the hydraulic diameter, which is equal to twice the duct height in the 2D case.

Table 2.2 Curr et al.'s (1972) numerical results for f·Re_{Dh} product, limiting cases and gaps

	α				
1/x+	1	0.5	0.2	small	0.0 (Shah & London)
	Fully Developed				
10	71	76	88		103
11	72	77	89		103
13	72	80	90		104
14	76	82	90		105
17	80	86	92		107
20	86	88	96		109
25	89	92	100		112
33	96	102	108		117
50	112	113	120		128
67	130	129	134		138
100	151	151	154		158
111	160	160	164		164
125	169	169	172		172
143	176	176	180		182
167	190	190	192		195
200	208	208	208		211
250	228	228	232		234
333	244	244	264		268
500	320	320	320		323
1854	600	Flat Plate			600
5247	1000				1000

$$x^* = \frac{x}{D_h \cdot \mathrm{Re}_{Dh} \cdot \mathrm{Pr}} \tag{2.1}$$

$$x+ = \frac{x}{D_h \cdot \mathrm{Re}_{Dh}} \tag{2.2}$$

$$Nu_{2D} = 7.55 + \frac{0.024 \cdot x^{*-1.14}}{1 + 0.0358 \cdot \mathrm{Pr}^{0.17} \cdot x^{*-0.64}} \tag{2.3}$$

$$f_{2D} = \frac{4}{\mathrm{Re}_{Dh}} \cdot \left[\frac{3.44}{\left(x^+\right)^{1/2}} + \frac{24 + \frac{0.674}{4 \cdot x^+} - \frac{3.44}{\left(x^+\right)^{1/2}}}{1 + 0.000029 \cdot \left(x^+\right)^{-2}} \right] \tag{2.4}$$

These 2D expressions (Equations 2.3 and 2.4) were then modified to include dependence on channel aspect ratio, and to approach the known analytical limits of fully developed 3D channel flow and very short depth. For very short depth the flow was forced to approach that of a flat plate, neglecting perpendicular boundary layer interactions

at the channel corners, thus neglecting all aspect ratio dependency at the leading edge. In fully developed channel flow of fixed aspect ratio, the Nusselt number and the product of friction factor and Reynolds number are known functions of the aspect ratio alone, as shown in Equations 2.5 and 2.6 below (Shah and London, 1978).

$$Nu_{FD,rect} = 7.541 \cdot (1 - 2.61\alpha + 4.97\alpha^2 - 5.119\alpha^3 + 2.702\alpha^4 - 0.548\alpha^5) \quad (2.5)$$

$$f_{FD,rect} \cdot \mathrm{Re}_{Dh} = 4 \cdot \left[24(1 - 1.3553\alpha + 4.97\alpha^2 - 5.119\alpha^3 + 2.702\alpha^4 - 0.548\alpha^5)\right] \quad (2.6)$$

Inside these three physical limits, tabular data from Wibulswas (1966) and Curr et al. (1972) for Nusselt Number and friction factor was bridged with an 8-parameter curve fit using least squares approach. The curve fits were weighted in an attempt to achieve a uniform distribution of accuracy. The power law dependence on aspect ratio yielded the best match to the results of Wibulswas (1966) and Curr et al. (1972). The 3D channel heat transfer correlation, constructed using Wibulswas' (1966) results, is discussed first.

2.2.2 3D Channel Heat Transfer

Equation 2.7 shows how Stephan's (1959) expression for 2D flow was first modified to account for aspect ratio by multiplying the first term (7.55 for fully developed flow) by the polynomial correction factor developed by Shah and London (1978). The next step was to add 8 empirical parameters to the second term to capture the effects of aspect ratio in the developing flow regime.

$$Nu_{3D} = 7.55 \cdot (1 - 2.61\alpha + 4.97\alpha^2 - 5.119\alpha^3 + 2.702\alpha^4 - 0.548\alpha^5) + \frac{\left(0.024 + A_1\alpha^{A_2}\right) \cdot x^{*\wedge}(-1.14 + B_1\alpha^{B_2})}{1 + \left(0.03393 + C_1\alpha^{C_2}\right) \cdot x^{*\wedge}(-0.64 + D_1\alpha^{D_2})} \quad (2.7)$$

where $A_1 = 0.247$ $A_2 = 1.049$ $B_1 = -0.1678$ $B_2 = 0.2109$
$C_1 = 0.987$ $C_2 = 0.8556$ $D_1 = -0.06201$ $D_2 = 1.211$

The functional form of this expression for 3D channel flow heat transfer was designed to reduce to the Stephan (1959) correlation when $\alpha \to 0$. Similarly, it reduces to the fully developed rectangular solution (a function of aspect ratio alone) when the nondimensional depth x* becomes large. Wibulswas (1966) presented 70 numerical results for Nusselt number as a function channel aspect ratio $1 < \alpha < 1/6$ and nondimensional depth $10 < 1/x^* < 220$. The curve fit employed this data to give the 3D channel flow correlation the ability to predict heat transfer within the channel geometric limits. Wibulswas' (1966) tabular data was reported to be accurate within a few percent when compared to experimental data for Graetz Numbers (1/x*) less than 70. At larger Graetz numbers (short flow length) the influence of the leading edge analytical bound shown in Table 2.1 is expected to improve the accuracy of the 3D channel heat transfer expression (See Appendix A), but only up to the lower limit of the curve fit (x* = 1/6667).

2.2.3 3D Channel Darcy Friction Factor

Equation 2.8 is the 3D channel Darcy friction factor correlation. It shows how the 2D developing flow equation was modified. Firstly Shah and London's (1978) multiplicative polynomial for the fully developed case was added. Secondly, 8 empirical parameters were inserted into the terms characterizing developing flow. As in the heat transfer case, the parameters were estimated using a least-squares approach. The curve fit was weighted in an attempt to achieve a more uniform distribution in deviations from results by Curr et al. (1972) and flat plate numbers. The curve was fit to points taken from numerical solutions presented graphically by Curr et al. (1972) for $0.002 \le x^+ \le 0.1$, who reported that his results compared well to experimental data taken by Beavers et al. (1970).

Equation 2.8 is formulated to ensure that the physically known limits of 2-D flow and fully developed 3D flow are approached as $\alpha \to 0$ and $x^+ \to \infty$.

$$f_{3D}\,\mathrm{Re}_{Dh} = 4 \cdot \left[\frac{3.44 + E_1 \cdot \alpha^{E_2}}{\left(x^+\right)^{1/2}} + \frac{24 + \dfrac{0.674 + F_1 \cdot \alpha^{F_2}}{4x^+} - \dfrac{3.44 + G_1 \cdot \alpha^{G_2}}{(x^+)^{1/2}}}{1 + \left(0.000029 + H_1 \cdot \alpha^{H_2}\right)\left(x^+\right)^{-2}} \right] \tag{2.8}$$

$$\times (1 - 1.3553\alpha + 4.97\alpha^2 - 5.119\alpha^3 + 2.702\alpha^4 - 0.548\alpha^5)$$

where

E_1=2.359 E_2=0.5553 F_1=3.434 F_2=4.001
G_1=3.42 G_2=3.204 H_1=0.001163 H_2=10000

To ensure that the correlation approached the flat plate limit, the 2D friction factor correlation (Equation 2.4) was used as the limit for small x+ (below 0.002) for all aspect ratios. The curve fit of Curr et al.'s (1972) results included a range of x+ values from 0.1 to 0.002 for aspect ratios of 0.2, 0.5, and 1. At the minimum x+ value of 0.002 the friction factor-Reynolds number product had approached the same value for all aspect ratios. This indicates that the flat plate situation has been reached near the leading edge because the boundary layer interactions at the corners have not yet developed to a point where they have a significant effect on friction. The accuracy of the 3D channel friction factor is believed to be better with small aspect ratios and large x+ values due to the constraints imposed by Equations 2.4 and 2.6.

2.2.4 3D Channel Correlation Predictions

Figure 2.1 shows how the 2D and 3D channel flow heat transfer coefficients and friction factors vary with flow depth and approach the flat plate solution as x*, $x^+ \to 0$. Reducing non-dimensional depth by decreasing heat exchanger depth has the same effect on heat transfer as increasing hydraulic diameter.

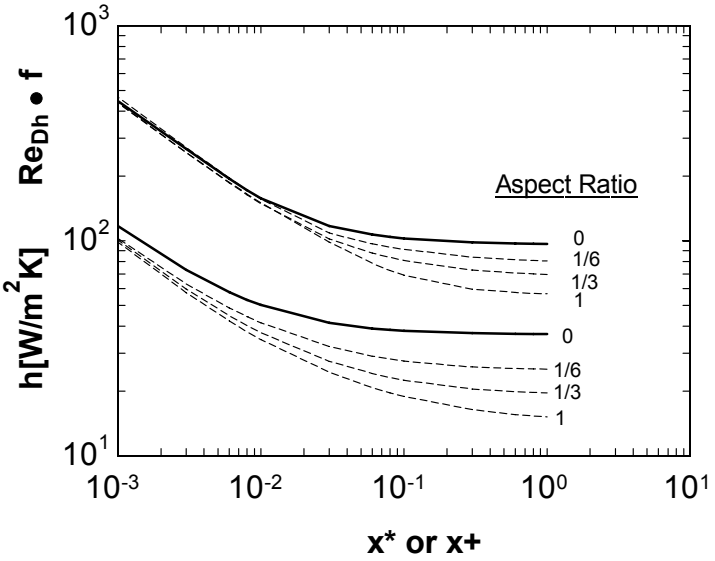

Figure 2.1 Heat transfer coefficient and $f \cdot \mathrm{Re}_{Dh}$ product dependence on flow length and aspect ratio.

The Stephan (1959) heat transfer correlation (zero aspect ratio channels) is shown by the solid line and represents an upper bound for all channel flows. The lower set of dashed lines is calculated using the 3D channel flow heat

transfer correlation for 3 aspect ratios ranging from 1 to 1/6. As aspect ratio gets smaller, the 3D channel flow heat transfer coefficient approaches the Stephan (1959) correlation as expected. All aspect ratios approach the fully developed flow result as x* becomes larger. Moving to a larger the channel aspect ratio lowers the heat transfer coefficient, an effect that is accentuated for large x*. The 3D channel flow heat transfer correlation appears above as Equation 2.7.

The heat transfer coefficient lines correspond to x* and the friction lines correspond to x+. The upper set of lines in Figure 2.1 compares the product of Reynolds number and friction factor predicted by the 3D channel friction correlation (dashed lines) to those for the 2D duct (solid line). The product of Reynolds number and friction factor is largest at small x+, reflecting the thinner boundary layer. Smaller aspect ratios produce higher friction factors due to larger velocity gradient at the wall in fully developed flow. Near the leading edge of the fins (small x+) aspect ratio has little to no effect on friction because the boundary layers have not yet grown thick enough to interact.

2.3 3D Channel Flow Correlation Accuracy

Tables 2.3 and 2.4 show the percent deviations between the correlations developed here, and the tabulated analytical results of Wibulswas (1966) and the numerical results of Curr et al. (1972). Recall that their results were reported to lie within a few percent of experimental data. These Tables quantify the additional uncertainty attributable to our curve fits that cover the broadest parameter range and converge to known physical limits at the maximum and minimum heat exchanger depths and at an aspect ratio of zero. The last two x* values in Table 2.3 extend beyond Wibulswas' (1966) results. These are flat plate values where the accuracy of the 3D channel heat transfer correlation is compared the heat transfer from a flat plate. Similarly the last three x+ values in Table 2.4 extend beyond Curr et al.'s (1972) results. These are flat plate values where the accuracy of the 3D channel friction factor correlation is compared to the friction factor of the 2D duct (Equation 2.4). At this low x+ a flat plate and a channel of any aspect ratio will have the same friction factor.

Table 2.3 Percentage deviations: 3D channel heat transfer

			α		
1/x*	**1**	**0.5**	**1/3**	**0.25**	**1/6**
10	-1.9	-1.8	0.2	0.9	1.9
20	-3.3	-2.8	0.3	1.3	2.3
30	-3.2	-2.5	0	1.7	2.7
40	-2.3	-2.1	0.2	1.9	2.9
50	-1.6	-1.7	0.5	1.5	3
60	-0.9	-1.4	0.3	1.6	2.9
80	-0.4	-1.4	0.4	1.2	2.3
100	0.5	-1.1	0.2	1	2.1
120	0.9	-0.8	0.3	0.6	1.7
140	1.5	-0.6	0	0.4	1.5
160	1.9	-0.3	-0.1	0.3	1
180	2.2	0	0	0.1	0.7
200	2.6	0.1	-0.2	-0.1	0.5
220	2.6	0	-0.3	-0.4	0.1
2115	-4.4	-4.4	-4.6	-4.8	-5.1
6667	0.9	3.1	3.3	3.2	2.7

The accuracy of Wibulswas' calculations were within a couple of percent for Graetz numbers $1/x^* < 70$. For larger Graetz numbers the heat transfer coefficient approaches that of a flat plate. Physically, the heat transfer from a 3D channel must lie between that of a flat plate and the 2D Stephan (1959) correlation, but Wibulswas took no experimental measurements in that region. The maximum error in the Nusselt number curve fit is ±5%. The RMS error of the curve fit is 1.5% and the individual errors appear in Table 2.3. Negative values in the table indicate an underestimation by the curve fit, most prevalent at aspect ratios of 1 and 0.5. The only limit on the 3D channel heat transfer correlation is that the nondimensional depth x^* be greater than 1/6667.

Table 2.4 Percentage deviations: 3D channel friction

	α		
1/x +	**1**	**0.5**	**0.2**
10	-0.9	2.6	3.5
14	0.4	0	5.2
17	-0.6	-1.6	5.7
20	-2.6	-0.8	4.3
25	0.5	0.2	4.2
33	2.5	-2.4	2.5
50	1.1	-0.5	2.3
67	-3.1	-3.6	0.2
100	-2	-2.7	1.2
125	-3.5	-3.7	-0.6
143	-1.9	-1.7	0.7
167	-2.6	-2.2	1.4
200	-3.4	-2.7	1.6
250	-2.1	-1.3	1.2
333	4.7	5.1	1.8
500	-2.9	-3.7	1.7
1000	-2.2	-4.9	1.2
1854	-1.1	-4.9	1.5
5247	-0.3	-4.9	1.7

Numerical data from Curr et al. (1972) was used to fit the 8 constants appearing in the 3D correlation. The 3D channel friction factor correlation (Equation 2.8) was found to approximate Curr et al.'s (1972) data with a RMS error of 2.7% and a maximum error of ±6% at an aspect ratio of 0.2 and an x^+ of 1/17. The only limit on the 3D channel friction factor correlation is that the nondimensional depth x^+ be greater than 1/5247.

2.4 Air Conditioning Microchannel Condenser Optimization

The channel flow correlations described above were used in a numerical experiment to simulate a microchannel heat exchanger with plain fins. The experiment compares two air conditioning systems. Both have the same compressor, throttle valve and evaporator, but have different condensers. Both condensers are of the microchannel tube variety, one with plain fins and one with louvered fins. The objective function, system power, was minimized and the same seven condenser inequality constraints were chosen as search variables for both condensers: Fin height, fin pitch, fin thickness, face velocity, depth, web thickness, and port diameter. Even with only the condenser geometry changing, system power changes considerably.

2.4.1 System model

The objective is to find the optimal values of the search variables that lead to minimum system power. The system model was constructed in Engineering Equation Solver with cooling capacity held constant at the ARI-A rating condition. This leads to the fact that minimizing system work is equivalent to maximizing system COP.

Table 2.5 Equality constraints for louvered and plain fin base case condenser system models

Parameter	Equality Constraint
A_{face} [m^2]	1
ΔT_{sat} [C]	1
Q [kW]	10.5
Subcooling [C]	5
Superheat [C]	5
$T_{outdoor}$ [C]	35
T_{evap} [C]	12
Tube end thickness [mm]	0.42
W_{evap} [kW]	0.4
k [W/mK]	237
η_{fan}	10%
η_{comp}	70%

The system simulation model consisted of a finite element microchannel condenser, a simplified evaporator, an adiabatic compressor represented by constant isentropic motor efficiencies, and isenthalpic expansion. System equality constrains appear in Table 2.5. The condenser finite elements allowed the solution to march along the refrigerant flow direction so that local two-phase heat transfer and pressure drop of the refrigerant could be accurately modeled.

The core face area was constrained to 1 m^2, otherwise it would increase without bound to improve performance. A saturation pressure drop (ΔT_{sat}) constraint was imposed to ensure that the optimal circuiting to ensure that in-tube pressure drop was larger than header pressure drop, to minimize refrigerant flow maldistribution among many parallel microchannel tubes. This allows for some tradeoff between tube length and the number of tubes, while allowing the aspect ratio of the condenser to be controlled by serpentining the tubes (i.e. multiple passes per tube).

The simplified evaporator model was implemented using simple energy balance and fluid property equations, neglecting pressure drop. Because only the condenser geometry is being changed, it is sufficient to include a simple evaporator model and use a constant estimate of the evaporator fan work.

2.4.2 System Power and Condenser Mass

Figure 2.2 shows how the minimum system work varies with condenser mass. Adding mass increases the airside area and is beneficial up to a point, although this point may lie beyond the best economical condenser mass. Plain fins show better performance, perhaps because the plain fin correlations are not empirically constrained while the louvered fin correlations were at every point. It is not clear whether or not louvered fins would show much better performance if unconstrained. For plain fins, as mass is increased, the optimization tends to spread the fins and tubes

apart and make the fins thicker. At 10 kg, the optimal plain fin condenser has a fin pitch of 1.2 mm, a fin height of 14 mm, and a fin thickness of slightly over 0.06 mm. Moving to 15 kg the fin pitch, fin height, and fin thickness increase by 31%, 7%, and 3%, respectively, while system power also decreases 1%. Also, the face velocity is decreased 4% from 1.5 m/s to maintain low pressure drop at 97% increased depth.

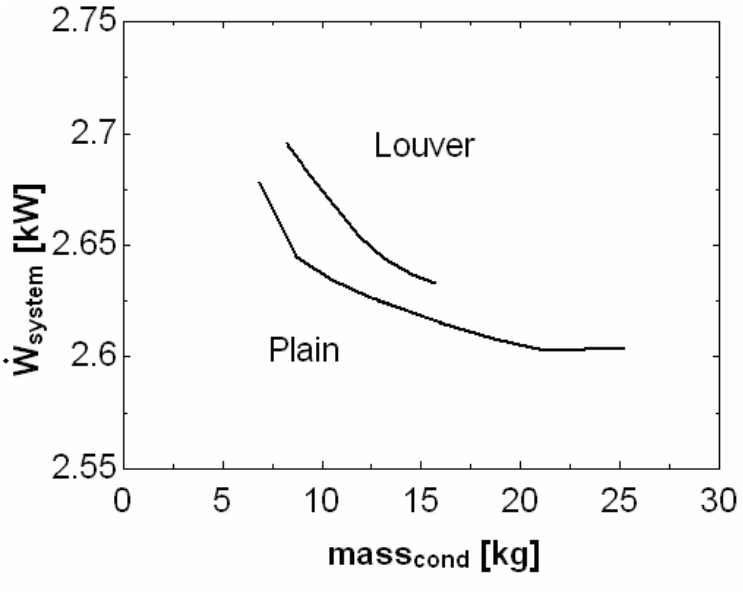

Figure 2.2 Optimal system work for plain and louvered fins

In the case of louvered fins, the optimization tends to spread the fins apart as mass is increased. Fin height and thickness do not change because they remain at their empirically-defined lower bounds of 8 and 0.06 mm. All correlation bounds appear in Table 2.6 below. Moving from 10 to 15 kg the fin pitch increases 10% to the upper bound of 2.2 mm. Face velocity varies erratically as additional geometric constraints are encountered. Maximum performance is achieved at the maximum depth.

Table 2.6 Empirical louvered and semi-empirical plain fin correlation limits.

Louvered	Variable	Plain	
Upper	Name	Lower	Upper
2.2	Fin pitch [mm]	1*	None
0.16	Fin thickness [mm]	0.06*	None
19	Fin height [mm]	None	None
None	Port diameter [mm]	0.6*	None
None	Web thickness [mm]	0.2*	None
44	Core Depth [mm]	None	None
None	Face velocity [m/s]	None	None

The plain fin condenser optimization was limited only by manufacturing constraints specified for web thickness and port diameter. These limitations were minimal as discussed below.

2.4.3 Louvered fin condenser optimization

The complex air flow caused by louvered fins is very difficult to solve analytically. For this reason empirical correlations are used. The Chang and Wang (1997) correlations were used to find the air side heat transfer coefficient and pressure drop. The bounds of the Chang and Wang (1997) parameter space were selected where the data was within 90-100% of the maximum and minimum values of the correlation, depending on data density. When seeking an optimal design, the empirical correlations will return a result at the edge of the parameter space if the true optimum lies outside the correlation bounds. This situation illustrates the fundamental limitations of an empirical correlation: they cannot be accurately extrapolated to predict performance of heat exchangers that have not yet been designed and tested. For example, the Chang and Wang (1997) correlation cannot be used to predict the performance of a heat exchanger deeper than 44 mm because all coils in the underlying data base were 44 mm or thinner.

The limitations of the empirical correlations for louvered fins became evident as the optimization algorithm sought to minimize system power. Six of the seven search variables were constrained by their respective upper or lower limits when mass is equal or greater to 15.7 kg, indicating that the true optimum lies outside of the parameter space. Adding more mass does not help because depth is already at the upper bound, therefore adding mass simply increases fan power. Only face velocity attained an intermediate value of 1.59 m/s at this mass. Also, the accuracy of the attainable optimum is questionable: while it lies within the correlation's stated bounds, no heat exchanger tested lies near that "optimal" corner of the parameter space (See Appendix A).

An interior optimum will occur where the absolute value of the partial derivatives with respect to search variables of condenser fan power equals that of compressor power. For the most energy efficient (most massive) design, core depth and fin pitch went to their upper limits (44 and 2.2 mm) while fin height, fin thickness, port diameter, and web thickness went to their lower limits (8, 0.06, 0.6, 0.2 mm) for this and all optimal designs of Figure 2.2. Louver geometry was not changed because it was found that the minimum louver pitch and maximum louver angle (1 mm and 23°) were always optimal. Port diameter, fin thickness, and web thickness were limited by manufacturing constraints. Fin pitch, fin height, and core depth were limited by underlying empirical data set. Thus further optimization would be possible by improving manufacturing methods or extending the range of the correlations. With the 7 search variables optimized within the constrained limits, the lowest system work achievable is 2.63 kW at 15.7 kg.

2.4.4 Plain fin condenser optimization.

The optimal configuration for plain fins was found to lie far outside the parameter space that constrained the louvered fin optimization. The only binding constraints were the manufacturing-related lower bounds on port diameter and web thickness. Recall in the case of louvered fins it was optimal to reduce fin height and increase fin pitch in order to minimize air-side pressure drop by increasing aspect ratio. With plain fins the optimal strategy is to increase fin height to improve heat transfer by decreasing aspect ratio, while using the minimum fin thickness in almost every case as mass is added. Fin pitch increases only slightly as mass is added. The material savings resulting from taller, more widely spaced fins is used to add area by making core deeper.

Exploiting the lower pressure drop associated with plain fins, heat transfer coefficient is maximized by reducing channel aspect ratio by increasing fin height, and area is increased by increasing core depth. Fin pitch increases as the core gets deeper and more massive, but it reaches a maximum of only 2 mm at a mass of 25 kg due to the low pressure drop of plain fins.

Table 2.7. Optimal designs for plain and louvered 10-kg condensers

Louvered	Variable	Plain
2.1	Fin pitch [mm]	1.2
0.06	Fin thickness [mm]	0.06
8	Fin height [mm]	14
0.6	Port diameter [mm]	0.6
0.2	Web thickness [mm]	0.2
32	Core Depth [mm]	39
1.75	Face velocity [m/s]	1.5

2.4.5 Sensitivity analyses

Sensitivity analyses were conducted for 10 kg condensers, to examine the effects of relaxing some of the constraints. A different optimal design is reached when the optimization is repeated with each of the altered constrains shown in Table 2.8. The results summarized in Table 2.8 shows that increasing face area while keeping mass constant) shows an increase in performance. This is due to more heat transfer area and lower pressure drop allowing for a larger heat sink. Switching to softer alloy for fin material would have only small impacts on system performance. Interestingly, the optimal fin thickness remains at its lower bound as fin height or pitch can offset the change in fin efficiency.

Far greater benefits are obtainable by increasing fan/motor efficiency from 10 to 30%. The optimal face velocity increases significantly, providing a larger heat sink to reduce condensing temperature directly. The higher velocity also increases heat transfer coefficient, allowing decreased fin height and fin pitch, thus increasing air side area. The higher pressure drop is more than offset by the high fan efficiency (See Appendix B).

Table 2.8 Sensitivity of system power [W] to design constraints for 10 kg condensers

	Baseline system power	A_{face} = 1.5 m^2	η_{fan} = 30%	k = 160 W/mK
Louvered fins	2673 -	2546 -4.8%	2499 -6.5%	2646 -1.0%
Plain fins	2636 -	2517 -4.5%	2460 -6.7%	2646 0.4%

Finally, to gain more detailed insights into the tradeoff between heat transfer and pressure drop the optimization was repeated for multi-layer heat exchanger configurations that re-started the plain-fin boundary layer several times. The results shown in Figure 2.3 show clearly that the pressure drop penalties exceed the heat transfer benefits. The case of slit fins might represent the limiting case as the number of layers gets very large.

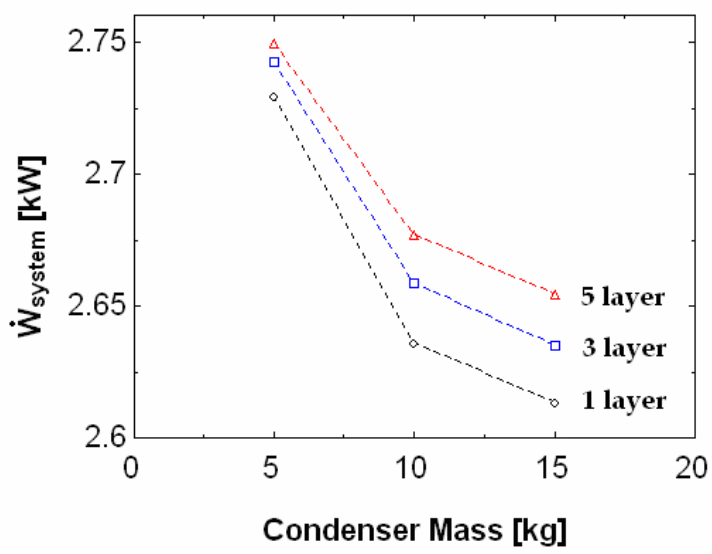

Figure 2.3. Minimum system work vs. condenser mass for crossflow condensers

Another analysis considered the system performance improvement achievable by arranging the layers in a cross-counterflow configuration, a strategy that has proven very successful for gas coolers in the transcritical carbon dioxide cycle (Bullard et al. 2002). However in this subcritical system the benefits of counterflow circuiting barely offset the disadvantages illustrated in Figure 2.3, failing to justify the incremental cost of a multilayer design.

2.5 Microchannel Heat Exchanger Economic Tradeoffs

The following economic analysis assumes $4/kg for aluminum fins and tubes, $0.10/kWh, and 1000 hours of operation per year. The material cost of both the plain and louvered fin 10 kg condensers is $40. The plain fin condenser uses 2.64 kW and the louvered fin condenser system uses 2.67 kW. This translates to a power savings of 30 W and a monetary savings of $3 per year.

Increasing mass almost always improves performance, but the economic optimum is related to the local slope of the curves in Figure 2.2. For the plain fin condenser, the slope at 10 kg reflects a 4 to 5 year simple payback period, while the steeper curve for the louvered case justifies the use of at least 12 kg using under the same payback criterion. When cost is held constant and system power is minimized, almost the same configuration is reached for a given mass. This is true even when the relative price of tubes and fins varies. The configuration will decrease the amount of tube or fins, relative to the other, depending on which is more expensive. The effect of trading fin mass for tube mass (or via versa) due to cost is very small. The main effect of constraining cost with different fin and tube prices is that the optimization will use more of the less expensive material in order to gain mass (See Appendix B).

Material and manufacturing constraints are discussed in more detail in Chapter 4.

Chapter 3. Round Tube Heat Exchangers

3.1 Round Tube Heat Exchangers Introduction

The purely empirical correlations currently used to characterize air-side heat transfer and pressure drop in round-tube heat exchangers are based on data taken over several decades by several investigators, using samples of production and prototype heat exchangers that reflected the technologies that were dominant at the time. As new technologies enable the use of smaller tube diameters and thinner fins in air conditioning, or new applications such as heat pumps, such correlations cannot be used to identify or analyze potentially optimal configurations that may lie outside the historically-defined parameter space. Unless the functional form of a correlation accurately reflects the physics of the flow; the Buckingham pi theorem cannot produce nondimensional variables that can be used to extrapolate beyond the dimensional limits of the underlying data set.

This chapter takes a physically-based approach to developing a heat transfer correlation that deals only with plain fins. The goal is to provide a functional form capable of being extrapolated to such well-known limiting conditions as fin arrays or tube banks, explicitly representing physical phenomena that tend to dominate heat transfer when fin pitch is large: e.g. developing flow and vortices shed from tubes and tube-fin junctions. A broader goal is to establish a mathematical framework that is also capable of representing the very different physical phenomena observed at small fin pitch, as in a/c evaporators and condensers.

Preliminary analyses using a system simulation model to optimize condenser geometry for a typical 10.5 kW split a/c system at the ARI-A design condition illustrated the inherent limitations of published correlations. The objective was to maximize system efficiency subject to a constraint on heat exchanger mass. For one-row heat exchangers the optimization algorithm was constrained by the lower bound on fin pitch, and for multi-row heat exchangers it was quickly constrained by upper bounds on both tube and fin pitches. Given the growing need to design heat pumps that can operate efficiently under frosting conditions, and the inability to extrapolate published correlations to larger tube and fin pitches, the analytical focus shifted to characterizing the physical phenomena that dominate heat transfer in such coils.

The analytical and semi-empirical solutions developed by Stefan (1959) and Zukauskas and Ambrazyavichyus (1972) for fin arrays and tube banks, respectively, serve as a starting point for developing a mathematical expression that approaches those limits as tube or fin pitch increases. Ichimyia (1988) measured temperature profiles at constant heat flux on a duct wall created by root vortices formed at the fin-tube junction, and observed heat transfer enhancements far greater than those observed by Saboya and Sparrow (1974) in naphthalene sublimation experiments at small (<3 mm) fin pitch where the fin interactions tend to dissipate both spanwise and streamwise vorticity rather quickly, leaving a long stagnant wake downstream of the tubes. Kawamura et al. (1984) showed that the presence of fins have little effect on heat transfer from the tubes, thus simplifying the task of incorporating interaction effects into a physically-based formulation.

There is relatively little published data for heat exchangers having fin pitch of the same order of magnitude as the tube diameter. Kim and Kim (2005) conducted experiments on a family of prototype heat exchangers having 10 mm tubes with identical pitch, with fin pitch varying between 7 and 15 mm, and tube rows from 1 to 4. As other experiments have shown, those with staggered tubes outperformed the inline prototypes, so this analysis focuses only on the former. Subsequent to publication the authors have developed separate curve fits for their staggered tube data, and separate correlations for their one-row and multi-row prototypes, reducing their RMS error to ~1%

(Kim and Kim, 2005). Those curve fits are used in this paper as surrogates for the underlying unpublished data, to test our semi-empirical model.

Granryd (1965) accumulated a much larger set of data spanning a much larger part of the parameter space where fin pitch exceeds 3 mm. Again, the data were not published so only the correlations are available as a basis for evaluating our physically-based approach. Unfortunately due to Granryd's (1965) focus on refrigeration coils having relatively large tube diameters and face velocities, the data sets do not overlap Kim and Kim's (2005). Moreover only a small fraction of the data had fin pitch greater than half the tube diameter. Granryd's (1965) semi-empirical approach, however, is consistent with ours, as it estimates empirical parameters to capture the effects of small fin pitch while allowing extrapolation to tube banks and fin arrays.

The following sections describe the first steps towards development of a single correlation for air-side heat transfer in single-and multi-row heat exchangers that can cover the entire parameter space with one continuous function. Such a formulation is required for compatibility with commonly used optimization algorithms that may be applied to heat exchanger and system design. The approach described below begins with a simple superposition of a fin array and tube bank, and then draws upon various experimental investigations to add empirically-based terms to account explicitly for the streamwise vortices that form at fin-tube junctions and the spanwise von Karman vortex streets shed from the tubes. This chapter uses data and a figure (Figure 3.2) taken from Ichimiya et al. (1988).

3.2 Methodology

Equation 2.3 is Stephan's (1959) semi-empirical expression for simultaneously developing flow in a 2-D duct with an isothermal boundary; it has been found to fit numerical solutions within 3% (Kakac, et al. 1987). It is shown again as Equation 3.1 for convenience. Equation 3.2 for staggered tube banks quantifies the heat transfer enhancement experienced by downstream tube rows as a result of the von Karman vortex streets shed by the first and subsequent rows.

$$Nu_{2D} = 7.55 + \frac{0.024 \cdot x^{*-1.14}}{1 + 0.0358 \cdot \mathrm{Pr}^{0.17} \cdot x^{*-0.64}} \qquad \text{where} \qquad x^* = \frac{depth}{D_h \cdot \mathrm{Re}_{Dh} \cdot \mathrm{Pr}} \tag{3.1}$$

Superposition of such flow fields requires an assumption of linearity that could only be justified at large fin or tube pitch where interactions could be neglected. The analysis presented in the next section begins with this simple case, and then proceeds to model a subset of interaction effects, perhaps ironically by employing a superposition approach.

This basic assumption follows from the fact that the large-scale flow fields produced by vortices are routinely analyzed using potential flow theory, as the most significant viscous effects are localized in the vortex core. The Zukauskas and Ambrazyavichyus (1972) correlation quantifies the effects of the vortex streets shed from tubes as their transverse velocity components enhance heat transfer on the tube surfaces that lie downwind. It also quantifies the viscosity-driven decay of those vortex streets as they are convected downstream through the tube bank. Therefore we assume *for large fin pitch* that this heat transfer enhancement mechanism operates in a simple additive manner as the vortex-induced components of velocity combine nondestructively with the streamwise laminar flow field between two widely-spaced parallel plates. At small fin pitch, however, the viscous core of the vortices is dissipated quickly due to the proximity of the tube walls, so the large-scale flow structures are unable to form and be carried downwind where they can enhance heat transfer on tube and fin surfaces.

Empirical data are also available to characterize the heat transfer-enhancing effects of the horseshoe vortices formed at the root of a cylinder protruding from a wall, normal to the air flow direction. In inviscid potential flow, the two streamwise vortices would begin to diverge from one another under the influence of the other's far-field velocity vector. For a similar reason the vortices would quickly move away from the wall, as if it were pushed away by a mirror image vortex on the opposite side of the wall. With the vortices thus removed from the dissipating effects of nearby surfaces, their large-scale velocity fields are carried downstream and their spanwise velocity component is available to enhance heat transfer on the duct walls. Similarly, their velocity components normal to the walls can bring fresh air into the thermal boundary layer that would otherwise be thickened as the laminar flow proceeded through the duct.

Ichimiya et al.'s (1988) experiments using acrylic cylinders of various diameters located in fully developed laminar flow through duct produced valuable insights into the nature of the heat transfer enhancements associated with root vortices. Even in laminar flow, most of the enhancement occurred on the wall near the root of the cylinder where the viscous core of the vortices were close to the surface and the transverse velocity components were relatively large. However there were also heat transfer enhancements of substantial magnitude extending more than 5 tube diameters downwind, as the large-scale flow field of the streamwise vortex was carried downwind. When fin pitch is large the viscous effects (scouring near the tube root, and rate of decay downstream) are represented by a simple additive empirical curve fit of heat transfer enhancement factor expressed by Ichimiya et al. (1988) as a function of downstream distance and enhanced area, normalized with respect to tube diameter and linearly interpolated between Reynolds numbers of 1000 and 2000 based on tube diameter.

Finally experiments by Kawamura et al. (1984) demonstrated that the root vortices have only a small effect on the tube heat transfer, so that effect is neglected. In any event for most heat exchanger geometries tube area is only a small fraction of the total, diminishing the effect of their area-weighted contribution. The next section describes in detail how the semi-empirical correlation is constructed from the analytical and empirical results described above.

3.3 Semi-Empirical Correlation for Large Fin Pitch

The basic framework of the correlation involves a simple area-weighted averaging of the fin and tube heat transfer coefficients. Since the effect of the fins on the tubes is neglected, all interaction effects are embodied in the multiplicative enhancement factor applied to the fin heat transfer coefficient.

$$h_{air} = \frac{EF_{fins} \cdot h_{fins} \cdot A_{fins} + h_{tubes} \cdot A_{tubes}}{A_{fins} + A_{tubes}} \tag{3.2}$$

To account for local variations of the heat transfer coefficients and the enhancement mechanisms, the fin is divided into $N_{rows} + 1$ segments as illustrated in Figure 3.1 for a 4-row heat exchanger. Next, these local results are then aggregated as shown in Equation 3.3.

$$EF_{fins} = \frac{\sum_{i=2}^{N+1} EF_i \cdot h_{loc,i} \cdot A_i}{h_{fin} \cdot A_{fin}} \tag{3.3}$$

In the fin section at the upstream tube-fin junction, the heat transfer coefficient $h_{loc,i}$ is evaluated by differentiating Equation 3.1 for a 2-D duct and the local velocity $V_{channel}$, which is simply the face velocity adjusted for the

blockage effect of the fin thickness. The position of these local heat transfer coefficients is shown in Figure 3.1. By definition, $EF_1 \equiv 1$ for area A_1 because all fin-tube interaction effects are assumed to occur downstream of the first tube row. Therefore, A_1 is not included in Equation 3.3.For all other segments starting with area A_2, the local enhancement factor is computed as follows:

$$EF_i = (EF_{Ichi,i} - 1)\frac{A_{enh,i}}{A_i} + EF_{Z,i} \tag{3.4}$$

where EF_{Ichi} is from Ichimiya et al. (1988) and applies only to the $A_{enh,i}$ enhanced by the horseshoe vortex extending downwind of a tube in row i, and $EF_{Z,i}$ is local enhancement factor observed by Zukauskas and Ambrazyavichyus (1972) on the surface of a tube in row i, representing the cumulative effect of all the vortex streets shed from upstream tube rows. The following subsections treat 1-row and multi-row heat exchangers separately, because the vortex flow patterns differ significantly.

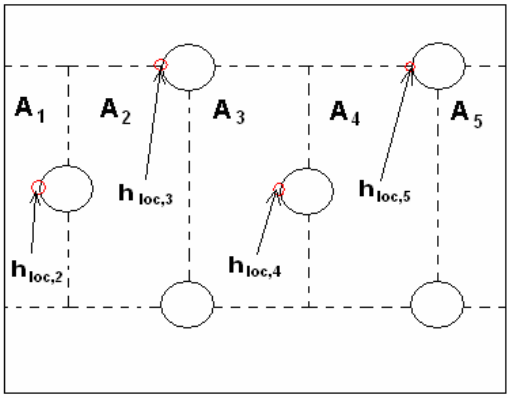

Figure 3.1 Area elements in fin section

3.3.1 One tube row

Figure 3.2 illustrates the shape of the wake region observed by Ichimiya et al. (1988) on the wall downstream of a cylinder when fin pitch is large. The contours show how heat transfer is enhanced throughout the wake region when $Re_{Dc} \geq 1000$; greater enhancement was observed at larger Reynolds numbers.

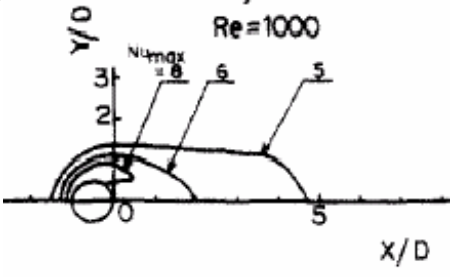

Figure 3.2 Iso-Nusselt number lines observed by Ichimiya et al. (1988)

The wake region observed by Saboya and Sparrow (1974, 1976) at smaller fin pitch had generally the same shape, but enclosed a large stagnation region where heat transfer was severely degraded. In both cases the wake region extended more than 4 tube diameters downstream, beyond the trailing edge of any one-row heat exchanger. These observations form the basis for our decision to attribute the heat transfer enhancement to the transverse velocity component generated by the horseshoe vortex when fin pitch is large, and to conclude that small fin pitches

confine the vortex to a small diameter along the shear layer separating the stagnation region from the free stream where $V=V_{max}$. Since the overall length and width of the wake region is the same, the same maximum velocity is assumed to prevail outside the wake when fin pitch is large. Accordingly the local enhancement factors in Equation 3.4 are applied to local heat transfer coefficients in A_2 and A_3 that are calculated using $V_{channel}$ and V_{max}, for the first and second tube rows respectively, as are the enhancement factors in Equation 3.6.

The equation for the enhanced area, taken from Figure 3.2, is given by Equation 3.5 and the associated enhancement factor, which fits 9 data points from Ichimiya et al. (1988) ±1%, is given by Equation 3.6.

$$A_{enh} = 2 \cdot D^2 \cdot (1.8 + 1.35 \cdot (X / D)) \qquad \text{X/D} \le 4 \tag{3.5}$$

$$A_{enh} = 2 \cdot D^2 \cdot (1.8 + 1.35 \cdot (X / D) + (X / D - 4)) \qquad 4 < \text{X/D} \le 5$$

$$EF_{Ichi} = A_1 \cdot (X / D) + A_2 \cdot (X / D)^{A_3} + B_1 \cdot \text{Re}_{Dh} \tag{3.6}$$

where A_1 = 8.913e-3, A_2 = 1.122, A_3 = -8.692e-2, and B_1 = 8.658e-5.

When applied to Equation 3.4 for area A_2, the enhanced area equation is simply truncated at the trailing edge (because no further area exists for a one row core), and the enhancement factor in Equation 3.6 is evaluated at X/D corresponding to the trailing edge. Since Ichimiya et al.'s (1988) experiment with a single cylinder measured the combined effect of the spanwise vortex street as well as the streamwise horseshoe vortex that formed at the root, it is not necessary to treat these phenomena separately in the case of a one-row heat exchanger.

3.3.2 Multi-row heat exchangers

The same equations apply to the case of deeper heat exchangers, with a few adjustments to reflect the fact that air flowing at V_{max} between the tubes of row 1 is divided and diverted as it approaches the staggered tubes of row 2. The two streams converging to pass between the tubes of row 2 therefore confine the wake of tube 1 to area A_2, confining its heat transfer-enhancing root vortex to that small area instead of letting its effect to be distributed less intensively over a larger area. To quantify this effect, the term $EF_{Ichi}A_{enh}$ in Equation 3.4 is evaluated by setting X/D=5, reflecting an admittedly crude but physically-based assumption that all the incremental heat transferred from the spanwise flow generated by the horseshoe vortex is confined to A_2 along with all the vorticity.

The second adjustment is rather straightforward, calculating the local heat transfer coefficients in Equation 3.4 using V_{max} for all segments downstream of A_1. Since all downstream tube rows face V_{max} instead of $V_{channel}$ due to the blockage effects of both the tubes and the wakes, the downstream tube rows generate stronger spanwise and streamwise vortices, consistent with the findings that of both Zukauskas and Ambrazyavichyus (1972) and Saboya and Sparrow (1976). Therefore V_{max} was used to calculate the enhancement factors starting with row 2. After the last row of tubes, the wake and its effects are truncated at the trailing edge, exactly as in the case of a one-row heat exchanger.

Finally the enhancement factor associated with the vortex streets shed by all tube rows is obtained directly from Zukauskas and Ambrazyavichyus' (1972) correlation for staggered tube banks having N rows.

$$Nu_D = C_2 \cdot C \cdot (\text{Re}_{D,\max}{}^m) \cdot \text{Pr}^{0.36} \cdot \left(\frac{\text{Pr}}{\text{Pr}_{surface}} \right)^{0.25} \tag{3.7}$$

where the average multipliers (C_2 in Equation 3.7) are given in Table 3.1. C is a function of tube pitch. Recall, however, that Ichimyia's experiments quantified the near-field enhancement effect of the vortex on the fin area lying

immediately downstream of the tube. However it is clear from Table 3.1 that the vortex streets shed by upstream tube rows continue to enhance heat transfer far downstream. From the average enhancement factors shown in the table, it is straightforward to compute a local enhancement factor Z_i experienced by the tubes in each row i, relative to the heat transfer coefficient for tubes in row 1. In a 3-row heat exchanger, for example, the factor Z_i is applied to tube surfaces in row 3 and fin surfaces A_4.

Table 3.1 Tube row multipliers

Number of Rows	Zukauskas (1972) Average Multiplier
1	0.68
2	0.75
3	0.83
4	0.89
5	0.92
6	0.95
7	0.97
8	0.98
9	0.99
10	1

3.4 Round Tube Heat Exchangers Correlation Discussion

3.4.1 Semi-empirical heat transfer model

Heat transfer coefficients predicted by this physically-based approach compare well to empirical correlations at large fin pitch. Figure 3.3 compares the results of Equation 3.2 for the heat exchanger prototype tested most extensively by Kim and Kim (2005) to their own empirical correlation, which can be viewed as a surrogate for data since its accuracy is ±1%. Figure 3.3 encompasses their entire range of face velocities and number of tube rows at 10 mm fin pitch. The largest discrepancy between the two correlations (5%) occurs at one row and high face velocity, and the RMS error is 2%.

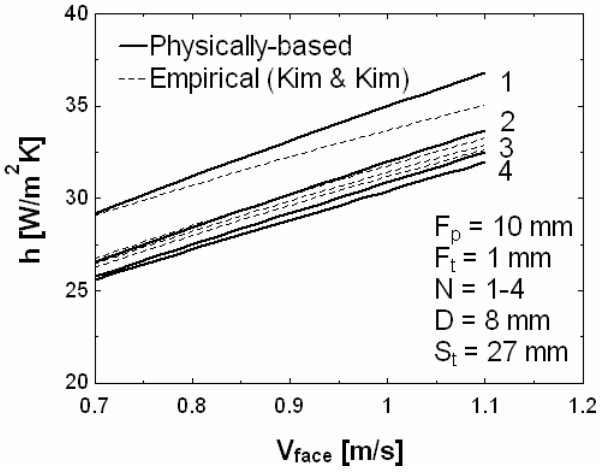

Figure 3.3 Comparison with Kim and Kim (2005)

While the data set at 10 mm fin pitch was dense, at the other fin pitches (7.5, 12.5, and 15 mm) it was limited to 1- and 2-row heat exchangers only. Nevertheless at 7.5 mm fin pitch, our semi-empirical correlation

overestimates Kim & Kim's predicted heat transfer by a maximum of 10% (for one row and 1.1 m/s face velocity) and the RMS error is 8%. On the other hand the agreement is much better 12.5 and 15 mm fin pitch, where RMS errors are 2.7% and 3.6%, respectively. This trend is consistent with the physical assumptions underlying the semi-empirical approach: that closely-spaced fins dissipate the horseshoe vortices more rapidly, and at high fin pitch the velocity fields generated by the streamwise and spanwise vortex cores are additive, and therefore their heat transfer enhancements are additive.

Figure 3.4 is a comparison with Granryd's (1965) correlation, which again serves only as a surrogate for the underlying data because the detailed experimental results are unpublished. The geometric parameters for the 2- and 3-row cases are taken from Granryd's (1965) data set, but the 1-row prediction reflects data from prototypes having different fin and tube geometries. Again the agreement is good, even at this relatively small fin pitch where the vortices begin to dissipate more quickly. Most of Granryd's (1965) data covered tube diameters up to 35 mm and fin pitches down to 3 mm, and the majority of the heat exchangers had inline tube arrangements. Therefore the resulting empirical correlation is influenced by stagnation regions in many of the tube wakes, and wakes that extend to the next tube row. This may account for the relatively strong row dependence seen in Granryd's (1965) correlation, compared to the weaker dependence seen in Kim's staggered tube correlation and our semi-empirical results.

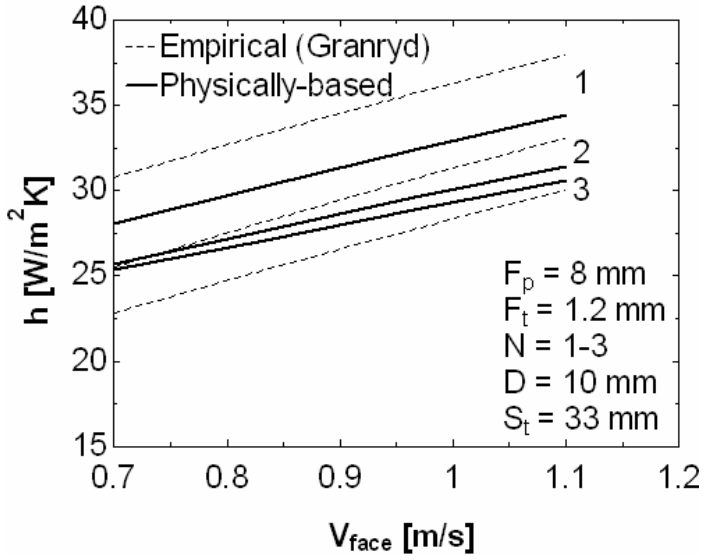

Figure 3.4 Comparison with Granryd (1965)

Due to the scarcity of published data, it is difficult to test many of the assumptions underlying the semi-empirical correlation presented in this paper. Therefore more detailed comparisons with available data are currently underway, aimed at confirming, refining or substantially revising the assumptions described here. For example the semi-empirical approach presented here deals with developing flow effects (thinner boundary layers near the leading edge) by applying the enhancement factors to local heat transfer coefficients on the fins. In combination with the assumption that the horseshoe vortices are concentrated in the local area immediately downstream of the tube, this may overestimate the enhancement effect. Although computationally more complex, it may be more accurate to assume that the streamwise vortex cores, instead of being pinched into a triangular region immediately downstream of tube row i due to the presence of tubes in staggered row i + 1, actually diverge far enough to travel around the

sides of the tubes in row i + 2, where their enhancement effects would be diffused over the [smaller] local heat transfer coefficients farther downstream. These and other assumptions are difficult to evaluate, especially when we are forced to use empirical correlations as a surrogate for the underlying data. Some of those correlations, such as Granryd's (1965), are derived from data sets that included both inline and staggered tubes, thus making it impossible to test physical assumptions about the downstream path of streamwise vortices.

Other assumptions may underestimate the enhancement effects. For example the enhancement factor reported by Ichimiya et al. (1988) was obtained by placing an acrylic cylinder on top of a heated metal plate and measuring local temperature profiles. Since the insulating effect of the cylinder would have produced immeasurable variations in local heat flux, it may have caused the heat transfer coefficients calculated using local surface temperatures would represent a lower bound.

Recall from Figure 3.2 that the enhanced area extended in a transverse direction about 0.35 tube diameters. Thus for heat exchangers having tube pitch less than 1.7 diameters, the enhanced areas may overlap laterally and invalidate the superposition model employed here.

At the current stage of development the semi-empirical correlation presented here is useful for exploring design tradeoffs in heat exchangers having large tube and fin pitch, as in many refrigeration applications where it is necessary to accommodate substantial frost accumulation, and defrost frequency may be constrained by marketing considerations. It may also apply to stationary applications where face area is constrained to the point where a deeper heat exchanger is needed to provide sufficient heat transfer area. In such cases, tube and fin pitch must be increased in order to minimize pressure drop, and thicker fins may be employed to offset the larger tube pitch.

The model's greatest value, after further validation, may be realized by using it to modify the form of the purely empirical expressions now used to predict air side performance of heat exchangers having smaller fin and tube pitches. By providing physically realistic asymptotes for such heat exchangers, and physically-based ways of dealing with the blockage effect of fin thickness near the leading edge and some developing flow effects, this semi-empirical approach may lead to development of a single expression that could extend throughout the parameter space. In particular, as more becomes known about the effect of fin pitch on the ability of von Karman vortex streets to form, and the rates at which both spanwise and streamwise vortices are dissipated, it may be possible to make the expressions more broadly applicable and even more physically realistic.

3.4.2 Semi-empirical pressure drop model

The pressure drop model is based generally on the same fluid mechanics described by the enhanced wake model described above. It is simply a superposition of fin array and tube bank pressure drops, based on face velocity up to the first row and maximum velocity everywhere downstream. The tube pressure drop was taken from Zukauskas and Ambrazyavichyus (1972), the fin pressure drop from Shah and London (1978), and the entry and exit losses from White (1999). Since the model ignores the dissipation of energy used to generate the streamwise vortices generated by the tubes, it underestimates pressure drop compared to Wang et al. (2000) within the latter's empirical bounds: up to 55% for 1 row heat exchangers, and up to 50% lower for more than two rows as shown below in Figure 3.5. The vertical lines on this figure show Wang et al.'s (2000) correlation bounds. The percent difference is smallest at small fin pitch, apparently because the vortices have little room to form. It is greatest at Wang et al.'s (2000) upper bound (fin pitch = 3.2 mm), apparently because stronger vortices are formed and subsequently dissipated via their heat transfer-enhancing interactions with the fins. The underestimation of pressure drop also tends to be greatest at small tube pitches where the horseshoe vortices formed by adjacent tubes overlap.

At larger fin and tube pitch the vortices are less confined and their interactions less intense, so the superposition assumption tends to be more accurate. However, the energy required to generate the horseshoe vortices at the fin-tube junctions is still neglected, so further improvements to the pressure drop model remain to be developed. See Appendix A for more on enhanced wake heat transfer and pressure drop accuracy.

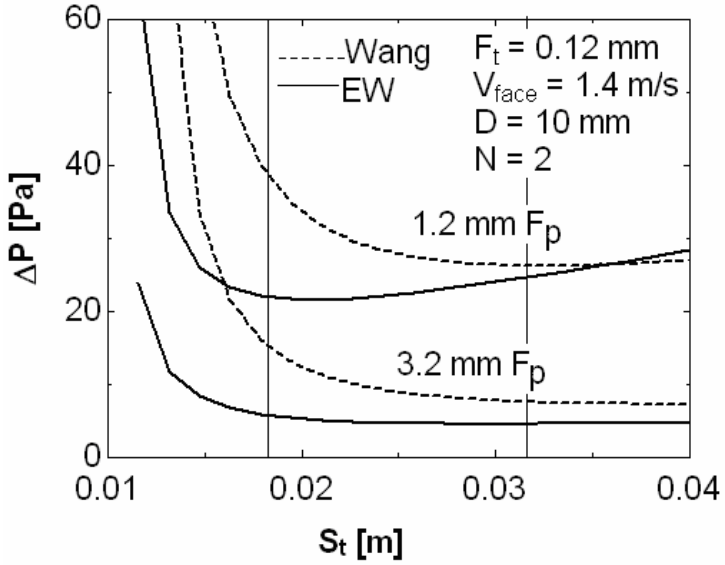

Figure 3.5 Pressure drop predicted by Wang et al. (2000) and the enhanced wake correlation.

3.5 Round tube condenser optimization

A computational experiment was conducted using an air conditioner simulation model. The goal was to find the condenser configuration which results in the minimum system power consumption for a given condenser mass. A five degree-of-freedom search was performed for plain, louvered, and slit fins using different empirical heat transfer and pressure drop correlations by Wang et al. (2000). Empirical correlations are necessarily limited to a small empirically defined subset of the parameter space. In order to explore outside that parameter space, the semi-empirical model, which accounts for the wakes generated by the tubes, was used for heat transfer and pressure drop.

3.5.1 System model

Despite the tentative nature of the semi-empirical heat transfer and pressure drop models described above, they were used to explore potentially optimal designs in the parameter space outside Wang et al.'s (2000). The five search variables were: condenser face velocity, number of tube rows, transverse tube pitch, fin pitch, and fin thickness. The longitudinal tube pitch was constrained so that the tube layout was always of an equilateral triangle shape. Tube outer diameter always moved to its lower bound, which was constrained to 7 mm for reasons of cost. Several other geometric and operating variables were held constant for the analysis; these appear in Table 3.2. The condenser was represented by a detailed finite-volume model, which was embedded in a simpler thermodynamic state model for the rest of the cycle. Circuiting was adjusted to limit saturation temperature drop in the condenser, and face area was fixed because it would otherwise increase without bound.

Table 3.2 Equality constraints and operating conditions

A_{face} [m^2]	1
D [mm]	7
ΔT_{sat} [C]	1
Q [kW]	10.5
Superheat [C]	5
Subcooling [C]	5
$T_{outdoor}$ [C]	35
T_{evap} [C]	12
$\dot{W}_{evap}$ [kW]	0.4
η_{fan}	0.1
η_{comp}	0.7

3.5.2 Results using empirical correlations

The optimal condenser configurations corresponding to the three empirical correlations are discussed first. They illustrate the geometric adaptations that can be exploited to offset the higher friction factors associated with slit and louvered fins. Interestingly, the 1-row plain fin heat exchanger with its relatively low friction factor and high heat transfer coefficient responds by operating at a higher face velocity where the larger heat sink helps reduce condensing temperature.

Each point in Figure 3.6 corresponds to a new tube row added to the condenser. The optimization was constrained in at least one variable by the limits of the empirical correlations for every point except the two row plain fin condenser. This indicates that the real optimum probably lies below the points shown.

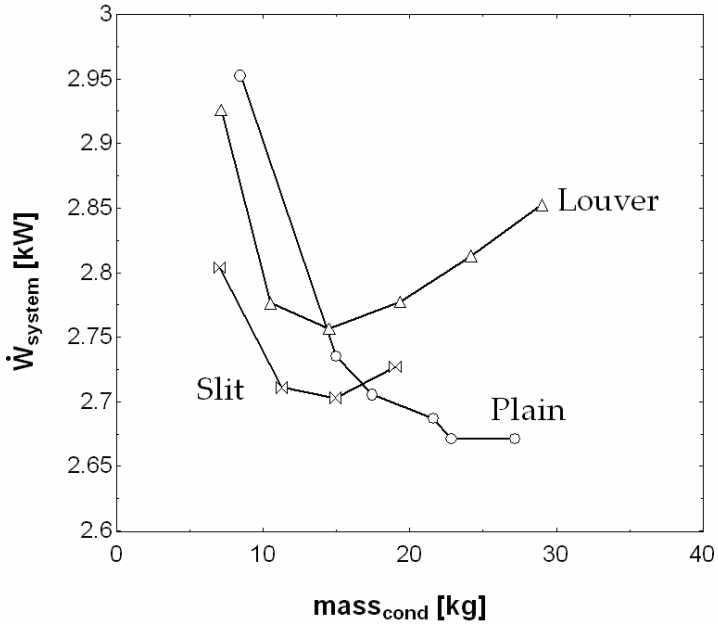

Figure 3.6 Optimal configuration performance for varying mass and number of rows.

For the case of two or more tube rows, both slit and louvered fins have the tube pitch and fin pitch move quickly to their upper bounds. At that point the only way to decrease condensing temperature (compressor power) is to increase the number of tube rows (depth), which increases fan power, causing the curves to turn upwards as air-

side pressure drop is increased by adding more surface area. Slit fins show the best performance for one to three tube rows. For four to six tube rows plain fins show the best performance because slit and louvered fins show an increase in required power when moving from 3 to 4 rows. This is depicted in Figure 3.6. Care must be taken when interpreting these results because the empirical parameter space is not uniformly accurate. In the case of slit fins, the lower limit on tube outer diameter (7.1 mm) was slightly above the 7 mm equality constraint.

In heat exchangers with a one-row core, slit fins use the least system power and require the least amount material. This is due to their high airside heat transfer coefficient (70% higher than plain) and low pressure drop (31% lower than louvered). Louvered fins require slightly more mass because their optimal fins are 8% thicker to maintain high fin efficiency (89%) under higher heat transfer conditions. Plain fins use material almost as efficiently as louvered because their lower pressure drop offsets their higher heat transfer resistance. Fin pitch is at its lower bound in all three cases, to maximize heat transfer coefficient in such a shallow core. Both slit and louvered fin correlations are limited to 25.4 mm maximum tube pitch. The slit fin condenser reaches this upper bound in an attempt to increase total heat transfer surface area as core depth increases proportionately, but the louvered fin does not, apparently due to the loss of fin efficiency and higher pressure drop. The parameter space for plain fins allows for a maximum of 32 mm tube pitch, but that bound is not reached for one-row cores.

At two and more rows, the increased pressure drop is accommodated in all cases by increasing fin and tube pitch, until they reach their upper limits. Once those limits are reached, adding heat transfer surface by adding more mass quickly begins to increase fan power more than compressor power is reduced. Fin thickness shows a slight trend of increasing with tube pitch in order to maintain fin efficiency. The plain fin correlations are less constrained. The upper bound on tube pitch is reached at 3 rows and the upper limit on fin pitch (3.2 mm) is reached at six rows deep.

3.5.3 Results using enhanced wake correlation

The same general trends are evident when the semi-empirical model was used to simulate the condenser outside the parameter space covered by the empirical correlations for plain fins. It was necessary to impose an arbitrary lower bound on fin pitch because the optimization sought to minimize it. This was expected because the semi-empirical correlation neglected the pressure drop caused by forming the root vortices at the fin-tube junctions, and the stagnant wake that forms behind the tubes when fin pitch becomes small. Both of these effects were captured by Wang et al.'s (2000) empirical correlation, which is valid only for fin pitches less than or equal to 3.2 mm. The stagnant wake begins to fill in as fin pitch is increased from 1.2 to 2 mm; this is characterized by an increasing heat transfer coefficient as shown in Figure 3.7 (See Appendix C for details). The reversal in heat transfer coefficient after 2 mm fin pitch occurs the thickening of the boundary layers decreases heat transfer faster than filling in the stagnant wake increases it. As fin spacing increases, the stagnant wake disappears completely. This appears to occur just above Wang et al.'s (2000) upper limit, where the empirical and semi-empirical lines would meet. Of course more data are needed to confirm this speculation.

Granryd (1964) developed correlations for fin pitches greater than or equal to 4.2 mm by first superimposing results for tube banks and fin arrays and estimating empirical correction factors based on data for a set of 1- to 3-row coils having larger fin and tube pitches and large fin thickness.

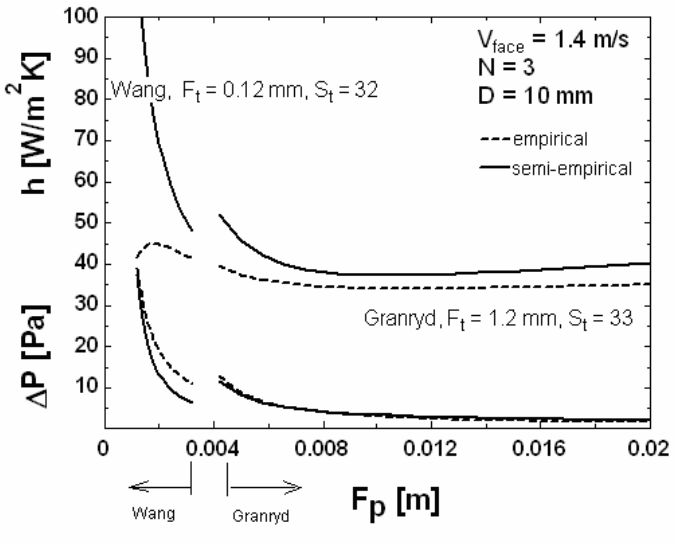

Figure 3.7 Comparison of enhanced wake and empirical correlations within empirical parameter spaces.

Figure 3.7 also compares our semi-empirical correlation to that of Granryd's (1965) for 10 mm tubes and 3.3 mm fin spacing, where his data set was fairly dense. Again, satisfactory agreement is obtained as both correlations approach known physical limits as fin pitch increases. On the other hand extrapolations of Wang et al.'s (2000) correlation to large fin and tube pitches revealed unrealistic behavior as it diverged from known physical limits, especially in the case of heat transfer. The 3-row coil was selected for this example because the limits of the two empirical correlations nearly overlap in this region. Together, the two comparisons provide some support for extending our semi-empirical correlation to fin pitches as small as 3 to 4 mm.

Care must be taken when comparing the curves for Wang et al. (2000) and Granryd's (1965) geometries in Figure 3.7. The gap between the two curves around 4 mm fin pitch is due to the 1 mm difference in fin thickness in Granryd's (1965) and Wang et al.'s (2000) experiments. The curves could actually overlap if fin spacing were plotted on the x-axis. Fin spacing is the distance between the fins (not counting fin thickness) and is the parameter used in the calculation of hydraulic diameter.

Figure 3.8 shows the results obtained for 2 and 3 tube rows, with fin pitch constrained to a lower bound of 3.3 mm. Note the negligible benefit obtainable by adding a third tube row while fin pitch is constrained. For a given mass of material the 2-row coil deploys it more efficiently through reliance larger tube pitch and fin thickness to achieve a higher fin efficiency and more heat transfer area per tube, while the smaller core depth reduces friction factor to allow a higher face velocity and correspondingly larger heat sink. The results suggest that improved performance may be achieved at a smaller fin pitch outside the range of this semi-empirical correlation.

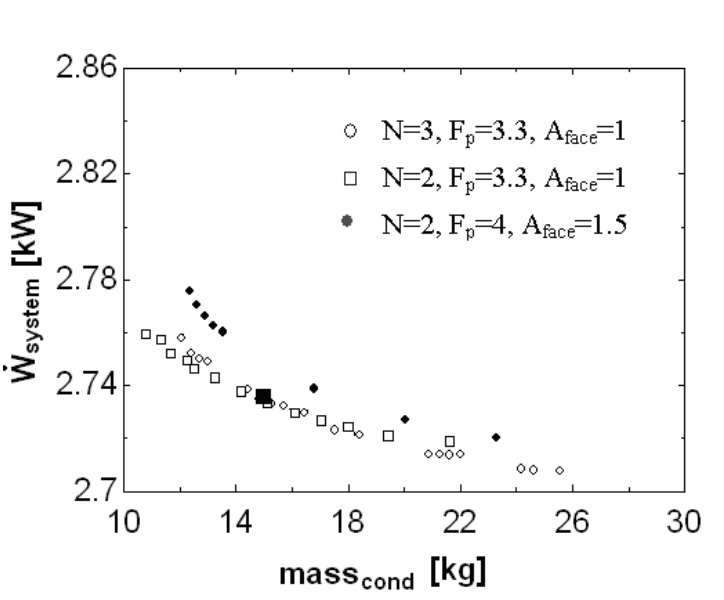

Figure 3.8 Minimizing system work using enhanced wake correlation

The optimization was repeated with a lower limit of 4 mm on fin pitch, where Granryd's (1965) results can be accepted as confirming evidence. This constraint severely limited the heat transfer surface area attainable with 1 m^2 face area, increasing system power by ~11%. The benefit of using larger fin pitch is that when the condenser is operated as in evaporator in heat pump mode, there will be less frequent defrost cycles. Subsequent analysis shown in Figure 3.8 demonstrated that the performance deficit could almost be eliminated by relaxing the face area constraint.

Finally the large solid square symbol shown Figure 3.8 represents the performance of the 1 m^2 two-row 15 kg core yielded by Wang et al.'s (2000) empirical correlation. The semi-empirical correlation found an equally efficient configuration at nearly twice the fin pitch by increasing tube pitch beyond Wang et al.'s (2000) 32 mm limit, suggesting a possible economic advantage. The semi-empirical result shows more fin mass and less tube mass than the empirical correlation. Fins are made of less expensive material, resulting in a possible lower initial cost with equal performance of the optimal configuration found using the empirical correlation. Other similar economic tradeoffs are discussed below in section 8. The semi-empirical correlation allowed fin pitch to almost double to 3.3 mm, allowing face velocity to increase from 1.4 to 1.9 m/s and provide a larger heat sink.

3.6 Round Tube Heat Exchangers Sensitivity To Constraints

Some of the equality constraints imposed on the condenser optimization are now examined to observe how system performance responds to increases in face area and fan/motor efficiency, and a decrease in fin conductivity. Wang et al.'s (2000) empirical correlation was used to search within his constrained parameter space; then the semi-empirical model was used to minimize system power at larger fin and tube pitches. The base case is a two-row 15 kg condenser with the equality constraints shown in Table 3.2. Table 3.9 shows a summary of all the sensitivity results for both correlations (See Appendix B for details).

3.6.1 Wang et al. correlation

When face area is increased from 1 to 1.5 m^2, the performance is improved significantly. The system power is decreased 6%, from 2.7 to 2.5 kW, due to the larger heat sink provided by a 31% higher airflow rate. System power also decreases 7% (from 2.7 to 2.5 kW) when the condenser fan efficiency is increased from 10 to 30%, allowing the 15 kg of condenser core mass to be reconfigured. The design variables all change from the base case in order to take advantage of the increased fan efficiency. The base case analysis used the thermal conductivity of pure aluminum is 237 W/mK, which is only slightly higher than that of the fin materials actually used. To quantify sensitivity to this assumption, an extremely conservative assumption of 160 was tested, representing the stronger alloys sometime used in brazed heat exchangers where more strength is required. Using the stronger fin alloy was found increase optimal system work only 1%. The 15 kg of condenser mass is reconfigured to keep fin efficiency high. When condenser mass is reduced to 10 kg instead of 15 kg, the Wang et al. (2000) correlations predict that system power increases by almost 2.6%. The 5 kg of mass was taken from fins, where pitch increased from 1.7 to 2.3 mm.

3.6.2 Enhanced wake model

Sensitivity analyses were also conducted on the semi-empirical model to determine the response of heat exchangers having larger fin pitch. The enhanced wake correlation shows a nearly 10% reduction in system power when face area is increased from 1 to 1.5 m^2. The airflow rate increases 21% from the base case, resulting in a larger heat sink with 19% lower face velocity,. Increasing fan efficiency to 30% lowers system power by almost 7%. The airflow rate increases 50% from the base case, providing a larger heat sink and higher heat transfer coefficient. About 10% of the 15 kg of metal moves from tube pitch to fin thickness in order to keep fin efficiency high at 89% (1.5% higher than the base case). Using a stronger fin alloy with a thermal conductivity of 160 W/mK increases system power only 1.3%. About 15% of the metal is again shifted from tube pitch to fin thickness to keep fin efficiency high at 88%, but the airside area is lowered 15% as a result of this. When condenser mass is reduced to 10 kg instead of 15 kg, system power increases by 1.6%. This is due to 30% thinner fins and smaller depth due to 15% smaller tube pitch. All optimal configurations appear in Table 3.3 below.

3.6.3 Sensitivity of constraints summary

Table 3.3 Summary of optimal system sensitivity to constraints.

	Enhanced Wake Correlations						Wang et al. (2000) Correlations					
	W_{sys}	S_t	F_t	depth	V_{face}	F_p	W_{sys}	S_t	F_t	depth	V_{face}	F_p
base case	3.05	41	0.27	71	2.4	4*	2.73	32*	0.15	55	1.5	1.7
A_{face}= 1.5	2.76	36	0.18	62	1.9	4*	2.57	32*	0.12*	55	1.3	2.4
η_{fan} = 0.3	2.85	37	0.30	64	3.6	4*	2.55	30	0.13	52	1.8	1.5
k_{fin} = 160	3.09	35	0.31	61	2.5	4*	2.76	32*	0.16	55	4	1.9
m = 10	3.10	33	0.19	57	2.6	4*	2.80	32*	0.12*	55	1.6	2.3

* indicates search variable was constrained to a correlation limit

3.7 Multilayer Round Tube Heat Exchangers

The difference between a multilayer heat exchanger and a multirow heat exchanger is that in the former the boundary layer restarts for every heat exchanger layer, which increases the both heat transfer coefficient and pressure drop. Repeating the optimization analyses using both the enhanced wake and Wang et al. (2000) correlations indicated that multilayer condensers achieved worse performance than single layer. This is because the pressure drop penalty outweighs the heat transfer benefit. Even when the condenser fan/motor efficiency is increased to 30%, the two layer coil increases system power ~6% greater than the single layer, using the Wang et al. (2000) correlations.

The enhanced wake correlation can be applied to multilayer plain fin round tube heat exchangers. The enhancement factor and enhanced area are modified so that the X/D extends only from the rear of the tube to the exit plane of the layer, but the multirow heat transfer enhancement effects predicted by Zukauskas and Ambrazyavichyus (1972) were included. The air velocity was modeled just as the multirow case, with face velocity up to the midpoint of the first tube and maximum velocity everywhere downstream. Pressure drop was computed as a superposition of fins and tubes with the same air velocities as the heat transfer. Comparisons with Granryd's (1965) results for multilayer heat exchangers confirms the accuracy of the enhanced wake correlation with maximum differences of 16% for heat transfer coefficient and 29% for pressure drop for the two layer case. When a two-layer-two-row condenser is optimized using the enhanced wake correlation, it attempts to enter Wang et al.'s (2000) parameter space (smaller fin and tube pitch). The reliability of the enhanced wake correlation at small tube pitch is also unconfirmed, so a lower bound of 30 mm was placed on tube pitch. With fin and tube pitch at their lower bounds (4 mm and 30 mm), the system power was found to increase 6.6% as a result of boundary-layer restarting. However the optimal multilayer condenser required 1.7 kg less mass than the base case of 15 kg.

Since optimization using the semi-empirical model suggested that the real optimum lies inside Wang et al.'s (2000) parameter space, this correlation was applied to multilayer by using the heat transfer coefficient of a one row condenser of the same configuration. Pressure drop was equal to the pressure drop of one layer multiplied by the number of layers. For the two-layer case, the fin and tube pitch attained intermediate values of 1.6 and 28 respectively, only fin thickness was constrained at its lower bound of 0.12. Because the fin and tube pitch have the largest effect on performance, the optimal configuration found is very near the true optimum. The results show that moving to two layers hurts performance. System work increases 8.4% and mass decreases 15% compared to the base case using Wang et al.'s (2000) correlations.

3.8 Round Tube Heat Exchanger Economic Tradeoffs

Many of the more efficient split systems in use today (10.5 kW cooling capacity) have condensers in the 10-15 kg range. The following analysis compares the optimal (minimum system power) designs identified using the enhanced wake model at an admittedly large 4 mm fin pitch, where the semi-empirical correlations are expected to accurately reflect the physical tradeoffs involved. Moving from a 2-row 15 kg condenser to 10 kg saves 5.6 kg of fin material but adds 0.6 kg of tube material. Tube mass increases because the 1 m^2 face area constraint and smaller tube pitch require increased tube length. The cost difference was estimated assuming copper tubes cost \$7/kg and aluminum fins \$4/kg, yielding a material savings of \$18.20. The optimal 10 kg condenser requires 48 W more system power; which at \$0.10/kWh and 1000 hours of operation per year translates to \$4.80 increased operating cost per year. Increasing condenser mass from 10 to 15 kg will result in a payback period of 3.8 years for the added material. Payback would be much shorter in warmer climates and at higher copper prices.

The above result may seem counterintuitive: reducing total mass requires that an increased mass be devoted to tubes in order to maximize system efficiency, thus partially offsetting the expected cost reduction. Since copper tube material is more costly and denser than aluminum fin material, trading tube mass for fins will yield more material volume (used for more airside area or fin thickness) and lower cost. The following example illustrates how increasing tube pitch can reduce heat exchanger cost at the expense of some increase in system power.

If the base case optimal tube pitch is increased 10% from 41 to 45 mm while keeping mass at 15 kg. Increasing tube pitch simultaneously increases core depth, so the optimal fin thickness is reduced 8% and fin pitch stays at its lower bound of 4 mm. System power increases 2 W because this configuration is no longer the power-minimizing 15 kg configuration. This move to 1.5% more fin mass and 9% less tube mass reduces condenser cost by 1% ($0.73) compared to the base case. The cost of the 2 W increase in system power is $0.20 per year. This change in condenser configuration results in a 3.6 year payback and may therefore be cost-effective under most conditions. Note that such large tube pitches lie far outside the range of empirical correlations, reflecting the fact that copper and aluminum cost differentials have historically been much smaller.

Chapter 4. Material and Manufacturing Constraints

To provide context and constraints for the more detailed analyses of flat- and round-tube heat exchangers in Chapters 2 and 3, it is necessary to identify important material-related constraints and tradeoffs. This chapter therefore begins by exploring some simple geometric tradeoffs that illustrate key thermal-hydraulic characteristics of flat and round tubes. Subsequent sections describe in more detail the material properties that may constrain the design of some types of flat- and round-tube heat exchangers, and identify pathways to new designs.

4.1 Some geometric relationships

To better understand the ways in which flat multiport tubes differ from the more familiar round tubes, the following paragraphs present some simplified comparisons of the two types of tubes, expressed in terms of heat transfer surface area and tube mass.

It is approximately true that a heat exchanger having a given capacity will require about the same refrigerant-side cross-sectional flow area, whether flat or round tubes are used. The thin dotted line in Figure 4.1 illustrates the dramatic increase in heat transfer surface area that results from using smaller diameter tubes or ports. On the refrigerant side the heat transfer surface area per unit flow area is the same for round and flat tubes (and circular or square ports) because the hydraulic diameters are equal. The amount of surface area inside a flat multiport of given outside dimensions is greatest for triangular ports, and slightly less for square and round ports in that order. In all three cases the refrigerant-side area is large enough to reduce refrigerant-to-wall ΔT to a few tenths of a degree Celsius.

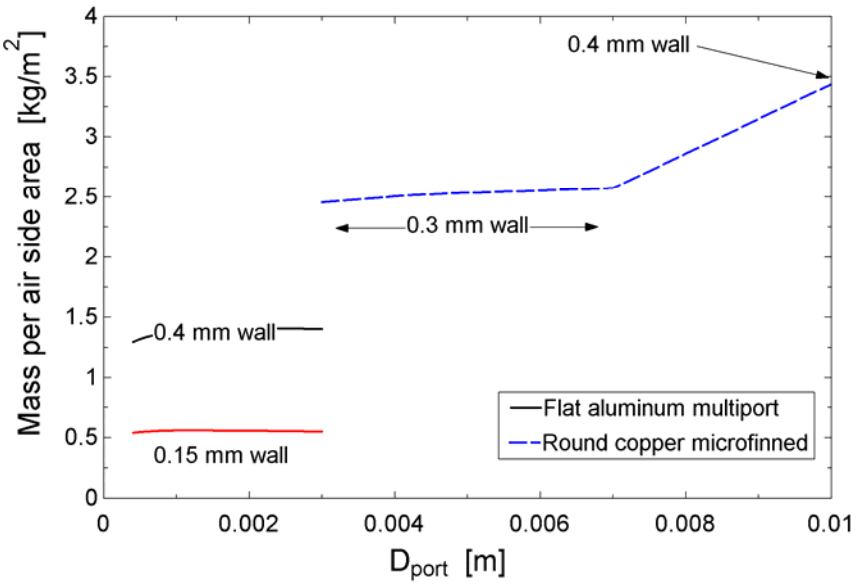

Figure 4.1. Heat transfer surface areas for flat and round tubes

Traditionally tubes have been selected to provide the required flow area and refrigerant-side heat transfer area. However in the case of flat multiport tubes their contribution to the heat exchanger's air-side area is also significant. As expected for conventional round copper tubes the thick solid line follows the curve for refrigerant-side area, because the two differ only due to the outer/inner diameter ratio. The thick solid line shows for flat tubes that the ratio is somewhat lower because the webs separating the ports are not in contact with the air. Nevertheless

the Figure illustrates the magnitude of the substantial air-side heat transfer benefits obtainable by using flat multiport tubes.[1]

The trends shown in Figure 4.1 depend mainly on tube geometry; tube wall thickness has a negligible influence. The discontinuity reflects the fact the round tubes' entire outer surface is in contact with the air, while the webs inside the multiport tube are not. The calculations also neglect the contribution of microfins inside round copper tubes, which can increase heat transfer area by about 60%.

Since mass can be a useful surrogate for cost, Figure 4.2 is presented to illustrate the effect of the factor of 3.3 density difference between aluminum and copper. The mass of copper needed for round tubes is shown by the dashed line, assuming that burst pressure limits require wall thickness to increase from 0.3 to 0.4 mm as diameter increases from 7 to 10 mm. For smaller diameters the tube wall thickness is held constant, reflecting the need to retain sufficient strength to resist buckling when the mandrel is inserted to mechanically expand the tubes after the fins are installed. If burst pressure were the only constraint, the 7-10 mm line could be extrapolated to lower diameters.

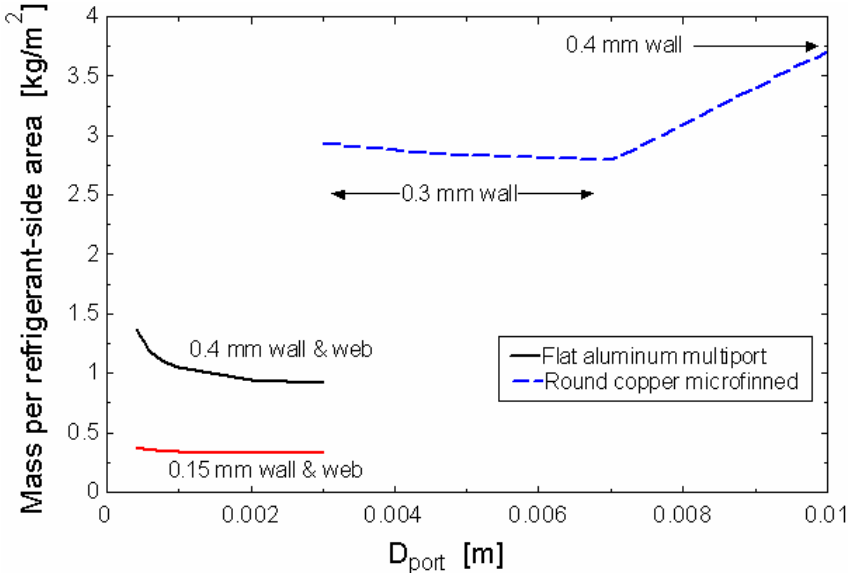

Figure 4.2. Mass required per refrigerant-side area

For flat multiport extruded aluminum tubes Figure 4.2 reflects the lower density of aluminum, as well as the range of wall and web thicknesses typically encountered. Thicknesses of 0.4 mm are common today for tubes with port diameters on the order of 1 mm, but some manufacturers are advertising thicknesses as low as 0.15 mm.[2] A variety of considerations to be discussed later (e.g. burst pressure, ease of extrusion, whether work-hardened or annealed) will influence the choice. In any event it is clear that the flat tubes can be considerably lighter, for a given refrigerant-side heat transfer area requirement.

Figure 4.3 shows the same general trends for the air-side area of the tubes' outer surfaces. Of course in the past, the contribution of tubes to air-side heat transfer surface has been quite small, except perhaps in the case of refrigeration coils having very large fin pitch. However it is clear from Figures 4.1 and 4.3 that flat multiport tubes can make non-negligible contributions to air side heat transfer area, so it is useful to compare the values in Figure

[1] This is in addition to the benefit of lower air-side pressure drop owing to the streamlined tube profile.
[2] http://www.brazeway.com/extrusion/specs/MMP_specifications.pdf

4.3 to the corresponding value for aluminum fins (~0.1 mm thick) – they require less than 0.1 kg of aluminum per square meter of heat transfer surface.[3] Therefore even the thinnest flat multiport tubes could not compete on the air side with secondary surfaces, in terms of material utilization efficiency.

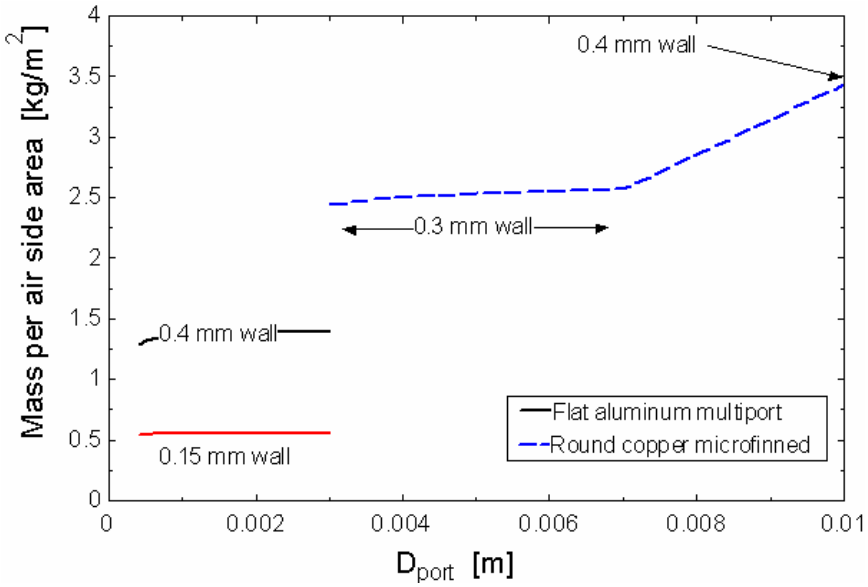

Figure 4.3. Air-side area provided by tubes and fins

Historically the cost of copper (mass basis) has been similar to that of aluminum. In recent years, however, the difference has increased to a factor of 3. Therefore the flat vs. round tube comparisons in Figures 4.2 and 4.3 imply that heat transfer surface area provided by the copper in traditional round tubes costs almost a factor of 5 to 10 more than the aluminum needed to provide an equivalent amount of air-side surface area using flat multiport designs. Of course adding manufacturing costs to the numerator and denominator reduces this ratio considerably, but the difference in material costs remains significant.

4.2 Some important material properties

Thermal conductivity is arguably the most important factor accounting for the widespread use of copper and aluminum in a/c and refrigeration applications. Compared to steel, the conductivity of aluminum is a factor of 3 greater, while copper's conductivity exceeds that of aluminum by another factor of 2 or more. However alloying elements and cold working can reduce conductivity, with the result that the conductivity of copper tubing used in a/c applications is about equal to that of conventional aluminum fin material and only ~35% greater than that of 3003 aluminum used for flat multiport tubes and fins (Copper Development Assn. 2006, The Aluminum Assn. 2000).

As with any single parameter it is important to recall the robustness of the multidimensional design tradeoffs revealed by the optimization analyses in Chapters 2 and 3. For example a ~20% degradation of fin conductivity due to cold working need not require a 20% in fin mass to maintain fin efficiency; the need for such an increase can be mitigated by moving to a different part of the parameter space, adjusting fin height, fin pitch, face velocity etc.

[3] Half of this advantage is comes from the fact that both sides of the fin are exposed to air, vs. one side of a tube. The remainder is attributable to the difference in thickness and the existence of webs.

Strength is important because of the material-saving advantages of minimizing fin and tube wall thicknesses. The ultimate tensile strength (UTS) of copper is at least three times greater than pure aluminum, but this ratio can be reduced to about a factor of 2 after the aluminum is work-hardened. More important for design purposes is the yield strength, which can be reduced far below the UTS by annealing to make the material ductile, or increased closer to the UTS to make it stronger but more brittle. Although these work-hardened properties are very important, comparisons can be misleading; for example the process of brazing aluminum heat exchangers can reduce yield strength by a factor of 4, as discussed below. Figure 4.4 shows how much yield strength of a particular alloy can be affected by temper (annealed vs. hardened). The two copper alloys shown are C10100 (nearly pure) and C19200 which contains some iron and is used for copper tubing in a/c systems.

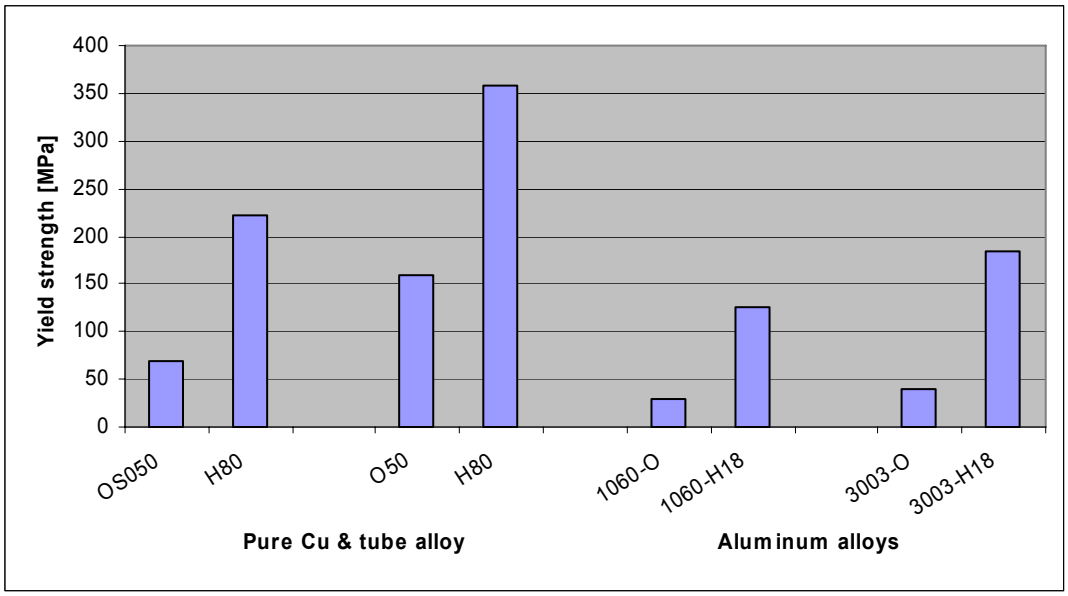

Figure 4.4 Effect of strain hardening on yield strength

Corrosion is always an issue with two dissimilar metals in the presence of an electrolyte such as salt water, creating a galvanic cell. In conventional heat exchangers the aluminum serves as the cathode, giving up electrons and eventually disintegrating. In aluminum heat exchangers made of dissimilar alloys care must be taken to ensure that the fins are sacrificial, to ensure that the tubes remain intact in order to prevent leaks. A sacrificial zinc coating is commonly applied to tubes as they exit the extrusion process, when the tubes are made of an alloy different from the fins.

Thermal expansion coefficients for aluminum are about 40% larger than those for copper, and relatively insensitive to alloying materials and temperature. It is essentially constant at the relatively low temperatures at which a/c heat exchangers operate. In absolute terms thermal expansion becomes significant only during brazing, when a heat exchanger core clamped in a fixture to protect against creep and sag – this can create stresses large enough to cause thin fins to buckle. In heat exchangers that do not require brazing, or in which fins are otherwise configured (e.g. by curvature) to resist buckling, thermal expansion properties may be less important.

4.3 Implications for heat exchanger design constraints

Fins. From a purely thermal-hydraulic standpoint, thinner is better. In round tube heat exchangers, the fins help provide adequate structural stiffness to the core. Optimal fin thicknesses are generally >0.1 mm for one- and

two-row heat exchangers and even thicker for deeper cores. The tradeoff between fin efficiency and fan power leads to the selection of these relatively thick fins because the high air side pressure drop created by round tubes favors large tube pitch. Moreover for louvered and slit fins, their higher heat transfer coefficients and interrupted conduction pathways may also require thicker fins

On the other hand in flat tube heat exchangers with louvered fins, air-side pressure drop considerations favor short fins and small tube pitch, as shown in Chapter 2. Therefore today's fins are often much thicker than high fin efficiency requires. For example if louvers are needed in order to resist buckling during brazing, the fins must be shorter to reduce fan power. If certain brazing- and strength-related constraints were relaxed, fins used in flat-tube heat exchangers might not require louvers and could be much taller and thinner.

Since fins typically account for >80% of the air-side area, the need for efficient material utilization would favor use of softer nearly-pure aluminum fin materials whose thermal conductivity is ~35% greater than harder alloys. This is indeed the case for conventional copper-aluminum heat exchangers, but manufacturing considerations dictate use of harder (3000-series) alloys for the serpentined louvered fins brazed between flat multiport tubes. Specifically, the manganese content of 3003 makes it harder and more brittle than softer 1000-series, thus easier to cut louvers and form serpentined fins. Recall also from Figure 4.4 that the manganese content of 3003 makes the fin remain stronger after annealing, making it more suitable for withstanding brazing-related stresses as described below.

The need for brazing imposes several constraints on fin design; stronger (manganese-containing) alloys such as 3003 are needed to resist sag and creep at temperatures near the melting point of the fin itself. Creep can also cause louvers to close during brazing. Fins are typically clad with alloy 4343, which contains silicon to reduce its melting point by ~50°C so it melts first and serves as filler material. The additional strength provided by 3003 also helps resist buckling of tall thin fins due to thermal stresses during brazing. Buckling resistance and stiffness are also increased by louvers, bumps or other surface features that increase the moment of inertia of the fin cross section. Serpentined plain or offset strip fins are very unstable and prone to collapsing during brazing. Therefore another approach might be to install the serpentine fins at an angle slightly off the perpendicular to the tubes (creating triangular- or parallelogram-shaped channels), while relying on other structural members to provide rigidity for the heat exchanger as a whole, both during and after brazing. Both approaches may be less prone to buckling or fin collapse, and therefore more compatible with the use of taller thinner fins.

Newer plate fin designs from Modine appear to avoid the buckling issues associated with serpentined fins, such as that shown in Figure 4.5 (upper left). Also shown are photos of individual plate fins that are slit and bent to fit between flat tubes, spanning the entire core. The design appears to be inherently easier to stabilize during brazing, which is still needed to ensure fin-tube contact. The fins are louvered, but there appears to be no reason that plain fins of the same design could not be made by a similar process, possibly avoiding the constraints on louver closure and fin collapse during brazing. Since the fins are already bent, buckling appears not to be an issue.

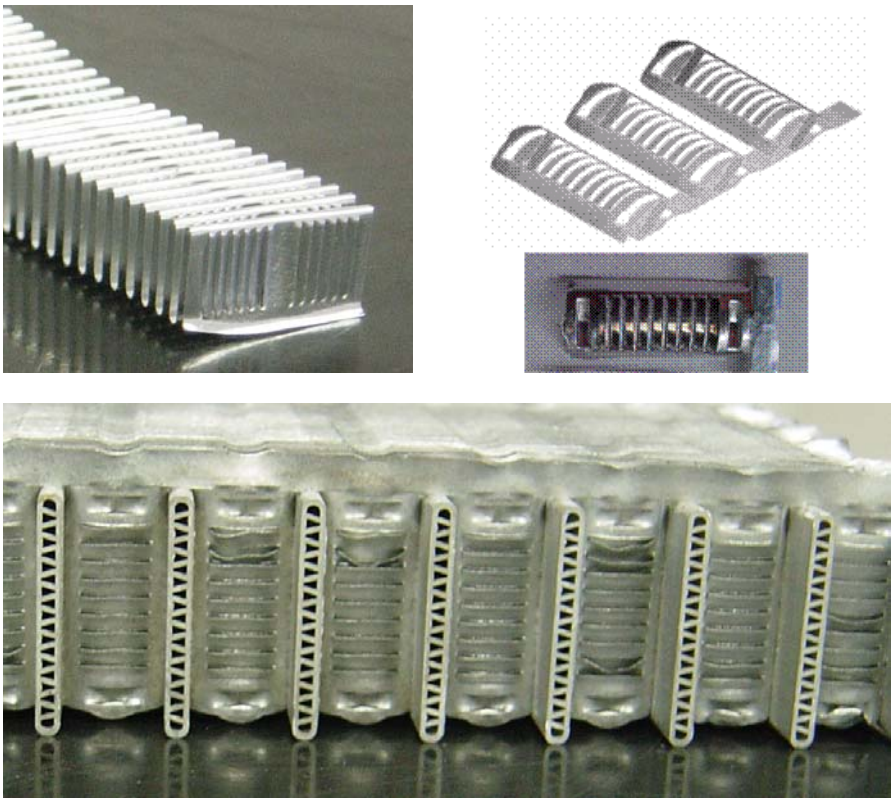

Figure 4.5. Serpentined and plate fins for flat tube heat exchangers

While serpentined fins provide a greater fin-tube contact area, the plate fins apparently provide enough (after brazing) despite their lack of collars. However if brazing is to be avoided (e.g. for reasons of strength and cost), other conceptual approaches exist. Some remain unproven or too costly, e.g. thermal adhesives; sliding slotted collared fins onto flat tubes; driving a tube through collared fin holes. The potential for research to reduce these costs is not well understood. Other approaches have well-known advantages and disadvantages, such as the spine fins used by GE for refrigerator evaporators and Trane for a/c condensers that apparently rely on larger fin-tube contact area to offset low or uneven contact pressure.

Tubes. Again from a purely thermal-hydraulic standpoint, smaller tube and port diameters are preferred because of lower burst pressure, increased heat transfer surface area, and lower air-side pressure drop. As diameters continue to be reduced, liquid refrigerant distribution becomes far more difficult in evaporators, where flash gas bypass places an upper bound on the cost of dealing with the problem. More research is needed to determine whether very small microchannel port diameters (<0.6 mm) will be vulnerable to refrigerant maldistribution as a result of oil deposition in the cold superheated areas of evaporator tubes. The following paragraphs explore the manufacturing and material-related constraints which are now limiting the pursuit of thinner tube walls and webs.

Burst pressure is the primary consideration affecting tube wall thicknesses, which of course must vary in direct proportion to tube diameter if burst pressure is held constant. Since multiport tubes share webs with the adjoining ports, webs must be twice as thick as the wall of a single circular tube having the same diameter. Since tubes of any material must withstand pressures at least 3x greater than maximum operating pressure (i.e. >12 MPa for R410A) yield strengths must exceed that value by a factor of $D/2t_{wall}$ or D/t_{web} for round and flat tubes, respectively. Therefore a 0.3 mm wall thickness on 9.5 mm copper tubing ($\sigma_y \sim 350$ MPa) can satisfy that

requirement. Similarly, strain-hardened aluminum tubes prior to brazing (σ_y ~ 120-160 MPa) can easily handle submillimeter port diameters. However after brazing even a relatively strong alloy like Al 3003 (σ_y ~ 40 MPa post-brazing) must have web thickness between a third and half the port diameter for the relatively high-pressure refrigerant R410A.[4] Flat aluminum multiport tubes having wall and web thicknesses ~0.4 mm are fairly common today, and from a post-brazing burst pressure point of view may support square ports up to ~1 mm diameter for R410A.

Thinner tube walls and webs hold promise for minimizing material costs; thicknesses ≤0.2 mm are now becoming available. However we could find no published data indicating the extent to which such thin walls would increase corrosion risk; i.e. would the current technology of spraying tubes with zinc as they emerge from extruder be sufficient? In the event that walls must remain thick (~0.4 mm) for corrosion resistance, very thin webs could still provide sufficient strength for correspondingly small ports (≤0.2 mm), but it is not clear whether the modest material savings would offset the tooling costs associated with making ports so small.[5] Finally there may be an additional limit imposed on wall or web thickness of some alloys, imposed by grain size or the scale of impurities (Beaudoin, 2006).

The extrusion process imposes other inherent constraints on tube design, especially on tube width (major diameter of flat multiport tube) exceeding ~100 mm. This is due to the difficulty of maintaining uniform temperature and pressure across the width of the die, preventing instabilities from exacerbating nonuniformities and causing the extrusion to veer off to one side. Another inherent disadvantage of extrusion is the tradeoff with the need for subsequent brazing, which requires use of such higher-strength and harder alloys as 3102 or 3003, which extrude slower than softer materials. Moreover the desire for thin-walled narrow multiport tubes also seems fundamentally incompatible with the size of currently available aluminum billets – another factor slowing the extrusion process and increasing its cost. It is not clear whether the refrigerant tubing market could grow large enough to motivate suppliers to provide smaller billets and correspondingly smaller extrusion equipment, or to devise ways of getting more tubes through a single die.

Copper tubes in conventional heat exchangers are strong enough to provide structural stiffness to the core and withstand mechanical expansion to contact fins made of relatively soft (1000-series) aluminum. In refrigerator evaporators that operate with R134a at relatively low pressure, thin-walled tubes are pneumatically expanded to contact the fins, and remaining contact resistance is quickly diminished by frosting as the system cycles on.

Finally in applications where the tubes must operate at temperatures >175°C (e.g. charge air coolers; gas coolers in transcritical R744 systems) other constraints come into play. For example creep can become significant at absolute temperatures around half the melting point), so walls and webs must be thicker to offset the loss of yield strength at higher temperatures.

4.4 Material choice

Of course it is possible to make both fins and [flat or round] tubes out of either copper or aluminum. It is primarily a cost issue because the conductivity of both materials is high. Traditionally the material cost has dominated the marginal manufacturing cost of increasing heat exchanger size. However the advent of brazed

[4] These figures are approximate, meant only to provide an overview. Actual limits depend on meeting fatigue life specifications, and actual operating conditions. Yield strength also decreases with operating temperature (~20% reduction at 50-70°C).

[5] Die deflection tolerances must be tighter; thin steel tools must be strong and wear-resistant at T~500°C

aluminum heat exchangers has forced reconsideration of that tradeoff. New manufacturing techniques (e.g. for making welded flat copper tubes with tiny channels; or for using thermal adhesives or pneumatic expansion to fasten fins to a single flat or round tube before assembly) call for a more general reassessment of "optimal" heat exchanger configurations. The choice between conceptually different designs (e.g. brazed or not; round or flat tubes) is strongly dependent on such manufacturing-related costs as setup, assembly and brazing. However optimization within a particular concept (e.g. round tube plate fin) is dominated by cost tradeoffs at the margin. The incremental cost of increasing heat transfer area is dominated by material costs, while setup and assembly costs tend to be less scale-dependent. Therefore the optimization analyses in Chapters 2 and 3 focused on quantifying those mass vs. performance tradeoffs in physical terms within realistic physical constraints suggested by member companies, recognizing that accurate cost data will always remain proprietary.

4.5 Refrigerant distribution

For both round and flat tubes, performance was optimized by minimizing diameters of round tubes or microchannel ports, which of course increases the number of parallel circuits. Refrigerant flow distribution is an extremely challenging fluid mechanics problem that must be solved separately.[6] For that reason the number of circuits was not constrained in our analysis, in order to explore configurations that were optimal from the standpoint of air-side heat transfer and pressure drop, and to identify the number of circuits that might be required.

In the case of conventional round tube-plate fin heat exchangers, the number of parallel circuits increases dramatically as tube diameters are decreased to 7 mm or less. Conventional conical distributors are limited in the number of circuits they can feed. Headers must serve as distributors in heat exchangers using flat multiport tubes, because the extremely large number of parallel circuits (measured either in number of tubes or number of ports) that must be fed. Virtually all microchannel heat exchangers have cylindrical headers that were originally developed for condensers, where the task is to evenly distribute high-void-fraction vapor. For evaporators where the task is to evenly distribute the liquid fraction (~10% by volume or less), radically different designs will probably be needed. One possible alternative scheme from Kulkarni and Bullard (2003) is shown in Figure 4.6; the idea is to shorten the flow length inside the header to minimize the opportunity for liquid/vapor stratification. The design eliminates the need for intermediate headers, and the optimal tube (circuit) length Note that all tubes are the same length, and it was found that the optimal tube length for R410A is approximately 1 m for a port diameter ~0.5 mm and is roughly proportional to port diameter. However it is not clear whether tubes serpentined in this manner may require additional support (e.g. a frame brazed to the U-bends) to meet core stiffness requirements. That same report also quantifies the upper bound on maldistribution losses in microchannel evaporators.

[6] Some possible solutions may have a cost that is independent of the number of circuits, e.g. separating vapor immediately downstream of the expansion device, and bypassing it around the evaporator.

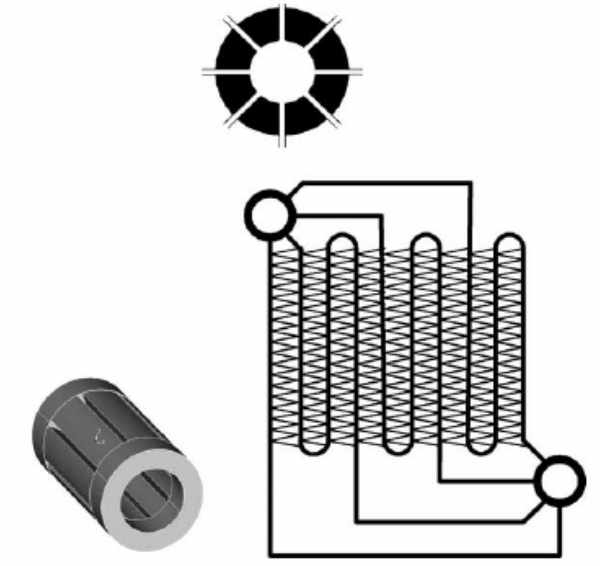

Figure 4.6. An alternative to long cylindrical headers

Simple geometric considerations dictate that conventional long cylindrical headers must have an internal diameter greater than the major dimension of a flat multiport tube. Large-diameter headers require thicker walls, thereby increasing heat exchanger mass and cost, especially in the case of high-pressure refrigerants. This leads to microchannel heat exchanger designs having many narrow tubes instead of fewer wide ones, increasing the probability that one of the tube-header junctions will leak after brazing. Avoiding this dilemma may therefore require abandoning the conventional cylindrical header design.

Large-diameter headers have hydraulic disadvantages as well, because mass flux in the header decreases faster than the mass flux entering (from wider tubes). This increases stratification of the two-phase flow inside the header, exacerbating maldistribution. Moreover long flow lengths provide greater opportunities for stratification to develop, and taller fins (beneficial from a heat transfer standpoint) necessarily increase the flow length of traditional long cylindrical headers. A variation on Figure 4.6 might offer an opportunity to eliminate these problems by bringing together all the unfinned tube lengths, essentially stacking them together and inserting them into a thick-walled rectangular header. This would eliminate constraints on tube major diameter, and greatly diminish the potential for liquid/vapor stratification and resultant maldistribution.

Chapter 5. Conclusions

Purely thermal-hydraulic considerations tend to call for tubes that have very small diameters and thin walls, fins that are very thin and have offset strips instead of louvers, and infinitesimally thin heat exchangers with infinitely large face areas and infinitesimally small face velocity. While simple packaging constraints rule out such a core geometry, and material and manufacturing considerations constrain fin, tube and header designs.

The constraints imposed on the performance optimization analyses of both flat- and round-tube heat exchangers in Chapters 2 and 3, respectively, and summarized in Table 5.1, were selected based on interviews with industry experts who felt that these dimensions were achievable and nearly economic with today's technology. All these constraints proved to be binding in most cases, indicating the potential value of developing new materials or manufacturing technologies that could push those limits lower. However at this time there exist hydrodynamic uncertainties such as oil fouling and refrigerant distribution that may prove to be even more costly to resolve. It is therefore advisable to conduct parallel research to quantify the thermal-hydraulic benefits associated with further reductions in fin and tube thicknesses. If refrigerant distribution or oil clogging in microchannel ports turn out to be show-stoppers, then materials- and manufacturing-related research could be redirected accordingly.

Table 5.1. Lower limits imposed

Round copper tubes	
Outer diameter	7.0 mm
Wall thickness	0.25 mm
Flat multiport aluminum tubes	
Wall thickness	0.4 mm
Web thickness	0.2 mm
Aluminum fins	
Thickness	0.06 mm

The following subsections summarize the implications for improving the performance of both round- and flat-tube heat exchangers, and the material- and manufacturing-related issues that must be addressed.

5.1 Heat exchangers with flat multiport tubes

Semi-empirical correlations for friction factors and Nusselt numbers for 3D rectangular channel airflow were developed, making use of physically known limits to facilitate global optimization. The curves were fit to analytical and numerical results for 2D and 3D channels that had previously been found to approximate experimental data within a few percent. The RMS errors of the curve fits developed here are of comparable magnitude.

The correlations were used to identify optimal configurations for plain fin heat exchangers with flat multiport tubes. Results were compared to those obtained using published empirical correlations for heat exchangers having louvered fins. Surprisingly, the plain fin heat exchangers outperformed the louvered fins on a per unit mass basis. However the latter optimizations were constrained by the limited empirical data sets underpinning the louvered fin correlations.

Sensitivity analyses demonstrated that, for a fixed core mass, system performance is relatively insensitive to the conductivity of the alloys used for the fins, because adjustments in fin height and fin pitch could largely offset

the degradation. Results also showed how performance can be improved 5-7% for both fin types by increasing the face area by 50%, or by increasing overall condenser fan/motor efficiency from 10 to 30%. In both cases, these improvements were achieved without increasing mass of the heat exchanger – simply by reconfiguring such parameters as fin and tube pitch, etc. These analyses revealed the existence of a relatively flat optimum in the multidimensional parameter space, in which a constraint on one parameter can often be substantially offset by adjustments in other heat exchanger dimensions. In the case of plain fin heat exchangers, the potential advantages of a multi-layer cross-counterflow configuration are negated by the pressure drop penalty associated with re-starting the boundary layer. The simulations suggest that single-layer cores are more efficient.

While the performance penalty for using louvered fins is small, the buckling resistance provided by the louvers may justify the incremental cost of the harder alloy and tooling required. On the other hand the plain fins are likely to provide superior performance and extended defrost intervals during winter heat pump operation, because louver-related heat transfer enhancements are lost quickly during frosting.

Because such heat exchangers undergo CAB brazing, strength-related issues dictate the use of manganese-containing alloys for tubes because their post-brazing strength can still meet constraints on burst pressure and core stiffness. These 3000-series alloys are also used to make louvered fins, because their hardness facilitates louver-cutting. Thermal stresses during brazing create a risk of buckling when serpentined fins are used, and louver closure due to creep if fins are too tall. These constraints have been partially ameliorated with the advent of plate fins that are bent in such a way as to reduce or eliminate the buckling risk, but the other constraints remain.

This report challenged the current paradigm which evolved from the early development of flat-tube heat exchangers to meet the severe packaging constraints of automotive condensers in a high face-velocity environment. Within this paradigm, heat exchanger performance was maximized using louvered fins (to reduce weight and take advantage of the high face velocity), which in turn provided the necessary structural stiffness and strength to survive the annealing effects of brazing. However it is louvered fins that require short fins and therefore more tubes, increasing material cost and weight. Outside this paradigm little data exists at the present time, but many other options could be considered. For example designs based on tall plain fins can achieve high fin efficiencies by fully utilizing even the thinnest fin stock in a lower face velocity environment, yet maximize heat transfer coefficient by creating nearly 2-D channels with taller fins and smaller fin pitch than louvered fins can efficiently tolerate.

Basically it is the brazing process that dictates the need for stronger alloys, which in turn increase the cost of extruding extremely small-diameter ports and thin walls and webs. If acceptable fin-tube contact could be achieved without brazing, softer 1000-series galvanically-compatible alloy pairs might be used for both fins and tubes. The cold-worked strength of these alloys appears sufficient to produce cores having the necessary stiffness, depending on how the fins are attached. Recall that louvers provide a moment of inertia large enough to resist buckling during brazing, a situation synergistic with hydrodynamic considerations that dictate that louvered fins be short in order to avoid excessive air-side pressure drop. However if plain fins are used, concerns about buckling and stiffness may persist because the optimal configuration calls for fins that are much taller (~14 mm) and a lower face velocity that still permits fins to be as thin as manufacturing and handling constraints allow. However these concerns are highly dependent on fin geometry and the type of brazing fixtures employed.

These findings underscore the importance of seeking to

- develop ways to achieve acceptable fin-tube contact resistance without brazing, for example by designing fins with collars and forcing tubes through them;

- reducing reliance on fins as structural elements, perhaps by devising ways to provide core rigidity using tubes and headers alone, or with an external frame;
- reducing tube wall and web thicknesses, along with port diameters to the extent that oil issues permit; and
- developing new types of headers to ensure uniform refrigerant distribution in evaporators.

In plain fin applications where core depth is not constrained, air-side pressure drop can be reduced substantially by decreasing fin pitch to the limit imposed by fouling constraints to reduce the aspect ratio of the air flow path, by using taller fins and fewer tubes. The quest for the highest system efficiency will then lead to substituting more material as the limit on heat transfer coefficient is approached, increasing core depth significantly while slightly increasing fin pitch to maintain low aspect ratio. At the same time, fin height and thickness can be increased to maintain high efficiency while reducing the number of tubes required. At some point the fan power requirement will reach a point where adding heat transfer surface becomes counterproductive, and the only remaining option is to relax the face area constraint, thus increasing the air flow rate to provide a larger heat sink or source. If tube width constraints are encountered along the way, it may be necessary to abandon extrusion and switch to brazing web inserts inside a flattened round tube, or to tolerate the performance penalty associated with multi-layer heat exchangers.

Finally it should be emphasized that although the simulation analyses were conducted for aluminum tubes and fins, flat-tube heat exchangers can be made of copper which is a more costly but stronger and more highly conductive material. The thermal-hydraulic payoffs of thinner fins and tubes are the same, but the material and manufacturing-related constraints are less well known because there is less experience with such designs. Recent increases in copper price may eliminate this option, and may require highly enhanced surfaces (e.g. offset strips to restart boundary layers) instead of seeking to substitute material cost for energy cost. Different fabrication options also exist, for example induction welding to make flat tubes having very small features on the refrigerant side, and small minor and large major diameters.

5.2 Round tube heat exchangers

A new set of physically based semi-empirical correlation was developed for predicting heat transfer and pressure drop in round tube plain fin heat exchangers having large fin and tube pitches. The functional form of the correlations was defined to facilitate representation of enhancement mechanisms observed in small-scale controlled experiments on single tubes and fins. It is based on separate fin and tube coefficients, with an enhancement factor applied to fin heat transfer reflecting the effects of vortices shed from the tubes. This physical model is valid only for laminar flow and is more accurate when fin and tube pitches are large. The accuracy was confirmed by comparison with the limited amount of published data and empirical correlations available for this relatively unexplored part of the parameter space.

Eventually it is expected that this physically-based model can be combined with published empirical correlations that are widely used for heat exchangers having small fin and tube pitch, but which cannot be reliably extrapolated outside their limited range of applicability.

These new semi-empirical correlations, along with purely empirical correlations already available, were used in a residential air-conditioning model to determine the optimal condenser configuration and performance/mass tradeoffs. The empirical correlations compared plain, slit, and louvered fins. All three empirical correlations were

found to severely limited by their underlying data sets, forcing the optimization algorithm to stop at their boundaries. Results suggested that optimal designs required larger fin and tube pitch, especially for heat exchangers having enhanced fins.

A second set of optimization analyses used the semi-empirical plain-fin correlations, which accurately represented tradeoffs in heat exchangers having very large fin and tube pitch. However these optimizations were also constrained by the lower bound on fin pitch. Together the results suggest that the most efficient a/c condenser design (having plain fins to facilitate defrost in heat pump mode) would lie in the gap between the ranges of the empirical and physically-based correlations; i.e. tube pitch greater than 35-40 mm (assuming 7 mm tubes) and fin pitch on the order of 3 mm or slightly greater. Bridging this gap, with either empirical data or physical modeling, is left for future study.

Unit costs of drawn copper tubing escalate sharply as diameter is reduced, suggesting the need to consider alternative fabrication techniques. The principal material-related constraint on improving performance of round tube-plate fin heat exchangers results from the need for mechanical expansion using a mandrel after assembly, in order to ensure adequate fin-tube contact.

This limitation suggests the advisability of considering alternatives to mechanical expansion. Since there is very little published literature on the subject, it may be useful to consider an exhaustive list of possibilities, ranging from thermal adhesives to pneumatic expansion. The latter approach is currently used with (softer) thin-walled aluminum tubing in refrigerator evaporators. As in the case of flat tube heat exchangers, at some point the additional area provided by small diameters will dictate that smooth tubes are superior to microfinned tubes, due to their lower refrigerant-side pressure drop.

Again as in the case of flat multiport tubes, smaller diameters require more parallel circuits, so the refrigerant distribution problem begins to require fundamentally different solutions (e.g. flash gas bypass) as tube diameters drop below ~7 mm o.d.

List of References

Aluminum Association, “Aluminum design manual” Arlington VA, 2000

Beaudoin, A. Private communication, University of Illinois at Urbana-Champaign, 2006

Beavers, G. S., E. M. Sparrow, R. A. Magnuson. “Experiments on hydrodynamically developing flow in rectangular ducts of arbitrary aspect ratio, Int. J. Heat Mass Transfer, Vol. 13, 1970, p. 689-703.

Bullard, C. W., J. M. Yin, and P. S. Hrnjak, “Compact Counterflow Gas Cooler for R744,” Transactions of ASHRAE, 108:1, 2002, p. 487-491.

Chang Y. J. and C. C. Wang. “A generalized heat transfer correlation for louver fin geometry” Int. J. Heat Mass Transfer, Vol. 40, No. 3, 1997, p. 533-544.

Copper Development Association, “Properties of wrought and cast copper alloys”, www.copper.org New York NY, 2006

Curr, R.M., D. Sharma, and D. G. Tatchell. “Numerical predictions of some three-dimensional boundary layers in ducts”, Computer Methods in Applied Mechanics and Engineering 1, 1972, p. 143-158

Elbel, S. and P. S. Hrnjak, “Experimental validation and design study of a transcritical CO_2 prototype ejector system” 7th Gustav Lorentzen Conference on Natural Working Fluids, International Institute of Refrigeration, Trondheim Norway, May 2006

Granryd. E. "Varmeovergang och tryckfall vid patryckt stromning genom flanselement" Kulde, 19:4, 1965, p. 88-105.

Hu, X. and A. M. Jacobi. "Local heat transfer behavior and its impact on a single-row, annularly finned tube heat exchanger" Journal of Heat Transfer, Vol. 115, 1993, p. 66-74

Ichimiya, K., N. Akino, T. Kunugi, and K. Mitsushiro. "Fundamental study of heat transfer and flow situation around a spacer (in the case of a cylindrical rod as a spacer)" Int. J. Heat Mass Transfer. Vol. 31, No. 11, 1988, p. 2215-2225.

Javeri. V. “Combined influence of Hall effect, ion slip, viscous dissipation and Joule heating on MHD heat transfer in a channel” Heat and Mass Transfer, Vol. 8, 1975, p. 193-202.

Kakac, S., R. K. Shah, W. Aung. Handbook of single-phase convective heat transfer, John Wiley & Sons, Inc. 1987.

Kawamura, T., M. Hiwada, T. Hibino, I. Mabuchi, and M. Kumada. "Heat transfer from a finite circular cylinder on the flat plate" Bulletin of JSME, Vol. 27, No. 233, 1984, p. 2430-2439.

Kim, Y. and Y. Kim. "Heat transfer characteristics of flat plate finned-tube heat exchangers with large fin pitch" International Journal of Refrigeration Vol. 28, 2005, p. 851–858.

Kulkarni, T. and C. Bullard, “Design tradeoffs in microchannel heat exchangers” ACRC TR-208, University of Illinois at Urbana-Champaign, February 2003

Mills. A. F. “Heat and mass transfer” Burr Ridge III.: Irwin, 1995.

Muzychka Y. S. and M. M. Yovanovich. "Laminar forced convection heat transfer in the combined entry region of non-circular ducts" Journal of Heat Transfer, Vol. 126, 2004, p. 54-61.

Saboya F. E. M. and E. M. Sparrow. "Local and Average Transfer Coefficients for One-Row Plate and Tube Heat Exchangers Configurations" Journal of Heat Transfer, 1974, p. 265-272.

Saboya F. E. M. and E. M. Sparrow. "Transfer characteristics of two-row plate fin and tube heat exchanger configurations”, Int. J. Heat Mass Transfer, Vol. 19, 1976, p. 41-49.

Shah R. K. and A. L. London. "Laminar Flow Forced Convection in Ducts, Supplement 1 to Advances in Heat Transfer" Academic, New York. 1978.

Stephan. K. "Warmeubergang und drauckabfall bei nicht ausgebildeter Laminarstromung in Rohren und in ebenen Spalten" Chem.-Ing.-Tech., Vol 31, 1959, p. 773-778.

Wang, C. C. C. J. Lee, C. T. Chang, and S. P. Lin. “Heat transfer and friction correlation for compact louvered fin-and-tube heat exchangers” Int. J. Heat Mass Transfer 42, 1999, p. 1945-1956.

Wang, C. C. K. Chi, and C. Chang. “Heat transfer and friction characteristics of plain fin-and tube heat exchangers, part II: Correlation” Int. J. Heat Mass Transfer 43, 2000, pp 533-544.

Wang, C. C. W. S. Lee, and W. J. Sheu. ”A comparative study of compact enhanced fin-and-tube heat exchangers” Int. J. Heat Mass Transfer 44, 2001, p. 3565-3573.

White F. M. “Fluid Mechanics” McGraw-Hill series in mechanical engineering, 4th ed. Boston, 1999.

Wibulswas, P. “Laminar Flow Heat Transfer in Non-Circular Ducts”, Ph.D. Thesis, London Univ., London, 1966.

Wiginton C. L. and Dalton C. “Incompressible Laminar Flow in the Entrance Region of a Rectangular Duct”, J. Appl. Mech., Vol. 37, 1970, p. 854–856.

Zukauskas, A. and A. B. Ambrazyavichyus. “Heat Transfer from Tubes in Cross Flow” in J. P. Hartnett and T. F. Irvine, Jr., Eds., Advances in Heat Transfer, Vol. 8, Academic Press, New York. 1972.

Appendix A. Correlations

A.1 Correlations Introduction

The computational experiment of optimizing the condenser in an air conditioning system compared five types of heat exchangers. Three have round tubes: Plain, louvered, and slit fins, and two have microchannel tubes: plain and louvered fins. A different airside heat transfer and pressure drop correlation set was used for each heat exchanger type. Two correlation sets were used for the round tube plain fin heat exchanger: an empirical model by Wang et al. (2000) and the semi-empirical enhanced wake model developed in this paper. This gives a total of 6 correlation sets, each with their own limits on search variables. This section describes the limits and optimal condenser configuration for each correlation set.

In all microchannel runs it was found the minimum tube port diameter and web thickness were optimal (0.6 and 0.2 mm). These lower limits were added to these variables due to manufactibility. In all round tube runs a tube diameter less than 7 mm was always found to be optimal. A lower limit of 7 mm was placed on tube outer diameter for all round tube runs because smaller tubes are not currently used and are said to be too costly to manufacture and to mechanically expand against the tubes.

A.2 Empirical Correlations

A.2.1 Flat tube louvered fin

Louvered fins are very common in microchannel heat exchangers. Unfortunately, the complex air flow caused by louvered fins is very difficult to solve analytically. For this reason empirical correlations are used. The problem with using empirical correlations is that their applicability is limited to parts of the parameters space covered by the underlying test data. The Chang and Wang (1997) correlations were used to find the air side heat transfer coefficient and pressure drop. The limits of this correlation's parameter space are listed in Table 1A. These bounds were selected to enclose between 90 and 100% of the underlying test data, depending on data density. The test points outside the parameter space were considered outliers and therefore not included. The same criteria were used to select bounds for all other empirical correlations.

Table 1A. Chang and Wang's (1997) louvered fin microchannel tube correlation limits

Lower limit	Design Variable	Upper limit
1.1	F_p	2.2
0.06	F_t	0.16
8	F_h	19
20	depth	44
100	Re_{Lp}	3000
1	L_p	3
10	L_{angle}	28

The lower limits on fin thickness and fin pitch are set to reflect manufacturing and fouling constraints. The other constraints are purely empirical and limit the optimization as shown in Table 2A. The velocity range covers face velocities from 1.3 to over 35 m/s. This is very high for most residential air conditioning systems because the correlation was designed for automotive applications, where velocities are much higher.

Table 2A shows the minimum system power usage for a range of depths with the louvered fin microchannel tube condenser. The louver parameters are not indicated because in all runs the louver pitch went to the lower limit and louver angle went to an intermediate value (1 mm and 23°). Notice that the lower limit on fin pitch does not constrain the optimization; the upper limit does for depths larger than 33 mm. Fin height and fin thickness constrain the optimization at the lower limit at every depth.

Table 2A. Optimal search variables, mass, and system work for louvered fin microchannel tube condensers of varying number of rows.

depth	V_{face}	F_p	F_h	F_t	m	W_{sys}
20	1.6	1.5	8.0	0.06	8	2.70
23	1.7	1.6	8.0	0.06	9	2.69
27	1.8	2.0	8.0	0.06	10	2.67
33	1.7	2.1	8.0	0.06	12	2.65
37	1.7	2.2	8.0	0.06	13	2.64
41	1.6	2.2	8.0	0.06	15	2.64
44	1.6	2.2	8.0	0.06	16	2.63

The behavior of the Chang and Wang (1997) correlation may be due to the fluid mechanics involved with louvered fins. However, it may be due to an inconsistency between the correlation data points and the optimal configuration. The optimal configuration has small fin height and large fin pitch; it lies in the upper left corner of Figure 1A, where the bounds of the correlation are defined by the rectangle. The points show the experimental data used in constructing the Chang and Wang (1997) correlation. The box shows parameter space for which the data was within around 90-100% of the maximum and minimum values; this was assumed to be the parameter space of validity. The optimal solution lies at the upper left corner of the box. Since it occurs at the boundary and is not surrounded by test data points, it actually reflects an extrapolation of the data. The majority of test points lie along the diagonal; only 4 lie clearly in the upper left quadrant. At the optimal louvered configuration, system power is most sensitive to the fin pitch and fin height search variables.

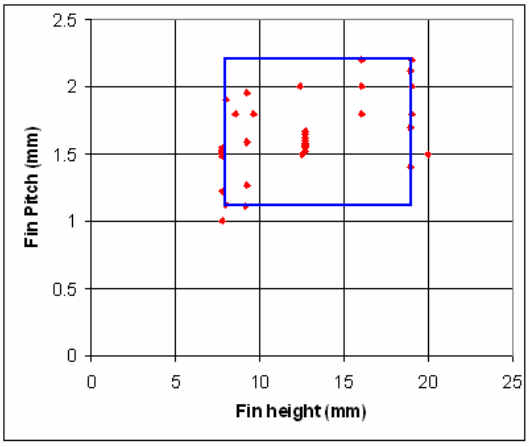

Figure 1A- Experimental fin pitch and height data used in constructing the louvered microchannel Chang and Wang (1997) correlation.

A.2.2 Round tube plain fin

The empirical Wang et al. (2000) correlation for a plain fin round tube heat exchanger is based on test data from 74 different heat exchanger geometries using 7 different design variables not including face velocity. The correlation is valid only within the upper and lower limits of each design variable, shown in Table 3A. The limits were selected with the same criteria as the louvered fin microchannel limits

Table 3A. Upper and lower bounds of the Wang et al. (2000) plain fin round tube heat exchanger.

Lower bound	Design variable	Upper bound
1	N	6
1.2	F_p	3.2
0.115	F_t	0.2
17.7	S_t	31.75
6.7	D	13.335
12.4	S_l	27.5

When the round tube plain fin correlations were used to minimize system power, the empirical limits again constrained optimization. Only for the two row condenser was an interior optimum found. The one row condenser was limited by the lower bounds on fin pitch and fin thickness and condensers of three and more rows were limited by the upper bound on tube pitch. For five and more rows the upper limit on fin pitch was reached as shown in Table 4A.

Table 4A. Optimal search variables, mass, and system work for plain fin round tube condensers of varying number of rows.

N	V_{face}	F_p	S_t	F_t	m	W_{sys}
1	1.6	1.2	27	0.12	8	2.95
2	1.4	1.6	31	0.14	15	2.74
3	1.4	2.2	32	0.14	18	2.71
4	1.4	2.5	32	0.14	22	2.69
5	1.4	3.2	32	0.14	23	2.67
6	1.3	3.2	32	0.14	28	2.68

A.2.3 Round tube louvered fin

The empirical louvered fin round tube correlations are more restrictive in the design variables than the plain fin round tube correlations, as shown in Table 5A. The may explain why plain fins outperform for every number of tube rows except one. Wang et al. (1999) reported no limits on fin thickness, so the same fin thickness limits are the plain fin case were used. This should not make a large difference because fin thickness primarily affects fin efficiency and mass, neither of which appear directly in the correlations for heat transfer coefficient and pressure drop.

Table 5A. Correlation limitations of Wang et al.'s (1999) louvered fin round tube correlations.

lower limit	Design Variable	upper limit
1	N	6
200	Re_{Dc}	8000
1.21	F_p	2.49
17.7	S_t	25.4
13.6	S_l	19.05
6.93	D_c	10.42
0.9	L_h	1.4
1.7	L_p	3.75

Louver height and louver pitch were found to be optimal at the lower limits of the correlation for every run and were not included with the other search variables in Table 6A. The optimization is limited by the lower bound on fin pitch for one row and the upper bound on tube pitch for two and more rows. The upper bound on fin pitch also limits optimization for three or more rows. System power consumption actually increased for more than three rows because the condenser configuration is so heavily constrained that face velocity must start decreasing to avoid excessive pressure drop.

Table 6A. Optimal search variables, mass, and system work for louvered fin round tube condensers of varying number of rows.

N	V_{face}	F_p	S_t	F_t	m	W_{sys}
1	1.3	1.2	21	0.13	7	2.93
2	1.4	2.2	25	0.13	10	2.78
3	1.3	2.5	25	0.13	15	2.76
4	1.2	2.5	25	0.13	19	2.78
5	1.2	2.5	25	0.13	24	2.81
6	1.1	2.5	25	0.13	29	2.85

A.2.4 Round tube slit fin

Slit fins show the best performance for round tube heat exchangers of three or less rows. They are also the most efficient use of mass for this application. Table 7A shows the empirical correlation limits for the slit fin round tube correlations by Wang et al. (2001).

Table 7A. Correlation limits of Wang et al.'s (2001) slit fin round tube correlations.

Lower bound	Design variable	Upper bound
1	N	4
1.21	F_p	2.50
0.11	F_t	0.2
20	S_t	25.4
7.52	D_c	10.34
4	N_{slits}	7
1	$slit_t$	2.2

The optimization of this condenser was constrained on several search variables, but still shows the best performance. Optimal values of search variables are shown in Table 8A below. In actual design of a heat exchanger, the number of slits must be an integer value. Table A8 shows a non-integer for some rows because the optimization was not constrained to integers only. The numbers can be rounded to the nearest integer value with little change in system performance.

System performance could be even better if correlations could be extended. The slit fin round tube correlation is limited by the upper limit on tube pitch and the lower limit on fin thickness at every step. The lower bound on fin pitch constrains the single row optimization. The lower limit on tube diameter was extended from 7.1 to 7.0 mm in order to be consistent with other round tube investigations and current designs. This extension has a negligible effect on correlation predictions.

Table 8A. Optimal search variables, mass, and system work for slit fin round tube condensers of varying number of rows.

N	N slits	V_{face}	F_p	S_t	F_t	m	W_{sys}
1	4	1.5	1.2	25	0.11	7	2.80
2	4	1.4	1.6	25	0.11	11	2.71
3	4.715	1.3	2.0	25	0.11	15	2.70
4	4.61	1.3	2.2	25	0.11	19	2.73

A.3 Semi-Empirical Correlations

A.3.1 3D channel flow - Flat tube plain fins

The 3D channel flow correlations were used to simulate a microchannel tube plain fin condenser. The inequality constraints imposed on the plain fin condenser are much less restrictive than the louvered fin condenser because of the correlations used. The Chang and Wang (1997) correlation is limited by manufacturing and empirical constraints while the 3D channel flow correlations are limited only by manufacturing constraints. Table 9A shows the inequality constraints imposed on the plain fin condenser. A lower limit of 1 mm was placed on fin pitch as a fouling constraint. The lower limit of 0.06 mm was placed on fin thickness as a manufacturability constraint. These 3D channel flow correlations could give accurate results without these limits, but such configurations are not practical. The upper limit on Reynolds number is to ensure laminar flow. It should be noted that the flow may still be laminar with a Reynolds number over 2000 if the boundary layers are still developing and have not touched on opposing sides. The lower limits on the non-dimensional depths, x* and x+, are the limits of the curve fit. These and any smaller values correspond to the heat transfer and pressure drop on a flat plate.

Table 9A. Correlation limits of the 3D channel airflow correlations as applied to a microchannel tube plain fin condenser.

Lower limit	Design Variable	Upper limit
1	F_p	none
0.06	F_t	none
none	F_h	none
none	depth	none
none	Re_{Dh}	laminar
1.5e-4	x*	none
1.9e-4	x+	none

$$Nu_x = 0.664 \cdot \mathrm{Re}_x^{1/2} \cdot \mathrm{Pr}^{1/3} \tag{1A}$$

Equation 1A is the laminar flat plate heat transfer equation. The 3D channel heat transfer correlation was constructed so that the flat plate heat transfer coefficient equals the channel heat transfer coefficient when x* is very small; this is shown as Equation 2A. The Stephan correlation captures this effect, but only for an aspect ratio of zero. In order to have the 3D channel flow correlation capture this, flat plate heat transfer coefficients were expressed using a hydraulic diameter Nusselt number and added to the flat plate region of Table 2.1. Any hydraulic diameter based Nusselt number can be expressed as a function of Prandlt Number and x* only assuming both heat transfer coefficients are equal, i.e. using Equations 1A and 2A and the definition of the Nusselt numbers, it can be shown that Equation 3A predicts the heat transfer coefficient for the leading edge of a channel.

$$h_x = h_{3D} \tag{2A}$$

$$Nu_{3D} = 0.664 \cdot (\mathrm{Pr})^{-1/6} \cdot (x^*)^{-1/2} \qquad \text{for small x*} \tag{3A}$$

Table 10A shows the optimal configurations of the microchannel tube plain fin condenser of various depths. Larger depth means larger mass, although this is not proportional due to the spreading of the fins and tubes as depth increases. Core depths less than 17 mm are not shown because fouling constraint on fin pitch precludes the existence of an interior optimum. The correlation is only limited by the lower bound on fin pitch at a core depth of 17 mm and under, and by the lower bound on fin thickness at several depths. These correlations are much less restricted by bounds than Chang and Wang's (1997) louvered fin microchannel correlations, and they can explore almost any depth[7]. This leads to better performance than the louvered fin correlation and a broader range of core depths explored.

Table 10A. Optimal search variables, mass, and system work for plain fin microchannel tube condensers of varying number of rows.

Depth	V_{face}	F_p [mm]	F_h [mm]	F_t [mm]	m [kg]	W_{sys} [kW]
17	1.6	1.0	9.8	0.07	7	2.68
25	1.5	1.1	11.5	0.06	9	2.65
33	1.5	1.2	13.3	0.07	11	2.63
41	1.5	1.4	15.0	0.07	12	2.63
49	1.5	1.4	16.7	0.07	13	2.63
57	1.5	1.5	17.0	0.07	15	2.62
65	1.5	1.6	17.0	0.06	16	2.62
73	1.5	1.7	15.1	0.06	19	2.61
81	1.5	2.0	15.7	0.09	21	2.60
121	1.5	2.0	18.5	0.06	25	2.60

A.3.2 Enhanced wake model - Round tube plain fin

The enhance wake model was used to predict the heat transfer coefficients and pressure drops in round tube plain fin heat exchangers. The limits on this correlation are not precisely known because the correlation has not yet been compared to large amounts of data. It was shown that the correlations have better accuracy compared to

[7] 3D the channel flow correlations have a lower limit on depth. See 3D channel flow correlation development and Table 9A

extrapolated empirical correlations for larger fin and tube pitches. However there are no specific lower bounds yet defined for some design variables. The accuracy of the heat transfer correlation has been found to be quite good for large fin and tube pitch, within 5% for 10 mm fin pitch and 27 mm tube pitch (see section on correlation development). This is because the correlation was constructed to approach known limits at infinite fin and tube pitch. The accuracy of the pressure drop correlation is not as good because of the lack of data available on the subject. Table 11A shows some of the bounds applied to the enhanced wake correlation when applied to a single layer condenser.

Table 11A. Correlation limits of the enhanced wake correlation (plain fins round tubes)

Lower bound	Design variable	Upper bound
1	N	none
-	F_p	none
none	F_t	none
-	S_t	none
-	D	-

The optimal configuration of a condenser when using the enhanced wake correlation depends on how the bounds are imposed. When optimizing, the fin pitch will always go to the lowest value allowed because it predicts an excessively high heat transfer coefficient here. For example, when 3.2 mm is chosen for the lower bound on fin spacing, the optimal configuration will reach that value. When 3.2 mm is used, the optimal 15 kg condenser uses the same system power as the optimal 15 kg condenser as predicted by the Wang et al. (2000) correlations for plain fins round tubes (see section 3.5.3). However, this is accompanied by an overestimation of heat transfer and pressure drop compared to Wang et al. (2000) at the edge of its applicable range. When 4 mm is used for fin spacing, the results are more accurate when compared to Granryd's correlations, but the system power is substantially higher when the 4 mm lower bound is applied. Sections 3.5.3 and 3.6 describe optimization using the enhanced wake correlations in more detail.

The accuracy of the enhanced wake correlations will now be discussed. Figures 2A – 5A show heat transfer coefficients predicted by enhanced wake and Wang et al. (2000) correlations for: 2 rows, 0.12 mm fin thickness, 10 mm outer diameter tubes, and 1.4 m/s face velocity. Only tube pitch and fin pitch were varied in these figures because these variables have the greatest effect on performance. The vertical lines show the limits of the Wang et al. (2000) correlations. Generally, the results show that the enhanced wake correlation does a poor job for small fin and tube pitch, while its accuracy improves near the upper limits of the Wang et al. (2000) correlation. Conversely the Wang et al. (2000) correlation fails to converge towards known physical limits as fin and tube pitch become large.

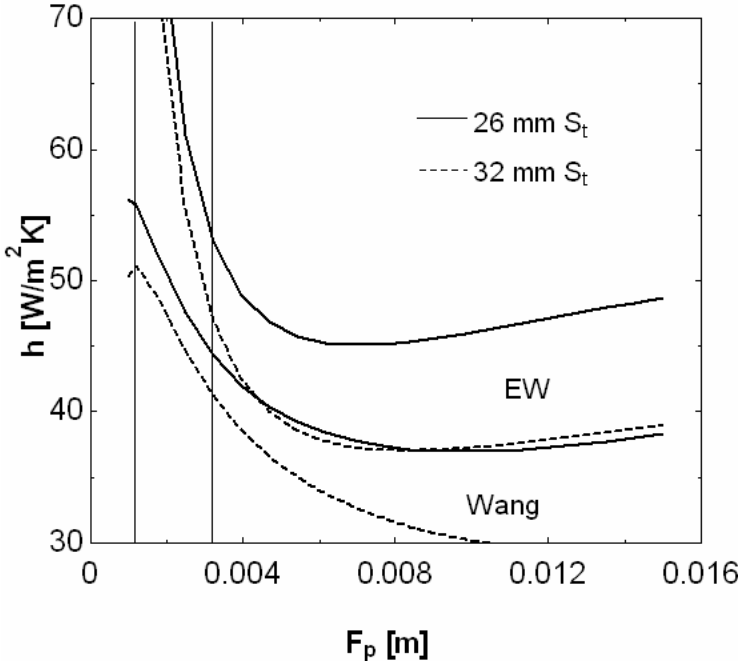

Figure 2A. Heat transfer coefficient varying fin pitch

Figure 2A show how the enhanced wake and Wang et al. (2000) correlations predict how heat transfer coefficient vary with fin pitch. The enhanced wake correlation was shown to be accurate for large fin and tube pitch (See sections 3.4 and 3.5). In these configurations, it appears to vary in accuracy within Wang et al.'s (2000) parameter space (Maximum error of 100% for minimum fin pitch, minimum error of 13% for maximum fin and tube pitch). The Wang et al. (2000) correlation (shown by the lower set of lines) is accurate within its bounds. When extrapolated to fin pitches over 8 mm, the 32 mm tube pitch curve does not show the reversal in trend shown by the enhanced wake correlation. Such a reversal is consistent with physical reality and occurs because the fraction of fin airside area is decreasing relative to tube airside area. Tubes have an 80% higher heat transfer coefficient at this configuration. The Wang et al. (2000) correlation predicts lower heat transfer than enhanced wake because it extrapolates the rapidly decreasing trend of small fin pitch to larger fin pitch values.

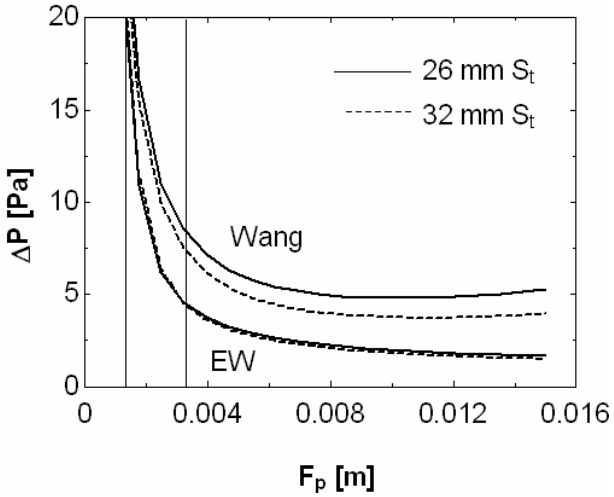

Figure 3A. Pressure drop varying fin pitch

Figure 3A shows how the two correlations predict pressure drop for varying fin pitch. The enhanced wake correlation under predicts pressure drop for all configurations because it does not include the pressure drop required to create root vortices. Within the empirical parameter space, the enhanced wake correlation predicts pressure drop 6% less than Wang et al. (2000) for the lower bound on fin pitch (1.2 mm) and upper bound on tube pitch (32 mm), and 50% less for the upper bound on fin pitch and 26 mm tube pitch. Both correlations show similar trends for fin pitches under 10 mm. For fin pitches larger than 10 mm, the Wang et al. (2000) correlation shows pressure drop increasing with fin pitch, which is not a realistic solution.

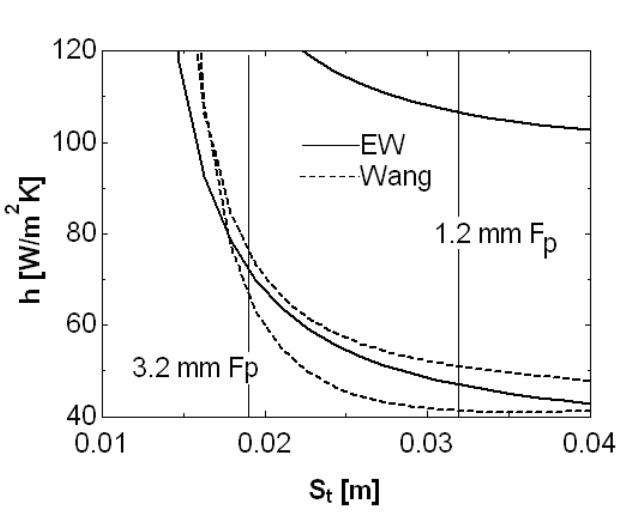

Figure 4A. Heat transfer coefficient varying tube pitch

Figure 4A shows that the enhanced wake correlation overestimates heat transfer (by up to 100%) within the empirical bounds for 1.2 mm fin pitch (upper two lines) for all tube pitches. The two correlations predict more similar heat transfer coefficients (maximum difference of 20% for 24 mm tube pitch) for 3.2 mm fin pitch (lower two lines). Both correlations show consistent trends versus tube pitch for all configurations shown in Figure 4A.

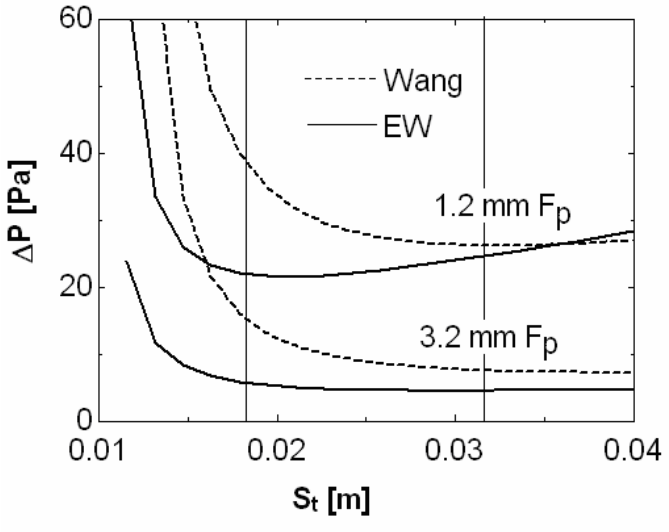

Figure 5A. Pressure drop varying tube pitch

Figure 5A shows how the two correlations predict pressure drop for varying tube pitch. Both correlations show pressure drop decreasing with increasing tube pitch as tubes are moved apart. The enhanced wake correlation shows a reversal in this trend for tube pitches larger than a certain value (21 mm at 1.2 mm fin pitch, 30 mm at 3.2 mm fin pitch). It is reasonable that this trend occurs because pressure drop increases with tube pitch as the core is made deeper. This reversal is unlikely at the lower fin pitch, because the enhanced wake correlation does not capture the physics of the flow there. The reversal is more likely at the larger fin pitch; the Wang et al. (2000) correlation does not capture it there because the correlation carries its small tube pitch trend to larger tube pitches.

Appendix B. Condenser Optimization Sensitivity

B.1 Sensitivity Introduction

This appendix describes the sensitivity to the equality constraints in detail. For microchannel tubes the plain and louvered fins were examined; the equality constraints shown in Table 2.5 can be changed for better performance and manufacturability. For round tubes the plain fins were examined using an empirical and semi-empirical correlation set. Table 3.2 shows the base case round tube equality constraints.

B.2 Microchannel Louvered

Several 10 kg condensers were compared to a base case optimal condenser of 10 kg with the constraints shown in Table 2.5. When face area is increased to 1.5 m^2 the 10 kg of aluminum changes configuration. The depth decreases 27% and moves to the minimum correlation bound of 22 mm. The fin height grows 12% to 9 mm. and the fin pitch increases 5% to 2.1 mm. The larger face area condenser uses around 5% less system power than the base case do to the larger heat sink from the 31% increase in air volume flow rate.

Another way to improve condenser performance is to increase the fan efficiency. This can be accomplished by using an efficient motor or improving fan placement. When condenser fan efficiency in increased to 30% (from the base case of 10%) the search variables change to use 6.5% less system power. Fin height remains at its lower bound of 8 mm. Fin pitch increases to its upper bound of 2.2 mm. Fin thickness and face velocity increase 17% and 43%. The higher face velocity provides a larger heat sink and higher airside heat transfer; the thicker fins keep fin efficiency high (92%).

Thermal conductivity varies significantly among the aluminum alloys used for making fins. Nearly pure aluminum (e.g. 1000 and 1100 series alloys) has a thermal conductivity around 237 W/mK, as used in the base case. The harder alloys used for louvered fins may a conductivity as low as 160 W/mK. The optimization analysis was repeated for the 10 kg heat exchanger assuming that the harder alloy was used. Face velocity was the only search variable to change, increasing 3% while system power increased 0.3%.

B.3 Microchannel Plain

B.3.1 Microchannel Plain – sensitivity to design constraints

A different optimal design is reached when the optimization is repeated with a 1.5 m^2 face area constraint, and 10 kg condenser mass. The larger face area results in about 5% lower system work for each of 1, 3 and 5 crossflow layers. The single layer condenser once again shows the better performance than any number of multilayers.

Another feasible way to improve performance is to increase the condenser fan/motor efficiency. For all previous runs this efficiency was set at 10%, a typical value for many residential split systems. It is possible to achieve condenser fan efficiencies around 30% with motor improvements and optimal positioning of the fan and condenser. For a one layer 10 kg condenser, the optimal condenser geometry changed as the system power consumption decreased 7%. This is due to the condenser fan and compressor work decreasing 33% and 6% respectively (63 and 114 W) compared to the base case.

The optimization analysis was repeated for the 10 kg heat exchanger assuming that the stronger, less conductive alloy was used, resulting in system power consumption increasing 0.4% (10 W). The optimal geometric variables change very little. Only fin height changes by any appreciable amount; it decreases 8% to prevent fin efficiency from dropping very far (-3%). The resulting shift of material from fins to tubes results in a 5% smaller

core depth as the 10 kg of metal is rearranged. Interestingly, the fin thickness remained at its lower bound despite the lower conductivity.

Figure 1B shows the percent improvement in system power when an equality constraint is changed. Multilayer condensers were not considered because they were shown to offer lower performance compared to a single layer. Figure 1B shows that increasing face area or fan efficiency increases performance much more than increasing mass 50% to 15 kg. This is due to the effect of diminishing improvement as condenser mass is increased.

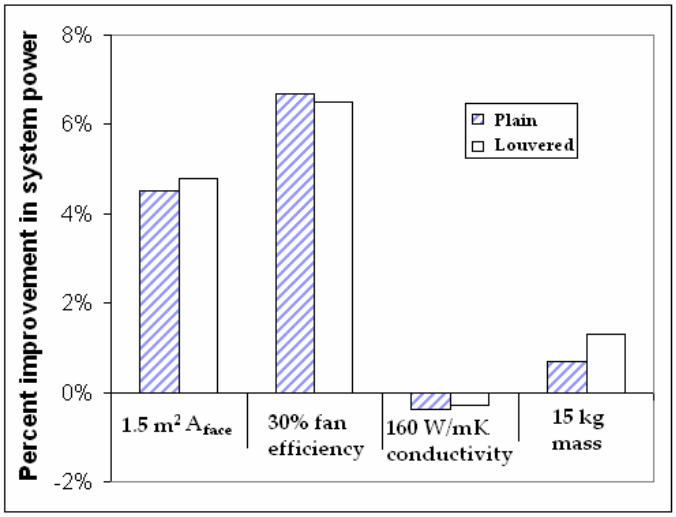

Figure 1B. Sensitivity of equality constraints for microchannel condensers.

B.3.2 Microchannel Plain – sensitivity to cost constraint

Constraining mass during the optimization is meaningful, but it is only accurate from a manufacturing standpoint if the cost of the fin mass plus tube mass is equal. In reality, the cost of the condenser will differ depending on the amount of fin and tube mass separately. The same 4 variable optimization was conducted on the plain fin microchannel tube condenser, with condenser cost constrained instead of mass. Condenser material cost was constrained to four values: 45, 50, 55, and 70 dollars. The optimization involved one case with cost estimates of fins at $4/kg and tubes at $6/kg. The second case valued fins at $6/kg and tubes at $4/kg. Figure 2B shows these three cases with increasing mass showing increased cost for each of the four cost constraints. Other constraints were the same as the base case of Figure 1B.

From left to right in Figure 2B the decreasing fin mass fraction suggests that more efficient (and costly) heat exchangers will require relatively more tubes, regardless of their cost relative to fins. When tubes were more costly than fins, system power consumption decreased 0.9%, as $45 heat exchangers were replaced with $70 ones. In the case where fins were more costly, the power was reduced 1%. Further details are provided in the following paragraphs.

In the expensive tubes case the optimization leads to denser fins and smaller fin height. The fraction of fin material is near the value of the 10 kg base case, as shown in Figure 2B. In the other case, when tubes are less expensive, the optimization spreads the fins apart and adds depth in order to reduce the mass fraction of fins. The fin height remains around the same value (14 mm) because larger fin height would lower the fin efficiency. Fin thickness remains at the minimum bound for all optimization because adding depth is a more efficient use of mass around this geometry. This is because more area has a larger effect on airside heat transfer than increasing fin

efficiency. Fin efficiency remains between 85 and 89% for all constrained cost runs. Adding fin thickness is beneficial in larger, more massive condensers as shown in Chapter 2.

In the $55 run, with $6/kg fins and $4/kg tubes, only the fin pitch changed substantially from the expensive tubes case. Fin pitch increased to allow a lower fraction of fins and save cost. This allowed more depth to be added to the condenser and the result was better performance at equal heat exchanger cost (with more mass). The best performance improvement occurred with the highest cost ($70) condenser, where system work was 0.2% lower compared to the expensive tubes case. Other improvements were around 0.15%. Figure 2B shows these $70 points as the right-most circle (expensive tubes case) and the right-most triangle (expensive fins case). Even though these condensers have the same cost, the expensive fins case condenser is almost 2 kg heavier than the expensive tubes case.

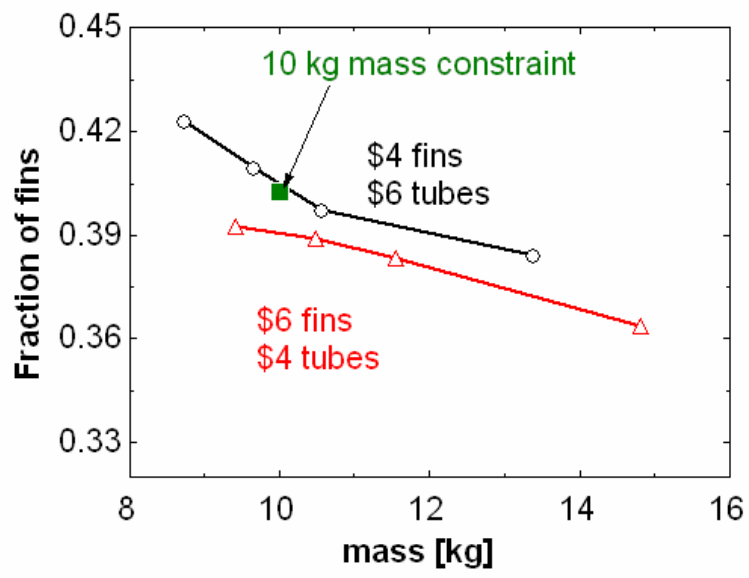

Figure 2B. Optimal fin mass fraction vary with cost

The fins and tubes are always spread further apart as mass increases. The spreading of the fins has a larger effect on fin mass, and this accounts for the decreasing fraction of fins as mass increases.

B.4 Wang ET AL. Correlations Round Tube Plain Fin Sensitivity

It has been shown that system power usage can be lowered by increasing the mass of the condenser. Figure 3 shows that for round tubes and plain fins the economic optimum between condenser mass and system power takes place at around 15 kg and 2 tube rows. Imposing these constraints and again optimizing the condenser geometry for minimum system work leads to a nearly identical configuration. This will be the base case for a number of comparisons. Other constraints are shown in Table 1B. The exchanger airside heat transfer and pressure drops were computed using the empirical correlation by Wang et al. (2000). The transverse tube pitch goes to its empirical upper bound of 31.75 mm. This and other optimal base case variables appear in Table 1B. In the unconstrained mass case depicted in Figure 3.6 the tube pitch was slightly below the upper bound; this is due to the broadness of the optimums.

Table 1B. Optimal variables for 15 kg base case Wang et al. (2000) condenser.

m [kg]	15
V_{face} [m/s]	1.5
S_t [mm]	32
F_t [m]	0.1
F_p [mm]	1.7
depth [mm]	55
W_{sys} [kW]	2.7
h [W/m^2K]	67
ΔP [Pa]	14
A_a [m^2]	62
A_{fin} [m^2]	61
A_r [m^2]	1.3
W_{comp} [kW]	2.1
$T_{sat,in}$ [°C]	45
W_{cond} [kW]	0.2
η_{fin}	0.8
T_{app} [°C]	1.9
$hA\eta_{fin}$ [W/K]	3422

When the face area constraint is increased from 1 to 1.5 m^2, the performance is improved significantly. The system power is decreased 6%, from 2.7 to 2.5 kW. This is due to the larger heat sink caused by a 31% higher airflow rate. The air velocity is 13% lower due to the larger face area, and this helps keep pressure drop small. The larger heat sink increases the mean temperature difference between the air and refrigerant and results in lower condensing temperature. The 1° C lower condensing temperature lowers compressor work by almost 5%. The depths of these two condensers are equal because both have 2 rows and a maximized tube pitch. Because mass is constrained to 15 kg in both cases, the larger face area condenser meets this constraint by decreasing fin thickness by 20% and increasing fin pitch by 37%. The larger fin pitch and lower face velocity lead to 15% lower heat transfer coefficient and 50% lower pressure drop. The lower heat transfer coefficient allows thinner fins to be used at less of a performance penalty; fin efficiency decreases by around 1%.

Performance also increases when the condenser fan efficiency is increased. The base case uses a fan and motor efficiency of 10%. The model shows that system power can be lowered 7% (from 2.7 to 2.5 kW) when fan efficiency is increased to 30% and the 15 kg of condenser core mass is reconfigured. The design variables all change from the base case in order to take advantage of the increased fan efficiency. The airflow rate and face velocity increase 24% (to 1.8 m^3/s) providing a larger heat sink. Higher air velocity and smaller fin pitch increase the heat transfer coefficient by 8%. Tube pitch decreases by 6% (to 30 mm) in order to keep fin efficiency high at 82%. Increasing fin thickness is not the preferred method to increase fin efficiency because the mass is better used to decrease fin pitch, which increases airside area and heat transfer coefficient. Fin thickness decreases 10% from the base case and fin pitch decreases 14%. Pressure drop increases by 64%, but fan power is lowered by 32% due to the increased fan efficiency.

When the stronger fin alloy is used, performance is lowered. The thermal conductivity of the stronger alloy is 160 W/mK whereas the conductivity of pure aluminum is 237. Using the stronger fin alloy increases minimum system work by 1%. The 15 kg of condenser mass is reconfigured to keep fin efficiency high. Fin efficiency decreases to 78% from 83% in spite of 10% thicker fins. The material is taken from fin pitch (reduced 11%) to provide the thicker fins. This decreases airside area by 10%, but airside heat transfer coefficient is decreased by only 2% because face velocity increases 3%. Wider fin pitch lowers pressure drop by 7% and fan power decreases 3%. The compressor power increases by 1.5% due to the airside $hA\eta_{fin}$ product decreasing 15% and the condensing temperature increasing by almost 1°C.

When condenser mass is reduced to 10 kg instead of 15 kg, the Wang et al. (2000) correlations predict that system power increases by almost 2.6%. The 5 kg of mass was taken from fins, where pitch increased from 1.7 to 2.3 mm. This is the preferred method of reducing mass in this case because larger fin pitch reduces friction factor and allows for increased face velocity to offset the loss of heat transfer coefficient and area. Tube pitch remains at the upper limit (32 mm) and fin thickness moves to the lower limit (0.12 mm) to maximize heat transfer area at this fin pitch.

B.5 Enhanced Wake Correlations Sensitivity

Design constraint sensitivity analyses were also conducted on the semi-empirical model to determine the response of heat exchangers having larger fin pitch (See section 3.8 for economic design sensitivity). In every case, the fin pitch attempts to move to as small a fin pitch is permitted. The minimum bound on fin pitch was set to 4 mm and this value is optimal for every case. The enhanced wake correlation shows a nearly 10% reduction in system power when face area is increased from 1 to 1.5 m^2. The airflow rate increases 21% from the base case, with 19% lower face velocity, resulting in a larger heat sink. The tube pitch and fin thickness are lowered 12 and 33% to conserve mass. Airside area increases 32%, which is the main factor in compressor power lowering 10% from the 2.7°C drop in condensing temperature. Fan power also decreases 19% due to 31% lower pressure drop from thinner fins and a shallower core.

Increasing fan efficiency to 30% lowers system power by almost 7%. The airflow rate increases 50% from the base case, resulting in a larger heat sink and higher heat transfer coefficient. About 10% of the 15 kg of metal moves from tube pitch to fin thickness in order to keep fin efficiency high at 89% (1.5% higher than the base case). The compressor power is lowered 7% due to the 23% higher heat transfer coefficient, and fan power is lowered 11% due to the higher fan efficiency.

Using a stronger fin alloy with a thermal conductivity of 160 W/mK increases system power only 1.3%. About 15% of the metal is again shifted from tube pitch to fin thickness to keep fin efficiency high at 88%. The airside area is lowered 15% as a result of this; the optimization tries to compensate by increasing airflow rate 4% to provide a larger heat sink. Compressor power is increased 1% due to the reduction in airside area and fan power is increased 11% due to the increased face velocity.

When condenser mass is reduced to 10 kg instead of 15 kg, system power increases by 1.6%. This is due to 30% thinner fins and smaller depth due to 15% smaller tube pitch. Tube pitch still remains larger than Wang et al.'s (2000) upper limit because more heat transfer area is needed. Face velocity is 8% higher than the base case to compensate for the reduced airside area. Compressor power still increases ~1% in spite of attempts to raise heat transfer. Fan power increased 8% because of the increased face velocity.

Figure 3B shows that increasing the condenser fan efficiency to 30% and face area to 1.5 m^2 achieve nearly equal performance. The exception is the enhanced wake correlations predict increasing face area is better than fan efficiency. This is because increasing the face area lowers fan and compressor work more than increasing fan/motor efficiency due to increased heat transfer area and lower pressure drop. The enhanced wake correlation shows better improvement in performance here because the fins are consistently spread to the minimum pitch, 4 mm. Increasing face area dictates that the fin be spread further apart, but in this case the fins were already spread far apart for the base case, hurting performance. It appears that increasing face area is more beneficial for round tube condensers. For the Wang et al. (2000) correlations with round tubes the increased face area case is constrained by the upper tube pitch bound (31.75 mm) and lower fin thickness bound (0.115 mm), indicating even more energy saving may be possible. Tube pitch is the only variable constrained in the base case and the low conductivity case; it is constrained at the upper bound. The ~6% energy savings or the increased fan efficiency for both cases is similar to the microchannel condenser system.

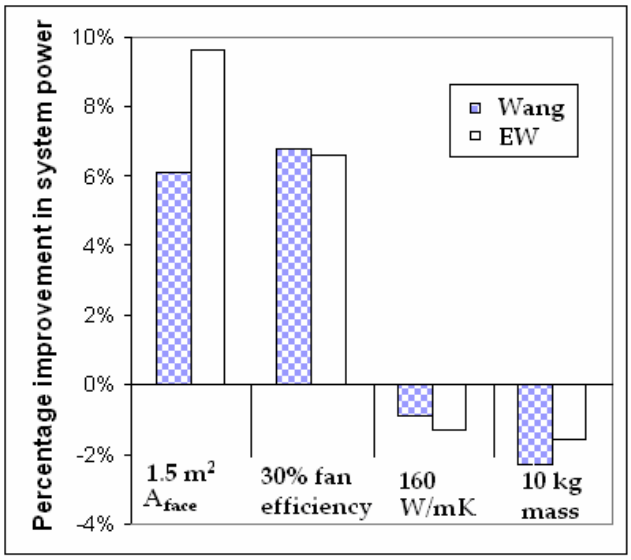

Figure 3B. Sensitivity of equality constraints for round tube plain fin condensers

Appendix C. Round Tube Plain Fin Physics

C.1 Round Tube Plain Fin Physics Introduction

Fluid flow over tube banks and fin arrays are easy to model separately. It is much harder to predict the behavior of a fluid flowing over a finned tube array, such as air flowing over a plain fin round tube heat exchanger. The fluid mechanics involved changes depending on the geometry of the heat exchanger and the air velocity. This section will focus mainly on low air velocity (~1 m/s) because high velocities are not suitable for HVAC applications. As for geometry considerations, fin spacing is very important. At relatively small fin pitch a stagnant wake forms behind a tube, severely lowering heat transfer. As fin spacing is increased, a Von Karman vortex street forms behind the tubes, increasing heat transfer on the fins. The parameters determining where this change occurs are not known, but it is expected to be a function of tube diameter, fin spacing, and Reynolds number.

The horseshoe-shaped root vortex forming at the fin-tube junction enhances heat transfer locally and forms in front of tubes regardless of fin spacing. The strength of this enhancement depends on the velocity which impinges on the tube. In staggered multirow heat exchangers, every row after the first will experience a stronger root vortex due to velocity contraction from the previous row. This Appendix uses data and information from experiments and compares them to physical models. The small fin pitch situation is discussed first, followed by the large fin pitch situation. This appendix uses data taken from Saboya and Sparrow (1974, 1976) and figures and data for Ichimiya et al. (1988).

C.2 Single Row Small Fin Pitch

The interacting boundary layers from the tubes and the fins cause significant changes in performance as shown in Figures 1C and 2C. These figures show the heat transfer coefficients and pressure drops versus transverse tube pitch as predicted by two different correlations. The first correlation, the empirical Wang et al. (2000) correlation, is based on experimental data and therefore includes tube-fin interactions within its range of applicability shown by the vertical lines on the Figures.

The second correlation is a superposition of tube bank and fin array heat transfer coefficients and pressure drop and does not include tube-fin interactions. The fin array calculations are performed using the 2D channel flow correlation, Equation 2.3. The superposition correlation predicts less system power usage for an air conditioning system with the same condenser configuration because it predicts less pressure drop and a higher heat transfer coefficient. This quantifies the extent to which tube-fin interactions hurt overall performance, at least for the specified fin pitch, face velocity, and tube diameter listed in Figures 1C and 2C, and within the tube pitch limits of the Wang et al. (2000) correlation. When fin pitch is larger, tube-fin interactions will be shown to increase the heat transfer coefficient.

The Wang et al. (2000) correlation predicts a higher heat transfer coefficient than the superposition when face velocity is high. This indicates that the net effect of interactions is to increase the average heat transfer coefficient at a high face velocity (6 m/s for configuration in Table 1B). This is of limited use however as much higher pressure drop makes a high face velocity unfavorable.

In Figure 1C below, the superposition correlation predicts a higher heat transfer coefficient than the Wang et al. (2000) correlation within the empirical bounds. The Wang et al. (2000) correlation is labeled with the number of tube rows; the line pattern indicates the corresponding number of tube rows for the superposition correlation.

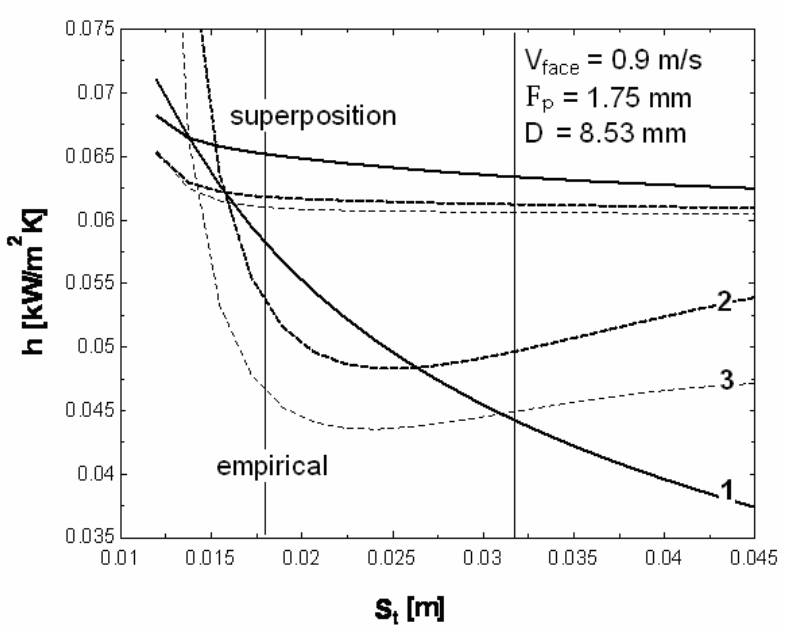

Figure 1C. Average heat transfer coefficients predicted by the superposition and Wang et al. (2000) correlations.

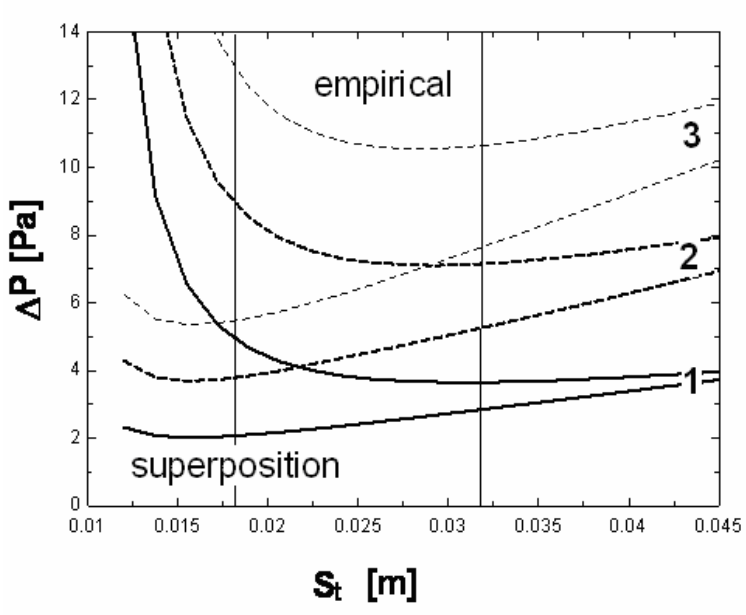

Figure 2C. Heat exchanger airside pressure drop versus tube pitch with same configuration as Figure 1C.

The difficulty in modeling tube-fin interactions stems from finding how the boundary layers formed by the tubes affect the heat transfer and pressure drop on the fin surface. The boundary layer on the fin surface has little effect on the transverse dependency of the heat transfer coefficient along the tube (Kawamura et al., 1984). The heat transfer from a finned tube is a function of angular position only for the middle 90% of the exposed tube length between fins. This indicates that tube-fin interactions have little effect on the tube heat transfer coefficient. It can be inferred that these tube-fin interactions also have little effect on the pressure drop contribution attributable to the tubes.

The tube-fin interactions do have a significant effect on the heat transfer and pressure drop as seen by the fins for many heat exchanger configurations, which is evident from Figures 1C and 2C. This is partially due to the formation of root vortices near the front of the tube; this happens at face velocities over 0.9 m/s with 1.75 mm fin pitch and 8.53 outer tube diameter according to (Saboya and Sparrow, 1974). For higher face velocities the root vortices become stronger and a secondary, weaker set of root vortices forms farther away from the tube centerline (Saboya and Sparrow, 1974). These secondary vortices begin to form at a minimum flow area velocity of 9.25 m/s and the same fin pitch and tube diameter as specified above. The onset of root vortex formation occurred at velocities of 5.75 m/s and up with a 38 mm diameter tube (Hu and Jacobi, 1993). Much higher heat transfer and pressure drop are experienced in this vortex region (Saboya and Sparrow, 1974).

Saboya and Sparrow (1974, 1976) published experimental results for a one and two row round tube plain fin heat exchanger. The one row results are discussed first. The local Sherwood number was reported on the fin surface as a function of the transverse coordinate at 18 different flow depths using 3 different face velocities. The geometry of their heat exchanger appears in Table 1C. Only the lowest face velocity (appearing in Table 1C) was examined in detail because the others are much larger than experienced by typical heat exchangers in HVAC applications. The core depth in Table 1C corresponds to that of an equilateral tube configuration, which is used for all the calculations in this experiment.

No data on the leading edge Sherwood number was collected, probably due to experimental constraints. The closest point reported to the leading edge of the fin was at $x_1 = 1$ mm. The leading edge is the point of highest heat transfer and the data presented by Saboya and Sparrow (1974, 1976) does not include this point. The method used to estimate the average heat transfer coefficient for the first millimeter is to use the average Sherwood number corresponding to the average heat transfer coefficient as the 2D channel flow case. This is most likely a slight overestimate because it neglects the slowing of the airflow along the streamline approaching the centerline of the tube. Since the dependence of h on V is less than linear, this decrease is only partially offset by the higher velocity at the leading edges between the tubes.

Table 1C. Heat exchanger used for local heat transfer measurements (Saboya and Sparrow, 1974, 1976).

N	1
depth [mm]	18.5
S_t [mm]	21.5
F_s [mm]	1.65
D [mm]	8.53
$V_{channel}$ [m/s]	0.94

Figure 3C shows the dimensions of the naphthalene plate used in (Saboya and Sparrow, 1974). Only one half of a tube pitch of naphthalene is need due to symmetry.

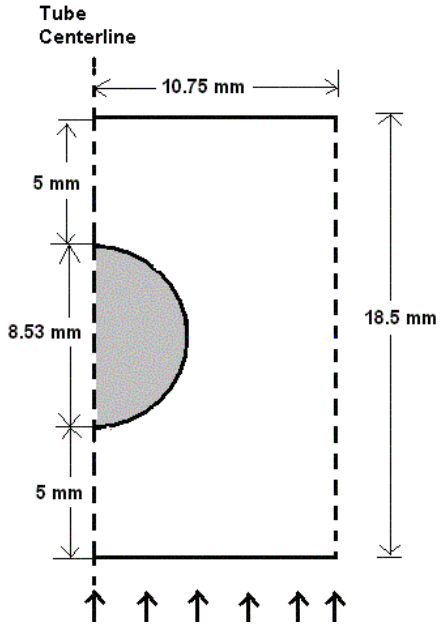

Figure 3C. Experimental schematic of naphthalene experiment used by Saboya and Sparrow (1974).

Figure 4C below shows the longitudinally local transverse average heat transfer coefficient as a function of flow depth, computed from Saboya and Sparrow (1974) data by integrating across the fin surface in the transverse direction at each of the 18 cross sections where measurements were made. Each average is computed at a given longitudinal coordinate. All transverse averages in this report are thus "longitudinally local". Also shown in Figure 4C is the curve for local heat transfer coefficient as calculated by the 2D channel flow correlation.

The 2D channel flow correlation is set with the same configuration used in Table 1C, but without the presence of a tube. The local heat transfer coefficients are uniform in the transverse direction for this pure channel flow situation. Saboya and Sparrow (1974) show that the presence of a tube can produce local heat transfer coefficients as much as a factor of 10 higher near the leading edge of the tube where the root vortex is strongest. When the local heat transfer coefficients are averaged transversely, the maximum enhancement is only 1.3 as shown in Figure 4C. Fin area blocked by the presence of the tube was not included in the averaging. The upstream edge of the tube begins at a flow depth of 5 mm and the downstream edge is at 13.5 mm as shown by the vertical lines in Figure 4C. The naphthalene experiment shows the purely local heat transfer coefficient is lowered by tube-fin interactions in the stagnation region upstream of the tube and is reduced to nearly zero in the wake region behind the tube. These wake regions extend far downstream, unless they are influenced by the presence of another row of tubes.

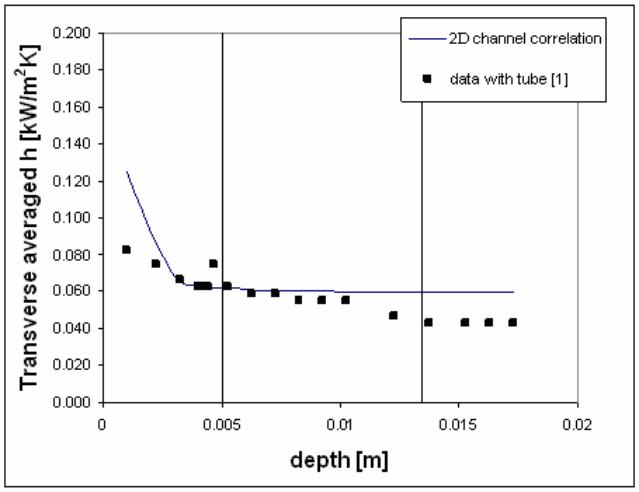

Figure 4C. Transverse averaged local heat transfer coefficient data from Saboya and Sparrow (1974) (with a tube) and predicted by the 3D channel flow correlation (without a tube).

Figure 4C shows that near the leading edge a much lower heat transfer coefficient was measured by Saboya and Sparrow (1974) than predicted by the 2D channel flow correlation. The reason for the dramatic difference for the first data point is not completely clear, but it could simply reflect the inability to measure local mass transfer close to the leading edge. Also it is reasonable to expect a lower heat transfer coefficient with the presence of a tube due to the slowing of the flow in front of the tube. The next two points in the stagnation region nearly match channel flow, indicating that interactions have a small effect on transverse average heat transfer here. The 2D channel flow curve bends sharply at the third data point, indicating the rapid thickening of the boundary layer.

In Figure 4C it can be seen that just upstream of the tube, the data reveals a jump in heat transfer coefficient due to the high mixing from the root vortices. Just upstream of the stagnation region the heat transfer coefficients are roughly equal. The formation of root vortices occurs here (4 mm deep). The increased heat transfer coefficient from the root vortices balances with the decreased coefficient from the tube blockage yielding a transverse average heat transfer coefficient comparable to channel flow without the tube. After the vortices are formed they are swept around the tube. This keeps the heat transfer coefficient near that of channel flow even beyond the midpoint of the tube, where the wake region begins to form. The combined effect of increased velocity and the vortex enhancement generally raise transverse average heat transfer coefficient in the minimum flow area, but at this low face velocity the vortices cause little enhancement. Also there is a dip in fin heat transfer coefficient just outside the vortex region due to the boundary layers growing from the tube. This dip is encountered in a transverse direction just outside of the vortex and exists downstream of the tube centerline. The result is that the transverse average is roughly equal to that of channel flow in between the tubes in the maximum velocity region.

Beyond the mid-point of the tube (9.25 mm), the wake region begins to form behind the tube. This region is characterized by very low flow velocities and heat transfer coefficients. In Figure 4C this region is characterized by the measured heat transfer coefficient (with tubes) drops below the 2D channel flow coefficient (without tubes). At any depth where a wake region exists, the flow is low within the wake but proportionally higher outside the wake due to continuity. The local heat transfer coefficient therefore is higher outside the wake. The transverse average including the wake and region of maximum velocity is lower than it would be with an evenly distributed equal mass flow. This is because the heat transfer coefficient over a plate is roughly proportional to the square root of velocity.

Figure 5C shows the same results as Figure 4C, expressed as a percent difference between the two transverse average heat transfer coefficients as a function of the fraction of channel depth traveled. Plotting results in this form provides a better framework for describing the physics of the flow. Vertical lines show upstream and downstream edges of tube

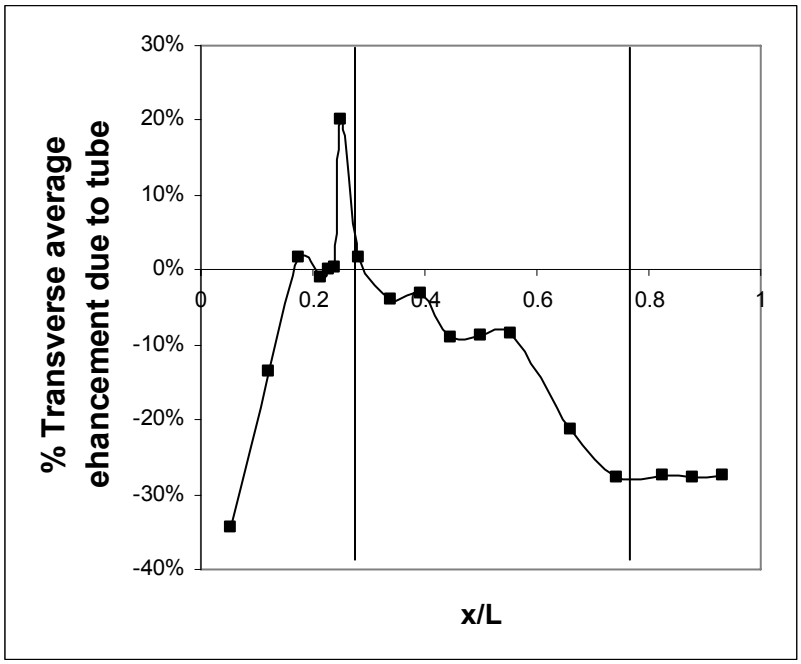

Figure 5C. Percent enhancement in local transverse average fin heat transfer coefficient (for the specified depth) due to the presence of the tube.

The first point in Figure 5C shows that tube-fin interactions lower the transverse average heat transfer coefficient because the oncoming flow is slowed due to the presence of the tube. The spike in enhancement at x/L = 0.25 is due to the impinging flow on the tube creating the root vortex. After the spike (for x/L = 0.25 → 0.6) the degradation caused by the boundary layers from the tube is offset due to the constriction and the sweeping of the vortices around the tube. After x/L = 0.55 the local heat transfer coefficient degrades quickly as the tube cross sectional area is replaced by wake area. After the flow has passed the tube the stagnant wake is just as wide as the tube and the heat transfer coefficient is lowered by 27% compared to channel flow.

Figure 6C shows the result obtained assuming that heat transfer along the leading edge (first 1 mm of flow depth, 5 mm upstream of the tube) is the same as for 2D channel flow. This is most likely an overestimate because it neglects the slowing of the airflow as it approaches the tube (as shown in Figure 4C). The average heat transfer coefficient, integrated from the leading edge to the flow depth shown, is shown in Figure 6C, with and without tubes.

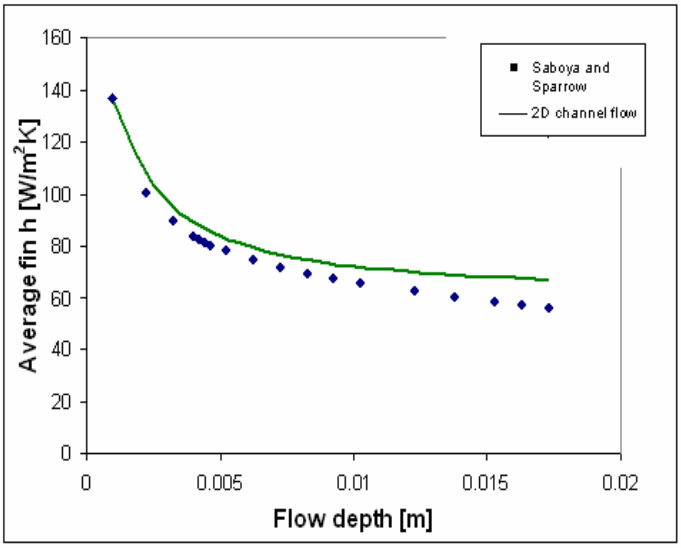

Figure 6C. Cumulative average fin heat transfer coefficient (leading edge to flow depth) for a channel with and without the presence of a tube assuming same leading edge value.

For all depths after the first millimeter the average heat transfer coefficients with tubes is lower than without tubes. In front of the tube the average coefficient is lower because of the slowing of the flow as it approaches the tube. As the flow passes over the tube, the difference between average heat transfer coefficients does not increase because of the vortices and the contraction effect. After flowing past the tube, the average heat transfer coefficient decreases more rapidly due to the wake region. Near the end of the flow depth, the lower heat transfer coefficient in the presence of a tube is to be expected to be lower primarily due to the wake region effect.

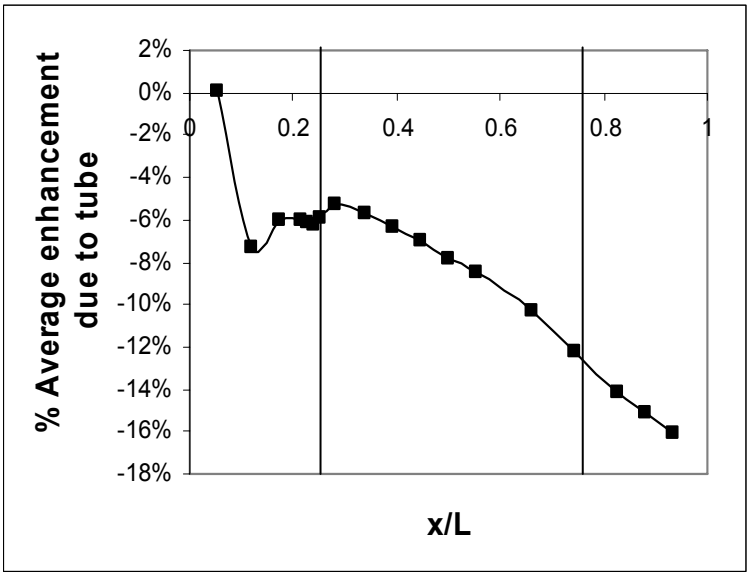

Figure 7C. Same information as Figure 6C, but expressed as a cumulative enhancement of average fin heat transfer coefficient due to the presence of the tube.

Figure 7C shows that average heat transfer coefficient is higher everywhere without the presence of a tube. The first point of average data was not available from the data Saboya and Sparrow (1974) provided, so the

enhancement was assumed to be zero, i.e. the first millimeter of flow was assumed to have the same average fin heat transfer coefficient in both cases. For the rest of the points in front of the tube (x = 0 → 0.27) average heat transfer coefficient has a negative enhancement because of the slowing of the airflow and the large difference between the transverse average first data point taken from (Saboya and Sparrow, 1974) and the 3D channel flow prediction. From x/L = 0.1 → 0.3 the positive slope of the curve can be attributed to the root vortices which form and increase the heat transfer coefficient. Neglecting the leading edge, the average heat transfer coefficient is highest near the point where the stagnation streamline hits the front of the tube. Vertical lines show where the tube begins and ends (x/L = 0.27 → 0.73)

When the flow starts going around the tube (x/L = 0.27 → 0.73), the curve begins decreasing. This is because there is less enhancement here than in front of the tube and the boundary layers forming from the tube affect the fin heat transfer coefficient. This is where the local heat transfer coefficient is highest, but the transverse average coefficient is lower here than in front of the tube. The maximum local coefficient only takes place on a very small strip of area around the tube.

Behind the tube (x/L = 0.73 → 1) the wake region decreases the heat transfer coefficient. As shown in Figure 7C by the last point, the total effect of the tube on average fin heat transfer coefficient is to decrease it by 16%. This net decrease in heat transfer coefficient is to be expected because the presence of the tube increases and decreases flow velocity behind the tube, and heat transfer coefficient is proportional to the square root of velocity, as mentioned earlier. So the net effect of the faster and proportionally slower flow is to decrease average heat transfer coefficient over the surface of the entire fin.

Figure 7C relates to Figure 1C in that: for a one row heat exchanger with a tube pitch of 21.5 mm the heat transfer coefficients with and without the presence of interactions are very similar. As shown in Figure 1C, the Wang et al. (2000) correlation predicts interactions cause a 12% decrease in average heat transfer coefficient compared to the superposition correlation. This is slightly different than that predicted by Saboya and Sparrow (1974) (16%), but the difference is within the accuracy of the correlations and experiments.

As mentioned earlier, Saboya and Sparrow (1974) presented data for 3 air velocities with a one row heat exchanger, with the same configuration of heat exchanger in Table 1C. Figures 8C and 9C show the percent enhancement due to the tube as a function of nondimensional depth for channel velocities of 2.86 and 5.59 m/s (max velocities of 4.72 and 9.25 m/s). Recall that Figure 5C shows the same plot for a channel velocity of 0.9 m/s.

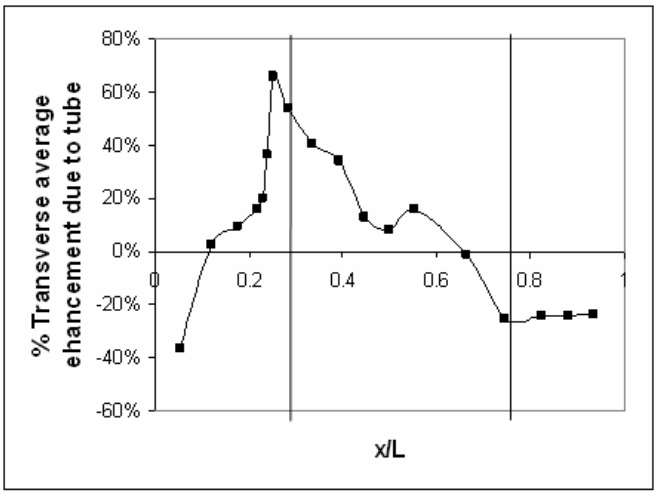

Figure 8C. Percent enhancement in transverse average fin heat transfer coefficient (for the specified depth) due to the presence of the tube. Channel velocity of 2.86 m/s.

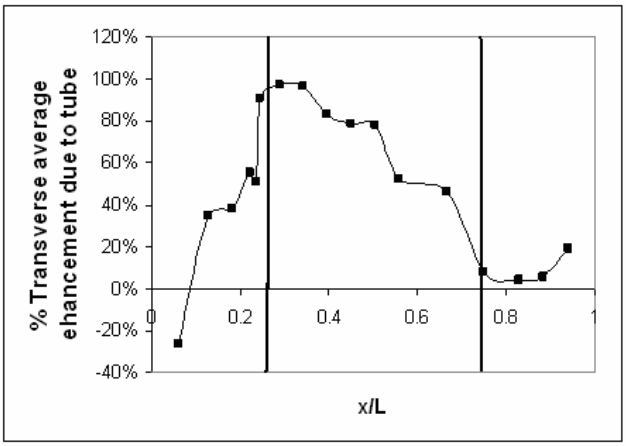

Figure 9C. Percent enhancement in transverse average fin heat transfer coefficient (for the specified depth) due to the presence of the tube. Channel velocity of 5.59 m/s.

Figures 5C, 8C, and 9C show that as air velocity increases, the interactions increase the fin heat transfer coefficient more relative to pure channel flow. Also the peak heat transfer coefficients cover a wider area and extend for a greater depth. This is due to larger and stronger root vortices that do not dissipate as quickly. For the 5.6 m/s channel velocity case, the vortices do not die out after being swept around the tube. They extended through the exit area of the channel.

Table 2C shows two methods of determining the effect of interactions by comparing physical models to an empirical model and experimental data. The table shows percent degradation due to interactions as predicted by superposition compared to the empirical Wang et al. (2000) correlation (fins and tubes), and 2D channel flow compared to Saboya and Sparrow (1974, 1976) (fins only). The same heat exchanger geometry as Table 1C was used. For the one row coil, the 2 lower velocities show good agreement between the interaction degradation of the fin heat transfer coefficient and the fin and tube coefficient. This is reasonable because a one row tube-fin heat exchangers has a fin heat transfer coefficient within 1% of the fin and tube coefficient as previously mentioned. For

the high velocity one row coil, it is not clear why the two methods show different levels of interactions. For two row coils both methods show comparable levels of interactions.

Table 2C. Percent degradation due to interactions for Wang et al. (2000) (fins and tubes) and Saboya and Sparrow (1974, 1976) (fins only).

N	V_{max} [m/s]	% degradation comparing superposition and Wang et al. (2000)	% degradation comparing 2D channel flow and (Saboya and Sparrow, 1974, 1976)
1	1.56	18	16
1	4.72	5.8	7.6
1	9.25	8	-22
2	1.47	20	25
2	7.76	-23	-19

C.3 Multirow Small Fin Pitch

For a heat exchanger with 2 or more staggered rows, the situation changes significantly. The change in flow occurs because the flow is accelerated by the first row of tubes and impinges at high velocity on the second row, causing even higher heat transfer coefficients from a stronger root vortex in front of the second tube row. This results in the second row showing a large spike in heat transfer coefficient as shown in Figure C10 below. In spite of this the degradation of the heat transfer coefficient is substantially more for the second row because the stagnant wakes extend from the first row through the entire heat exchanger. The wakes begin to fill in by the exit plane but there is still a negative effect, which is combined with the negative effect of the wakes behind the second row.

The higher flow velocity impinging on the second row can result in either one or two pairs of root vortices. Just how fast this impinging flow is depends on heat exchanger geometry and the length of the wake region. If longitudinal tube spacing is high and face velocity is low, it is possible that the wakes will fill in before the maximum flow region hits the next tube row. The actual length of the wake region is not known; it extends through the exit of the channel in (Saboya and Sparrow, 1974, 1976), although for the lowest velocity the wake begins to fill in at the exit.

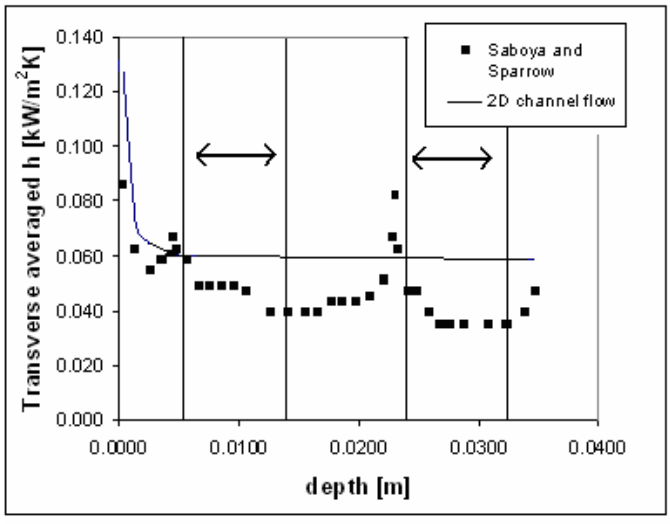

Figure 10C. Transverse average heat transfer coefficients versus longitudinal location for a two row coil.

Figure 10C shows the transverse average heat transfer coefficients as predicted by the 2D channel flow correlation (without tubes) and data collected by Saboya and Sparrow (1976) (with tubes) for a two row deep coil. The geometry is the same as Table 1C. The vertical lines with arrows in between show the locations of the tubes. Root vortices cause the two spikes in front of the tubes which are clearly visible. The low heat transfer regions between tubes of the same row are due to the boundary layer which grows from the tube. Fin areas blocked by the presence of the tube were not included in the averaging. The low heat transfer region behind the tubes is due to the stagnant wake, which only occurs at small fin pitch.

C.4 Large Fin Pitch

Ichimiya et al. (1988) performed an experiment in which a constant heat flux was applied to one side of a flat duct with a cylinder in the duct. The cylinder was placed sufficiently far downstream in the 10 mm high duct to allow the boundary layers to grow together (so that the channel flow was nearly fully developed). The temperature distribution on the plate downstream of the cylinder was measured and recorded. This temperature distribution on the plate was used to obtain local heat transfer coefficients and Nusselt numbers for Reynolds numbers based on a length scale equal to two times the duct height, varying from 1,000 to 10,000. The duct heat transfer enhancement is presented as the ratio of average duct Nusselt numbers with and without the cylinder as a function of Reynolds number and downstream distance. Experiments were repeated for cylinder diameters of 10, 15 and 20 mm.

Only Reynolds numbers of 1000 and 2000 are considered here because the next largest Reynolds number used is 3000, which is entering the transition regime. A linear interpolation on Nusselt number was applied between the two lowest Reynolds numbers to find intermediate heat transfer values. Smaller Reynolds numbers can be accounted for by extrapolating the linear fit to smaller Reynolds number. Reynolds numbers over 2000 are not uncommon in heat exchangers with large fin pitch. This type of flow is not affected by the transition to turbulent flow if the flow is still developing, and therefore can be modeled with laminar correlations if the linear fit on Reynolds number is extrapolated upwards of 2000.

The data on average enhancement is presented in (Ichimiya et al., 1988) in the form of a single plot which shows the enhancement on the y axis and nondimensional downstream distance from the rear of the tube on the x axis for 7 Reynolds numbers, five of them transition or turbulent. This figure appears in Figure 12C below, and shows that enhancement ratio is not a function of cylinder diameter for a Reynolds number of 1000. The variation in enhancement with Reynolds number is due to velocity changes alone. The effect of duct height was not investigated directly; perhaps changing the Reynolds number through duct height will have a different effect than that reported by Ichimiya et al. (1988).

In an attempt to generalize these results to other duct heights, interactions between the cylinder and base plate boundary layers must be considered explicitly. Two types of vortices are created, the root (or horseshoe) vortex is created at the upstream portion of the fin-tube junction, and the vortex street is created by the tube and extends downstream. The root vortex forms in front of the cylinder and enhances heat transfer on a small area roughly equal to the cross sectional area of the tube. This vortex was shown to exist for both small fin pitches (Saboya and Sparrow, 1974, 1976) and large fin pitches (Ichimiya et al., 1988). The heat transfer caused by the root vortex was shown to be a strong function of the velocity which impinges the tube (Saboya and Sparrow, 1974, 1976). Every tube row after the first will see greater enhancement because the free flow area is smaller than that seen by the first tube row. Also, the development of the boundary layer may diminish the strength of the root vortex due to lower velocity gradients at the fin-tube junction.

The second type of vortex is the vortex street, which forms behind the tube and extends downstream. The phenomenon is well understood in the case of tube banks (the limiting case of large fin pitch). However the vortex street has not been observed directly in exchangers with small fin pitch (Saboya and Sparrow, 1974, 1976). To understand how this affects fin heat transfer first consider the case of infinite fin pitch, where the cylinder would see uniform flow. Over the range examined in Ichimya et al.'s (1988) experiments ($350<Re_D<2000$) the cylinder's boundary layer is separated, producing a turbulent and "increasingly three-dimensional" vortex street for Reynolds numbers between 150 and 300,000 (Mills, 1995). Assuming at the lower end of this range that the vortex street is basically two dimensional, the pressure distribution on the base plate would be influenced by the velocity field in the cylinder's wake (neglecting interaction so the pressure gradient through the base plate's boundary layer can still be neglected).

Since Ichimiya et al.'s (1988) experiments were conducted with the cylinder placed at the streamwise location just downstream of the point where the flat plate boundary layers have just touched, the question arises about their applicability to the case of developing flow. The range of heat exchanger geometries and operating conditions of interest (i.e. 7-10 mm tubes; 0.7-2.0 m/s face velocity; 1-15 mm fin pitch) include ducts where the tubes see fully developed flow, and cases where the boundary layers have not yet touched, even at core depths greater than 100 mm. Under conditions of developing flow in a 2-D duct, the tube heat transfer and pressure drop are greater than that seen by a flat plate, because the velocity at the centerline of the duct exceeds the face velocity by an amount related to the thickness of the velocity boundary layer. Figure 11C shows hydrodynamic entry length for a fin array, as a function of fin pitch and Reynolds number based on hydraulic diameter as predicted by Wiginton and Dalton (1970). Figure 11C shows that at larger values of fin spacing and Reynolds numbers, fully developed flow occurs far beyond the depth of conventional heat exchangers.

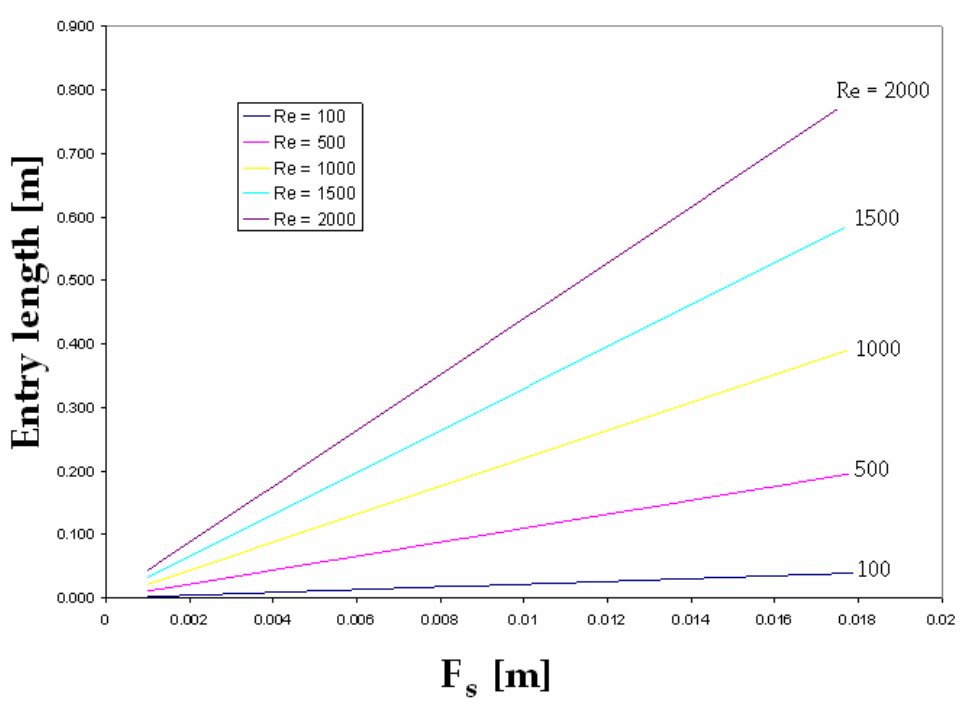

Figure 11C. Hydrodynamic entry length vs. fin spacing for different Reynolds numbers.

Figure 12C shows that higher laminar Reynolds numbers result in a higher percent enhancement of local heat transfer coefficient on the fin at the base of the tube, in part due to the stronger root vortices. In contrast, for the baseline case of fully developed flow in an unobstructed 2D channel, the local Nusselt number is independent of Reynolds number. For the lower laminar Reynolds number of 1000 the data points for the three tube diameters are coincident, indicating that the enhanced area scales with tube diameter. For the larger laminar Reynolds number of 2000 tube diameter has some effect on enhancement. No trend is easily observed from Figure 12C, but at X/D of 1 enhancement is greater for smaller tube diameter. This may be due to larger vortices from larger tubes interacting destructively from opposing fin surfaces as discussed below. This effect is minimal compared to the effect of Reynolds number. The dependence of enhancement factor on Reynolds number reflects the velocity increasing while geometry remains fixed. This results in strengthening of the vortex street shed by the tube and perhaps the effects of the thinner fin boundary layer and the vortices being closer to the fin. Ichimiya et al.'s (1988) surface temperature measurements tend to confirm – qualitatively at least – that the influence of the vortex street extends to the base plate (fin), apparently producing nonzero velocities throughout the wake region, including the region immediately downstream of the tube (see Figure 13C).

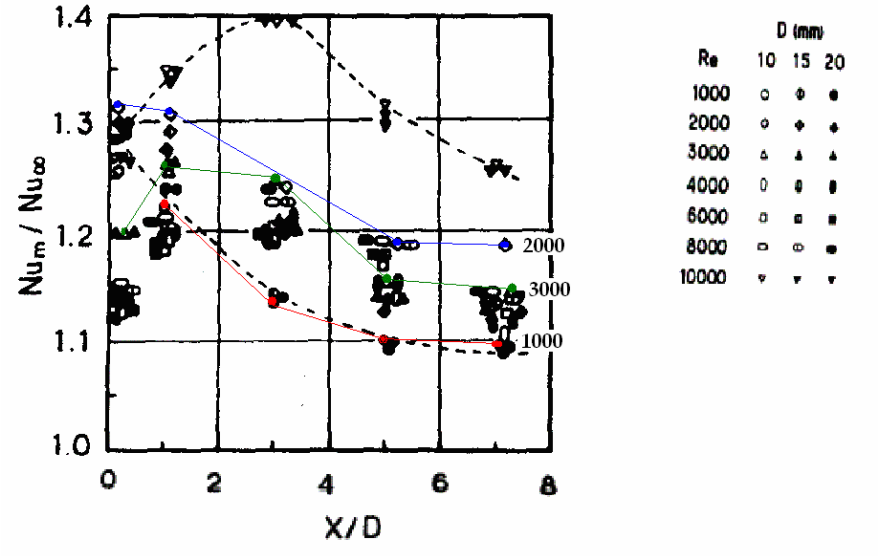

Figure 12C. Data showing heat transfer enhancement versus depth for 7 Reynolds numbers where X/D is the distance downstream of the tube trailing edge (Ichimiya et al., 1988).

Solid lines are drawn on Figure 12C to show the trends for the 3 non-turbulent Reynolds numbers. Only 1000 and 2000 are laminar, 3000 is transition. Not every data point was able to be read but the general trends of the curves were captured. The points corresponding to Reynolds numbers of 3000 and greater were ignored in the enhanced wake correlation development because only laminar flow is under consideration here.

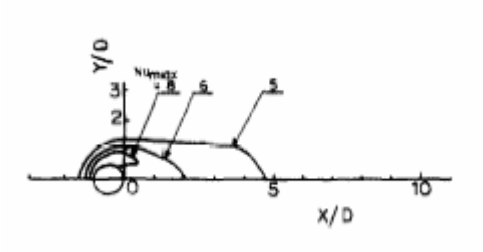

Figure 13C. Iso-Nusslet number lines for Reynolds numbers of 1000 (Ichimiya et al., 1988)

The enhancement behind the tube comes from the interaction of the root vortex and the vortex street. As the root vortex is swept around the sides and behind the tube, it mixes with the vortex street. At large fin pitch the root vortex has room to develop and is swept around the tube. The root vortex contributes its transverse velocity to that of the vortex street, enhancing the fin heat transfer coefficient behind the tube. If the tube is positioned in the presence of a thin developing fin boundary layer this effect is stronger due to the stronger root vortex. For this reason it makes sense to apply Ichimiya et al.'s (1998) enhancement factors as a percent of local channel heat transfer directly in front of the tube, and not only the fully developed portion.

Based on the fact that Ichimiya et al.'s (1998) results showed little dependence on tube diameter for both laminar Reynolds numbers (1000 and 2000), for sufficiently large fin pitch we assume that the structure of the vortex street will scale with tube diameter over the range typically encountered in heat exchangers ($0.007 < D < 0.010$). In Ichimiya et al.'s (1988) experiments the tube diameter was equal to and greater than the duct height. Figure 13C shows iso-Nusselt number contours of experiments with the tube diameter equal to duct height (10 mm). This figure also appears as Figure 3.2, but is shown here again for convenience. The enhanced region behind the tube indicates that no stagnation region forms. For laminar Reynolds numbers, Ichimiya et al. (1988) shows comparable enhancement for tube diameters of 15 and 20 mm, again indicating that the stagnant wake region does not form. Saboya and Sparrow (1974, 1976) show that for a tube diameter equal to 5 times the duct height (1.65 mm) a stagnant wake region forms behind the tube. This suggests that at some critical duct height (or duct height-tube diameter ratio) a fundamental change occurs in the interaction between the vortex street and root vortex. As the fins are brought together the root vortices on opposing fins will touch and prevent the vortex street from forming, with their transverse velocities beginning to cancel one another, while frictional forces on the fin surface play a larger role in dissipating the strength of the horseshoe vortices. Apparently, when the opposing root vortices touch they create a barrier that prevents fluid from entering the region behind the tube. The result is the stagnant wake when fin pitch is small.

For the case of small fin pitch naphthalene sublimation experiments by Saboya and Sparrow (1974, 1976) showed that the wake is characterized by a stagnation region that forms directly behind the tube and extends downstream. Just outside the wake are thin strips of enhanced area, presumably due to the root vortices, which extend downstream with the wake. These strips are prominent only for high velocity and are very thin, providing little overall enhancement. For large fin pitch, Ichimiya et al.'s (1988) results suggest that the root vortices have enough room to form and grow, subject to only minimal frictional dissipation at the fin surfaces. Their transverse velocities near the fin surface, in conjunction with alternating streamwise velocities produced by the vortex street, results in enhancement of fin heat transfer behind the tube. The local heat transfer coefficient one tube diameter behind the tube predicted by Ichimiya et al.'s (1988) is 30% over that of fully developed channel flow for a

Reynolds number of 1000 (Figure 13C). Saboya and Sparrow (1974) predicts a local heat transfer coefficient up to 88% lower than a uniform temperature duct at the same downstream distance.

Figure 13C supports the existence the two types of vortex enhancement: the vortex street which forms downstream of the tube and the root vortex which forms at the upstream tube-plate junction. The root vortex is swept around the sides of the tube; as the root vortex is swept downstream, the fluid structure becomes the vortex street if there is enough room. As discussed above, the vortex street only forms when the duct height is large enough. The root vortex is present regardless of duct height and always causes positive enhancement (Saboya and Sparrow, 1974, 1976), at least locally. The enhancement for large fin pitch (Ichimiya et al., 1988) and laminar flow is nearly independent of tube diameter. This indicates that the sum of enhancement due to the root vortex and vortex street is not affected by tube diameter.

Although only one wall was heated in Ichimiya et al.'s (1988) experiments, the results of Javeri (1975) for fully developed 2-D channel flow indicate that they ought to apply as well to the case where heat transfer occurs at both walls (isothermal or constant heat flux). Ichimiya et al.'s (1988) results, however, were limited to the case of constant wall heat flux. The heat transfer trends for an isothermal wall are similar to those of constant wall heat flux i.e. decreasing Nusselt number with increasing x*, reaching fully developed at a value of around 2. Constant heat flux on one wall does not affect the velocity boundary layer. This means the fluid vortices are mostly unchanged and the enhancement should be nearly the same even though Nusselt numbers are different. The Prandtl number is a fluid property: the ratio of kinematic viscosity to thermal diffusivity. It is the ratio of the velocity to thermal boundary layer thickness and is unaffected by the boundary conditions.

The heat transfer enhancements Ichimiya et al. (1988) reported in Figure 12C were obtained by integrating within the area enclosed by the iso-Nusselt number contour intersecting the x axis for various downstream distances. For example, the enhancement area for a Reynolds number of 1000 and an X/D of 5 is shown in Figure 12C within the Nu=5 contour. The enhancement factor is defined as the area-averaged Nusselt number within the contour divided by the local Nusselt number in a fully developed flat duct (which is 5.4 for one wall with constant heat flux). The contours in Figure 13C confirm the enhancement factors shown in Figure 12C. Figure 12C shows that the local enhancement generally decreases as the downstream depth and enhanced area increase. This shows that local enhancement is greatest near the tube. Figure 13C above shows the iso-Nusselt number lines reported in (Ichimiya et al., 1988).

The average enhancement factor and enhanced fin area per tube were shown to be functions of Reynolds number, tube diameter, and downstream distance. These functions were determined and are shown in Chapter 3 as part of the enhanced wake correlation.